Scanning tunneling microscopy study of strong metal-support interaction in iron oxide based model catalysts

vorgelegt von

Dipl.-Ing.

KE ZHANG

Geboren in ChangZhi, ShanXi, China

Von der Fakultät II - Mathematik und Naturwissenschaften
der Technischen Universität Berlin
zur Erlangung des akademischen Grades
Doktor der Ingenieurwissenschaften
Dr.-Ing

genehmigte Dissertation

Promotionsausschuss:

Vorsitzender: Prof. Dr. rer. nat. Reinhard Schomäcker
Gutachter: Prof. Dr. rer. nat. Hans-Joachim Freund
Gutachter: Prof. Dr. rer. nat. Mario Dähne
Tag der wissenschaftlichen Aussprache: 22.09.2017

Berlin 2018

Diese Arbeit wurde von April 2014 bis Juli 2017 am Fritz-Haber-Institut der Max-Planck-Gesellschaft in der Abteilung Chemische Physik unter Anleitung von Herrn Prof. Dr. H.-J. Freund angefertigt.

Abstract

The *term* "*strong metal-support interaction*" (SMSI) was introduced by S.J. Tauster in late 1970's to describe drastic changes in the chemisorption properties of metal particles supported on reducible oxides. Although there may be different explanations for SMSI effect, in the great majority of cases, it manifests itself via encapsulation of the supported metal particles by a thin oxide layer stemming from the support. To shed more light on the encapsulation mechanism and atomic structure as well as on the role of the encapsulating layer on structure-activity relationships, in this work we made use of planar model systems based on well-ordered iron oxide thin films grown on metal single crystal substrates. The studies were carried out under controlled Ultra-High Vacuum (UHV) and exposure conditions primarily using Scanning Tunneling Microscopy (STM) in combination with other surface science techniques such as LEED, AES and TPD.

In the first system, metal (Pt, Pd) nanoparticles were deposited onto magnetite $Fe_3O_4(001)$ surface. Nucleation, growth and thermal stability in vacuum were studied. The results provided strong evidence that Pt nanoparticles on $Fe_3O_4(001)$ are encapsulated by an FeO(111) layer upon UHV annealing at elevated temperatures, i.e. in the same manner as for the $Pt/Fe_3O_4(111)$ system previously studied in the group. Therefore, the results show that the encapsulation takes place irrespective of the surface structure of the oxide.

Similarly, SMSI driven encapsulation was observed upon vacuum annealing of $Pd/Fe_3O_4(001)$. Although, for both Pt and Pd, the annealed metal particles exhibited a cuboid shape, considerably larger particles are ultimately formed for Pd than for Pt (~ 20 *vs* ~ 5 nm). This finding is rationalized in terms of the encapsulation blocking metal sintering (presumably via Ostwald ripening), both processes occurring simultaneously at elevated temperatures. Since Pt shows (on the basis of theoretical calculations) a considerably higher adsorption energy as compared to Pd, much smaller Pt particles are forming before the encapsulation sets in and hence blocks sintering.

As the second model system, we addressed ultrathin FeO(111) films grown on Pt(111), which, to some extent, mimic the surface of encapsulated Pt particles. In an attempt to elucidate the reaction mechanism and the role of the metal support in this reaction, we also studied FeO(111) films grown on Au(111), for comparison. Both Au and Pt supported films show promotional effect in the CO oxidation reaction. Structural transformations were monitored by STM in vacuum, in oxygen and CO ambient on the films as a function of oxide coverage and exposure conditions. The results show that oxygen desorption on O-riched FeO_{2-x} islands starts at the edges and propagates towards interior parts. Also reaction with CO, that reduces FeO_2 to FeO, first occurs at the FeO_2/Pt interface and then propagates inside the island. Based on these findings reaction mechanisms were proposed.

In general, the results show that reactivity of encapsulated metal particles is intimately linked to the structure and reactivity of ultrathin films and their interfaces, and thus provide further useful information towards rational design of metal catalysts based on ultrathin oxide films.

Zusammenfassung

Der Begriff “Starke Metall-Substrat-Wechselwirkung” (engl.: strong metal-support interaction, SMSI) wurde von S. J. Tauster in den späten 1970er Jahren eingeführt, um die drastischen Änderungen in den Chemisorptionseigenschaften von Metalpartikeln, geträgert auf reduzierbaren Oxiden, zu beschreiben.. Obwohl es viele Erklärungen für SMSI Effekte geben mag, manifestieren sie sich, in der großen Mehrzahl der Fälle, über Einkapselung der geträgerten Metallpartikel durch eine dünne Oxidschicht, die von der Unterlage stammt. Um mehr Licht auf den Einkapselungsmechanismus und atomare Struktur, sowie auf die Rolle der Einkapselungsschicht auf Struktur-Reaktivitäts-Beziehungen zu werfen, machen wir in dieser Arbeit Gebrauch von ebenen Modellsystemen basierend auf wohlgeordneten Eisenoxid Dünnfilmen, die auf Metall Einkristallen gewachsen sind. Die Untersuchungen wurden unter kontrollierten Ultrahochvakuum-(UHV) und Expositionsbedingungen primär mittels Rastertunnelmikroskopie (Engl.: scanning tunneling microscopy, STM) in Kombination mit anderen Techniken der Oberflächenforschung wie LEED, AES und TPD durchgeführt.

Im ersten System, wurden Metallnanopartikel (Pt, Pd) auf Magnetit Fe_3O_4(001) Oberflächen deponiert. Keimbildung, Wachstum und thermische Stabilität im Vakuum wurden untersucht. Die Ergebnisse zeigen starke Belege für eine Einkapselung von Pt Nanopartikeln auf Fe_3O_4(001) durch eine FeO(111) Schicht nach tempern im UHV bei erhöhten Temperaturen, d.h. in der gleichen Weise wie für das Pt/ Fe_3O_4(111) System, welches zuvor in dieser Gruppe untersucht wurde. Daher zeigen die Ergebnisse, dass die Einkapselung unabhängig von der Oberflächenstruktur des Oxids stattfindet.

In ähnlicher Weise wurde SMSI getriebene Einkapselung beobachtet nach Vakuumtempern von Pd/Fe_3O_4(001). Obwohl sowohl für Pt als auch für Pd die getemperten Metallpartikel eine Quaderform aufwiesen, wurden bei Pd im Endeffekt deutlich größere Partikel gebildet, als für Pt (~ 20 versus ~ 5 nm). Dieser Befund wird erklärt durch ein Blockieren des Sinterprozesses (vermutlich via Ostwald Reifung) durch die Einkapselung, da beide Prozesse bei erhöhten Temperaturen gleichzeitig ablaufen. Da Pt im Vergleich zu Pd (auf der Basis theoretischer Berechnungen) eine deutlich größere Adsorptionsenergie aufweist, bilden sich viel kleinere Partikel bevor die Einkapselung einsetzt und daher das Sintern blockiert.

Als zweites Modellsystem behandeln wir ultradünne FeO(111) Filme gewachsen auf Pt(111), die, in gewissem Umfang, die Oberfläche eingekapselter Pt Partikel imitieren. In einem Versuch den Reaktionsmechanismus und die Rolle der Metallunterlage in dieser Reaktion zu erhellen, haben wir zum Vergleich auch FeO(111) Filme gewachsen auf Au(111) untersucht. Sowohl Au, als auch Pt geträgerte Filme zeigten Verbesserungseffekte in der CO Oxidationsreaktion. Strukturelle Transformationen an den Filmen wurden mittels STM im Vakuum, in Sauerstoff und

CO Umgebung verfolgt in Abhängigkeit von Oxidbedeckung und Expositionsbedingungen. Die Ergebnisse zeigten, dass Sauerstoffdesorption auf O-reichen FeO_{2-x} Inseln an deren Kanten beginnt und sich zum inneren Teil fortsetzt. Auch die Reaktion mit CO, das FeO_2 zu FeO reduziert, tritt zuerst an der FeO_2/Pt Grenzfläche auf und wandert dann ins Innere der Insel. Basierend auf diesen Befunden wurden Reaktionsmechanismen vorgeschlagen.

Im Allgemeinen zeigen die Resultate, dass die Reaktivität von eingekapselten Metallpartikeln eng mit der Struktur und Reaktivität ultradünner Filme und deren Grenzfläche verknüpft ist und bieten deshalb weitere nützliche Informationen in Richtung rationaler Gestaltung von Metallkatalysatoren basierend auf ultradünnen Oxidfilmen.

Contents

Introduction

The definition of catalyst in my middle school chemistry textbook is "A substance able to increase the rate of a chemical reaction without itself being consumed or changed by the reacting chemicals is called a catalyst." In the corresponding demonstration experiment of hydrogen peroxide (H_2O_2) decomposition catalyzed by manganese dioxide (MnO_2), a powerful reaction of strong effervescence combined with the formation of fog even though just a tiny amount of MnO_2 was added to a H_2O_2 solution deeply impressed me. In modern chemical industry, catalysts are the workhorses of chemical transformations and approximately 85 – 90 % of the products of chemical industry are made in catalytic processes[1]. Many commonly concerned issues in modern society such as sustainable energy, pharmaceuticals and environment protection rely on the development of catalysts.

If the reactant and catalyst interact in different phases, i.e. the above mentioned MnO_2 as solid powder and H_2O_2 as liquid, the catalyst is called heterogeneous catalyst. About 85% of all catalytic processes are heterogeneously catalyzed with the major advantage of easy separation of reactants, products and catalysts[1]. The heterogeneous catalyst is usually deposited on a support material, in most of the cases a metal particle on an oxide support. The support itself and the interaction with the catalyst may affect the catalyst's performance.

For the case of a metal supported on a reducible oxide, i.e. titania, ceria, etc., strong metal-support interaction (SMSI) greatly alters the microstructure and catalytic properties of the system, hence is of great importance in heterogeneous catalysis since this term was introduced in 1978[2]. Besides the typical support effect like charge transferring and affecting metal particle size and shape, one of the mostly discussed SMSI characteristics is the occurrence of the encapsulation of the metal particles by the oxide thin layers. To some extent, the encapsulation can be rationalized on thermodynamic grounds using surface energy considerations. Generally speaking, surface energy of metal is comparatively higher than corresponding metal oxide [3-4], thus the oxide layer encapsulation would decrease the surface energy of the whole system. However, atomic details of how a metal particle undergoes this encapsulation by an oxide has not been fully understood, which is very important not just scientifically, but also for industrial application of this kind of catalysts.

Over the past several decades, an atomic-level understanding of catalysis has greatly advanced through the combination of ultra-high-vacuum (UHV) techniques and model catalyst research on well-defined samples. The subject of my doctoral work is the study of strong metal support interaction on iron oxide based model catalysts by means of scanning tunneling microscopy and other surface science

techniques in UHV system.

The Thesis is organized as follows:

1) Chapter 1 provides a short overview of research progress of SMSI in past 5 years as well as an introduction to the concept of planar model catalysts, in particular of iron oxides.

2) In Chapter 2, the basics of UHV system, experimental setup, characterization techniques and their theoretical backgrounds are described.

3) Chapter 3 presents results of Fe_3O_4(001) film preparation, thermal stability of Pt and Pd, related to the strong metal support interaction effects of Pt and Pd supported on Fe_3O_4(001).

4) Chapter 4 addresses the preparation, oxidation and reduction of ultra-thin FeO supported on Pt(111) and Au(111). The support effect on the structure and reactivity of FeO (111) thin films is highlighted.

5) The Thesis ends with Summary.

Chapter 1.
Literature survey and background knowledge

1.1. Strong Metal Support Interaction (SMSI)

As a ubiquitous phenomenon in heterogeneous catalysis, the interaction between metal particles and support has been noticed and discussed as early as 1930s by G. M. Schwab[5]. But until 1978[2], the term "strong metal support interaction" (SMSI) was firstly introduced by Tauster to describe the passivation of group VIII metals supported on TiO_2 via drastic chemisorption decrease (almost to zero) of hydrogen and carbon monoxide uptake after high temperature reductive treatment. Since then a similar phenomenon was observed on noble metals supported on reducible oxides like CeO_2 [6-19], Fe_3O_4 [20-25], TiO_2 [2, 26-58], V_2O_3 [59-60] and Nb_2O_5 [26, 61-69]. Non-reducible oxides like Al_2O_3 and SiO_2 show no SMSI effect after similar treatment [55, 66, 70].

More and more evidences indicate that most cases of SMSI effect present as the partially reduced oxide patch decoration or thin layer encapsulation to the supported metal particles. These oxide species migrate from the support and block or partially block the chemisorption active sites on metal particles. Early explanation to SMSI includes Tauster's explanation as formation of intermetallic compounds[2, 71-74] and the latter electronic transferring effects, namely the electron transfer from metal oxide support to the metallic component, thus resulting in significant change in chemisorption behavior of the active metals[5, 46, 75-77]. Although these explanations to the *term* of SMSI may not be suitable, with the broader concept that the words "strong metal support interactions" themselves implying, these processes as mentioned above should be included.

Generally, SMSI effects are thought to suppress catalytic activity and be more detrimental for the surface structure sensitive reactions as compared to the structure insensitive ones [21, 37, 66, 78] when the encapsulating layer is inert in the reaction and remains unchanged. This structure-reactivity relationship was directly demonstrated by STM imaging and the CO oxidation catalytic activity measurements on Pt/ TiO_2(110) system[37]. Sample annealing at 1100 K results in encapsulation of Pt particles by reduced titania suboxide thin layer and suppresses the activity for CO oxidation, in contrast, subsequent removing of the encapsulating layer by mild sputtering recovers the activity.

In the view of the significant influence to catalyst activity and common existence in heterogeneous oxide supported metal catalysts, SMSI effects have been subject of numerous studies for the last 30 years. Thanks to the development in real-spaces imaging microscopy techniques [53, 79-80], certain progress has been made concerning

the formation and the structure of encapsulation layers[24, 41, 49, 52, 54, 81-83], non-classical SMSI systems[50, 84-92], tuning of SMSI[15, 19, 35, 37, 39, 46, 56-58, 93-96]. Next, I simply summarize the research progresses of SMSI in the past 5 years.

1.1.1. Details of encapsulating process and the atomic structure of encapsulating layer

The oxide layer encapsulation on metal particle can be rationalized on thermodynamic grounds using surface energy considerations, namely that the surface energy of metal oxide is lower than the corresponding metal[3-4], thus the oxide layer encapsulation would decrease the surface energy of the whole system. However, the detailed mechanism of the encapsulating process is still unclear.

Previous studies on Pd/TiO_2[97] indicated that the encapsulation proceeds through mass transport along the surface rather than through the bulk diffusion Recently, Zhang and coworkers[52] presented the dynamic process of the encapsulating overlayers' formation in this system by using TEM. They found that at low temperatures, an amorphous reduced titania layer was formed, which then crystallizes into either mono- or bilayer structures in reaction environment, together with dramatic reshaping of the metallic surface facets. Jang et al. [54]observed the oxygen vacancy formation, migration and agglomeration in $Pt/TiO_2/Pt$ junction by TEM during reductive treatment, which results in conduction of the junction. The O vacancy behavior can be an important observation point for the SMSI process. Similarly, $Pt\text{-}CeO_2/C$ system was examined by Ou et al.[14] by STM and EELS. They found that after reductive treatment the Pt nanoparticles embeded in the ceria support and ceria patches decorate the Pt surface at low Pt loading. Increasing the Pt loading, the formation of a thin layer decoration with lattice imaging was observed and the ceria thin layer was partly reduced. The EELS (Electron energy loss spectroscopy) study demonstrated that SMSI is strongly related to the redox reaction between Pt and ceria, and closely correlated with the formation of O vacancy on the support surface.

Kovtunov and coworkers monitored the SMSI process by parahydrogen-induced polarization (PHIP) technique[49]. High-temperature annealing dramatically decreases the activity of the Pd/TiO_2 catalyst in terms of the pairwise addition of hydrogen. This process is accompanied with the formation of TiO_2 sub-oxide on Pd as the indicator of SMSI, which is closely associated with the formation of the $Pd^{\delta+}$ state as a result of charge transfer between Pd particles and TiO_2 support.

Based on current literature known, we suggest that there are some common "clues" for the encapsulating process to consider:

1) Reductive treatment at elevated temperatures creates O vacancies and reduced cation on the surface of the support[14, 54 57];

2) Electron transfer between support and metal[49] ;

3) Charged metal and support may facilitate the formation of sub-oxide layer[49];

4) Elevated temperature activates the migration of an oxide layer to the metal surface, this is also energetically favorable and causes the geometrical blocking effect for adsorbates;

5) Higher temperature's treatment would activate the crystallization of the encapsulation layer[52];

6) Negative charged metal particles would affect the adsorption and the subsequent reaction process[46, 98 99];

The atomic structure and composition of the encapsulating layer vary in different systems and affect the activity of the system in different manners. Below are two examples to illustrate. The first one is Cu/ZnO, which is an industrial catalyst for methanol synthesis [83, 100]. It was shown that the ZnO support stabilizes the Cu nanoparticle due to SMSI and the synergistic effect between ZnO_x overlayer and Cu enhanced activity of the catalyst. Schott et al.[83] identified metastable graphitic-like ZnO_x overlayers on the surface of oxidized CuZn alloy by using a series of surface science methods. Partially reduced ZnO patches decorate on top of the metal particles under a strongly reducing condition, which is a typical manifestation of SMSI. Lunkenbein and coworkers[82] confirmed the formation of the encapsulating graphite-like ZnO_x layers in Cu/ZnO catalyst after being reduced in H_2 atmosphere through AC-HRTEM (aberration-corrected high-resolution TEM). They found that the graphitic-like ZnO_x encapsulation layer transforms from rocksalt to a wurtzite structure under continuous electron beam irradiation. This SMSI-induced graphitic ZnO overlayer has paved ways for revealing its rich surface concerns as a virtual playground from the essential surface features to the dynamic behaviours as well as possible interactions between surfaces and gases. This study facilitates elucidating the details of synergy effects between Cu and the ZnO_x encapsulation layer on the catalyst employed in industry.

Another example is the $Pt/Fe_3O_4(111)$ system. Pt nanoparticles were found to be encapsulated by a thin FeO(111) layer film after UHV annealing up to 850K by [20, 25]. Atomic resolution STM images showed that the top facets of Pt particles exhibit the same structure as a FeO(111) monolayer film on Pt(111) [101-102]. Single layer FeO(111) encapsulation on Pt particles in the $Pt/Fe_3O_4(111)$ system was further confirmed by Willinger et al.[24] by using AC-HRTEM and EELS. It was thought that the SMSI effect in this system renders it practically inactive in vacuum because the oxide thin layer suppresses adsorption of molecules otherwise readily adsorbing on the metal surface. However, $Pt/Fe_3O_4(111)$ shows high CO oxidation activity in mbar range due to the transformation of the bilayer Fe-O encapsulating film into a trilayer O-Fe-O film that catalyzes CO oxidation[22]. Revealing of the thin FeO(111) encapsulating layer on Pt

particles opens up a new perspective to study the structure and reactivity of ultra-thin FeO(111) film on Pt(111) surface.

1.1.2. "*Non-classical*" SMSI systems

Zhang's group[88] reported the SMSI effect between metal and nonoxide supports, that is, Au supported on hydroxyapatite(HAP). TEM and in-situ DRIFT (Diffuse reflectance infrared Fourier transform) spectra clearly indicate that this system involves two reversible processes under gas treatments: The encapsulation of Au by HAP-like species layer after oxidative treatment and the following retreat from Au surface after reductive treatment. This is very different to "*classical*" SMSI in metal/reducible oxide systems in which encapsulation usually occurs after reductive treatment and layer retreat in oxidative treatment. The encapsulation of Au enhanced its sintering resistance during high temperature calcination and reusability in liquid-phase catalysis. However, the full encapsulation of the Au particles reduces activity because of the blocking to active sites. Based on this result, the same group tried to control the encapsulation degree between Au and HAP by localizing the Au nanoparticles at the interfacial regions between the TiO_2 and HAP[50]. After oxidative treatment, HAP-like species partially covers the Au particles directly contacting with TiO_2 and provides enhanced activity as in Au/TiO_2 system. In this configuration, the catalyst possesses both high catalytic activity and good sintering-resistance. In principle, this rational design could also be applied to other metal/oxide systems to some extent.

Also, Liu et al.[85] reported Au particles encapsulated by ZnO overlayers after O_2 treatment in Au/ ZnO nano-rod systems. Subsequent hydrogen treatment resulted in encapsulation layer retreat and AuZn alloy formation as well as embedding of gold into the support to some extent. This finding is even more interesting compared to Au/TiO_2 and Cu/ZnO system, in which the encapsulation occurs only after reductive treatment, as in"*classical*"SMSI systems. Further comparative research on these three systems would be helpful to reveal the driving force for encapsulation under different (reducing/oxidizing) atmosphere.

In turn, the "classical" reductive SMSI also depends on the details of reductive treatment. Rui et al.[46] demonstrated the SMSI process of Pt/TiO_2 induced by mild HCHO and $NaBH_4$ solution reduction. Compared to traditional treatment in H_2, the SMSI degree was higher as indicated by CO chemisorption. As a result, a better toluene oxidation activity was achieved. Although they explained this process by a charge transfer process, this unusual treatment confirmed the SMSI after reductive treatment, which is worth applying to other systems. A similar idea was realized by reductive molecule adsorption. Matsubu and coworkers[57] found that high coverage of adsorbates (HCO_x) on the TiO_2 and Nb_2O_5 support induces the formation of oxygen-vacancies, which further drives the migration of HCOx-functionalized oxide

form the support to Rh. The overlayer is amorphous and permeable for reactants. This adsorbate-mediated encapsulating layer is stable under re-oxidation by H_2O and modifies the reactivity of all the remaining exposed Rh sites.

1.1.3. Tuning the SMSI effects

After the introduction of SMSI effects, Tauster suggested to use the SMSI state to tune catalyst performance via controlling the degree of encapsulation[103]. As known, in most cases of SMSI, the oxide overlayer blocks at least partially the metal surface active sites, and passivates the metal surface. Therefore SMSI tuning via support doping and promoter addition, support phase selection as well as encapsulation layer post-processing etc. is employed to adjust the composition of the overlayer and the degree of SMSI to improve the reactivity and selectivity of the supported metal catalysts.

For example, Chen et al. [58] obtained high-performance supported Pd nanoparticles for nitrobenzene hydrogenation catalysis by doping the TiO_2 support with nitrogen. They found N-doping strengthens the binding between the N-TiO_2 support and Pd particles with predominant presence of sub-2 nm in size which is stable under the applied hydrogenation conditions. Additionally, XPS and CO DRIFTS revealed the formation of strongly coupled Pd-N pecies, which restricted the TiO_x overlayer's migration. These high-dispersed Pd-N particles supply more active sites and favor the dissociative adsorption of the test reactant NB as well as they facilitate the desorption of the product aniline. Naldoni and coworkers[56] tested the formic acid plasmonic photo-degradation on Au supported on stoichiometric TiO_2, N-doped TiO_2 and black TiO_2. They found that N doping enhances the SMSI between Au and N-TiO_2 and increases the plasmon enhancement.

Schumann et al.[95] examined the promoting effect of Al, Ga and Mg doping in Cu/ZnO system as methanol synthesis catalyst. They found trivalent promoters Al^{3+} and Ga^{3+} improve conductivity and increase the defect level of the ZnO support, while the Mg^{2+} performs inversely. For activity, Al^{3+} and Ga^{3+} doping lowers the activation energy and facilitates the H_2 activation but Mg^{2+} has no beneficial influence. Al^{3+} and Ga^{3+} promotion was explained by their enhancement to the SMSI, i.e. the formation of a more extended ZnO overlayer, which has a synergy effect with Cu as mention above.

Alkali metals are widely used as promoters of catalysts for many reactions[104-110]. Zhu et al. linked the Na promotion effect with SMSI on Pt-Na/TiO_2 for high water-gas shift activity.[35] Deposition of 2-4 layers of NaO_x resulted in partial covering of the Pt surface, and the strong binding between Pt and NaO_x through Pt-O-Na is induced by Pt electron donation to O in NaO_x. NaO_x covering and strong binding with Pt hinder the migration of TiO_x from the support to the Pt surface and prevent

the Pt particles from sintering. In addition, periphery of the Pt-NaO_x interface provides highly active sites for the reaction. This configuration of alkali metals-O binding could be utilized in other metal/oxide systems.

Li et al.[98, 111] made a comparative investigation on SMSI for anatase and rutile titania supported Pt catalyst by EPR using CO as probe molecules. They discovered that H_2 reduction at low temperature resulted in SMSI on anatase titania support but not on rutile titania support. A similar trend was found for the high temperature H_2 reduced Pt/TiO_2 catalysts.

Bonanni et al.[39] found that slightly reductive treatment enhances catalytic activity of the Pt/TiO_2(110) system for CO oxidation reaction but strongly reductive treatment quenches the reaction. In following work[37] they ascribed the catalytic passivity to SMSI: the encapsulation of the Pt clusters by a thin, reduced titania layer. Subsequent mild sputtering and high temperature UHV annealing removes the encapsulation layer and renders system active and thermally stable.

Our group examined the SMSI in Pt/Fe_3O_4(111) system and found that the hemispherical Pt island was encapsulated by FeO(111) thin layer after 850K UHV annealing and the CO uptake is suppressed[20, 25]. After oxidizing the sample in mbar range O_2 at 450K, the inert FeO(111) layer oxidized to a FeO_2 layer which renders the system highly active for low temperature CO oxidation reaction[21-22]. This method may be valid in all systems with metal encapsulated by a FeO layer which exerts activity after mbar oxidation in the corresponding FeO/metal invers model catalyst [112-115].

1.1.4. Other SMSI effects

In addition to metal surface encapsulation there are other effects caused by interaction of metal and support. The strong bonding between support surface and metal defiantly affects the particle's final shape and size by hindering metal migration and growth through Ostwald ripening. This beneficial effect has been evoked deliberately in the so-called "electrical" catalyst [14, 33, 43, 93, 116] and single atom catalyst [117-118]. Pedenand colleages[84 119] demonstrated strong interaction between ternary oxide spinel $MgAl_2O_4$ and noble metals including Pt, Rh and Ir. They found that well-defined (111) facets of cuboctahedral $MgAl_2O_4$ support is capable of stabilizing Pt particles of 1-3 nm in size during extremely severe aging at 800 ^oC for 1 week. The deactivation is quite slower than the one of a conventional Pt/γ-Al_2O_3 catalyst under methanol steam reforming condition. Similar examination applied to Rh and Ir on $MgAl_2O_4$ shows the stable dispersion of 2 nm for Rh and 1 nm for Ir even at 1123 K in the presence of methane steam. Density functional theory (DFT) calculations suggest that these supported small metal particles have a lower work function than larger ones, which enables a small particle to activate both water and

methane more effectively than a larger one, and have a minimal influence on the relative stability of coke precursors.

Electron transfer between the metal and oxide occurs at the interface as the result of different work functions and electron affinity. The resulted charge states of metal and support are key factors for some catalytic reactions. Rodriguez and colleagues[15] showed that small Pt clusters are subjected to a large electronic perturbation when in contact with ceria, which strongly enhances their ability to dissociate water. For Ni/CeO_2 system[18], they attributed the high O-H bond cleavage activity to the stabilization of Ni ad-atoms on $CeO_2(111)$ and found that the origin of this support effect is the ability of ceria to stabilize oxidized Ni^{2+} species by accommodating electrons in localized f-states of ceria.

Apart from the intrinsic factor, charge transfer between the metal and oxide can be also affected by ambient atmosphere. McEntee and coworkers[99] found that the charge transfer direction (to or from Au) in the Au nanoparticle/TiO_2 system is determined by the nature of applied molecules. Adsorbed donor (reductive) molecules contribute electrons to TiO_2 and cause further electron transfer to Au particles. In contrast, adsorbed acceptor (oxidative) molecule withdraws electrons from TiO_2 thus resulting in electron transfer from Au to TiO_2. The resulted charge state of Au nanoparticles on TiO_2 can be measured by the shift of vibrational spectrum of the chemisorbed CO on Au particles and TiO_2 support in accordance with the well-known Stark effect.

As the result of charge transfer, the charge state of the metal is closely related to the catalytic activity of the system. For O_2 dissociation on the Pt/TiO_2 system for example [46, 98], electron transfer from TiO_2 support to the Pt particles, and the negatively charged Pt further transfers the electrons to the chemisorbed oxygen. Meanwhile, the chemisorbed oxygen is activated during charge transfer. Reductive treatment can enhance this process, which accounts for the high activity for catalytic oxidation of toluene over the reduced samples with SMSI in comparison with the unreduced sample.

1.2. Model catalysts: A “surface-science” approach

1.2.1. Model catalysts

Modern heterogeneous catalysts are complex and their composition and microstructure are precisely controlled to optimize the reaction rate and selectivity. This optimization and new catalyst development are based on the understanding of the reaction mechanisms. On one hand, the complexity of the catalysts must be simplified to facilitate the research for catalysis mechanism, on the other hand, it’s rather clear that the catalytic reactions take place on the surface of a catalytic

material and are not much influenced by the bulk. With the development of ultra-high vacuum (UHV) and surface analytical techniques, the concept of model catalysts was introduced in the late 1960s[120-121].

The model catalyst is a well-defined system and typically employs metal single crystal, metallic thin film, thin oxide film and supported metal particles prepared in UHV system to mimic the reaction proceeding on active site/surface in industrial catalysts. Good correlation between the catalytic behavior of model and industrial catalysts in a number of reaction systems has been demonstrated [121-122]. This well-defined material and an UHV system facilitate the utilization of surface analytical techniques to understand the structure-reactivity relationship. Especially scanning tunneling microscopy (STM) and related techniques are well suited for these model systems and, in principle, allow in-situ observations of catalytic reactions on the atomic scale[123-124]. Reduced complexity and surface analytical techniques' compatibility render the model catalyst a nice methodology for catalysis research.

Metal single crystals

In the early days of the surface-science approach, model catalysts were almost exclusively metallic single crystals. The kinetics and surface chemistry of several catalytic reactions have demonstrated the direct relevance of single-crystal studies for modeling the behavior of high-surface-area supported catalysts. Typical examples include the Ammonia synthesis on Fe[120-121, 125], CO oxidation ($CO + O_2 \rightarrow CO_2$) on Rh, Pd, and Pt[120, 125-127], CO methanation ($CO + H_2 \rightarrow CH_4$) on Ni and Ru[128-130], alkane hydrogenolysis on Ni and Rh[131-132], and ethylene hydrogenation on Pt[121, 133-134]. These works demonstrated that the activity of a particular site can be examined and the effects of surface structure can be explored in atomic detail.

Oxide thin films on metal single crystal substrates

Oxide is the most commonly used support in modern heterogeneous catalysts. However, in most cases, oxide single crystals are insulators, thus the possibility of sample charging puts serious constraints on the application of electron- and ion-based characterization techniques. This problem becomes less critical when corresponding oxide thin films grow on conductive single crystal substrates. The specific surface exposed and morphology features like defects, low-coordination surface sites can be controlled during epitaxial growth of such films. Thus, the growth of Al_2O_3, SiO_2, MgO, CaO, TiO_2, V_2O_3, Cr_2O_3, Fe_2O_3, Fe_3O_4, FeO, CO, NiO, MO_3 and CeO_2 on metal substrates has been extensively studied[135]. In these systems, the oxide film behaves either like a planar support for the dispersion of the metal or it is used to study surface chemistry and the catalytic processes over oxides. It has turned out that supported oxide thin films exhibit unique physical and chemical properties. Their surface structure[135] and charge state are affected by metal support underneath [31, 136]. For example, CeO_x ultrathin film supported on single metal surface shows high

catalytic performance in the water-gas shift, CO_2 hydrogenation, and methane and alcohol reforming[137]. MgO and doped CaO show activity in CO_2 or O_2 reduction due to the electron transfer effect [136, 138-141]. It was again our group which found the high CO oxidation activity on ultra-thin FeO supported on Pt(111)[21], series studies on ultra-thin films include ZnO, MnO, RuO_2 reveal an inverse relationship between bonding energy of enriched O and CO oxidation catalytic activity[142].

Metal particles supported on oxide thin films

This is the most commonly used model system. Single metal crystal surfaces cannot fully represent the complexity of highly dispersed metal catalysts; especially the particle size and interaction with support cannot be ignored. Therefore, metal particles supported on planar oxide surfaces performs better as model system to mimic the real metal-oxide catalyst. Main method to prepare planar oxide supports is the growth of oxide thin films on single metal crystal substrates as mentioned before. Another way is to cleave the bulk oxide single crystals, especially the ones that can be made sufficiently conductive after vacuum treatment, like Fe_3O_4[143] and TiO_2[144]. The metal particles can be deposited by physical evaporation, or chemical vapor deposition, which resembles more closely the preparation in industrial catalysts, as in the case of decomposition of metal-organic precursors or wet chemistry impregnation. In such model systems, the particles' size and density, and hence surface area can be tuned in a well controllable way. The metal-support interaction certainly affects the properties like morphology, charge state and surface coverage.

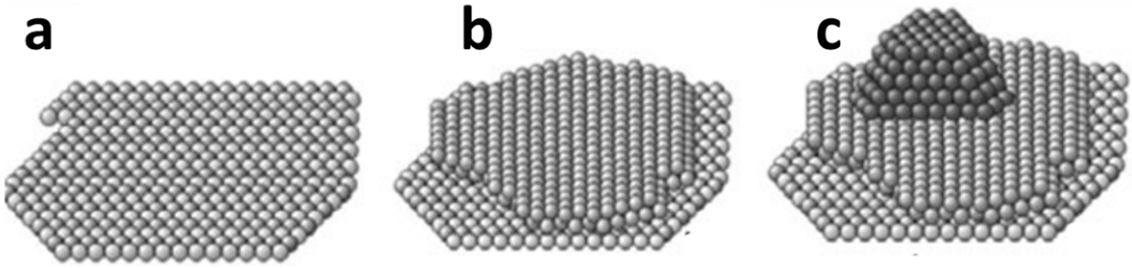

Figure 1-1. Model systems with increasing level of complexity: (a) single metal crystal, (b) oxide film on metal surface; (c) oxide film supported metal particles

1.2.1. Model catalyst preparation in UHV system

Generally speaking, oxide thin film epitaxial growth on single metal crystal can be divided into two categories: 1) directly oxidize the metal substrate to grow a native "passivated" oxide layer; 2) oxidize the deposited foreign metal in oxidative atmosphere. The first one is adopted in some limited examples in ultra-thin films like NiO(001) growth on Ni(001)[145], Al_2O_3(0001) on NiAl(110)[146], MoO_2 on Mo[147], some noble metal oxides, RuO_2 (110) on Ru (0001)[148-149], PtO_2 on Pt[150], IrO_2 on Ir[151] etc. Growth of these films is usually self-limited and the film thickness is hard to control.

Most widely used method to prepare the supported oxide thin films is the deposition of metals under oxidative atmospheres or metals' deposition followed by post-oxidation in higher temperature.

The preparation of well-ordered oxide films by deposition-oxidation method is often a trial-and-error process. The parameters including the substrate temperature during deposition, oxygen pressure, post-annealing temperature, are often difficult to optimize. In addition, lattice constants mismatch between the support and the oxide film is important to minimize the strain energy and form a well-ordered film. In terms of thermodynamics, the surface energy difference ($\Delta\gamma$) after oxide film growth on metal surfaces determines the growth process and the final film morphology, which can be described by equation:

$$\Delta\boldsymbol{\gamma} = \boldsymbol{\gamma_{oxide}} + \boldsymbol{\gamma_{interface}} - \boldsymbol{\gamma_{metal}}$$

γ is the surface(interface) energy which is derived from the energy excess due to disruption of surface bonds at the surface. There are three different oxide film growth modes as shown in **Figure 1-2** depended on the values of $\Delta\gamma$:

1) $\Delta\gamma>0$: Volmer-Weber (VW) mode

Stronger binding in between oxide than oxide film-metal substrate, leads to the formation of three-dimensional clusters from the onset. Further deposition will cause highly corrugated films.

2) $\Delta\gamma<0$: Frank-van der Merwe (FM) mode

Stronger oxide film-metal substrate interaction leads to two-dimensional, layer-by-layer growth. Oxide attaches preferentially to metal surface resulting in atomically smooth, dense films. This is the most common growth mode for oxide film growth on metal.

3) Stranski–Krastanov (SK) mode

This is like an "intermediate" growth regime, which is characterized by 3D island growth after the first layer(s) wetting the surface. Transition from the layer-by-layer to island-based growth occurs at a critical layer thickness which is dependent of the chemical and physical properties, such as surface energies and lattice parameters of the metal substrate and oxide film.

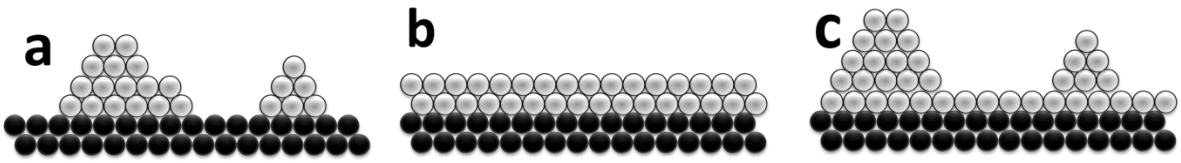

Figure 1-2. Cross-section views of the three primary modes of thin-film growth on metal

substrate including: (a) Volmer–Weber (VW: island formation), (b) Frank–van der Merwe (FM: layer-by-layer), and (c) Stranski–Krastanov (SK: layer-plus-island).

For metal supported on an oxide substrate, deposited metal particles can nucleate randomly or on specific oxide surface sites such as step edges, point defects or other energetically favorable sites. In general, the growth of metal on oxide follows the Volmer-Weber mode as mentioned above because of the comparative higher surface energy of metal than oxide. During deposition the metal can coalesce to bigger particles. Post-annealing could activate the sintering process by Ostwald ripening. The final morphology of the particle is strongly affected by the interaction with oxide substrate.

1.2.2. Surface reaction mechanisms

The main target for model catalyst research is to shed light on where and how the reaction proceeds in a real catalyst. The process includes the adsorption and desorption of gas molecules at a catalytically active surface, and interaction of these molecules with each other on this surface, as well as with the surface itself, may follow various reaction mechanisms.

Langmuir-Hinshelwood mechanism

The vast majority of catalytic reactions follow this mechanism, in which both reactants adsorb onto the surface of catalyst as the first step for reaction. The following surface diffusion facilitates interaction between adsorbed molecules. At last the reaction product desorbs from the surface. The reaction at the surface is often the rate limiting step. In this type of mechanism, the reactivity is highest when a stoichiometric amount of reactant is adsorbed on the single surface, and both reactants are fully intermixed on the catalyst's surface (**Figure1-3a**). However, the reactants may adsorb on different surfaces (components) of the catalyst, and the reaction can only happen at the interface (**Figure 1-3b**).

The CO oxidation reaction ($2CO+O_2 \rightarrow 2CO_2$) on Pt catalyst follow the Langmuir – Hinshelwood mechanism. It includes co-adsorption of O_2 and CO on Pt surface, dissociation of O_2, and the last formation and desorption of CO_2 to the gas phase.

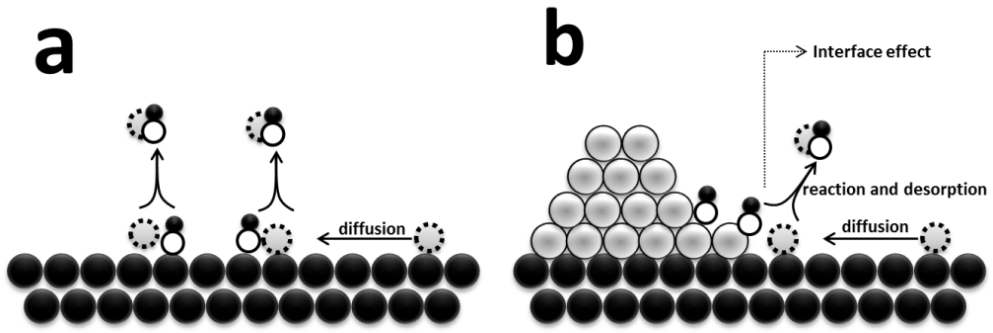

Figure 1-3. Langmuir-Hinshelwood mechanism: (a) single component catalysis; (b) multicomponent catalysis

Eley-Rideal mechanism

In this case, only one of the reactants adsorbs onto the catalyst surface, after which the other reactant interacts with the pre-adsorbed species directly from the gas phase, followed by the desorption of the reaction product. Higher coverage of the adsorbed species as well as a higher pressure of the other gas yields a higher reaction rate. An example of a reaction following this mechanism is the hydrogenation of CO_2 during formate (HCOO) synthesis, in which ambient CO_2 reacts with adsorbed hydrogen(H*) on the surface of Cu catalyst to produce formate (HCOO*) which desorbs subsequently[152]. The schematic process is shoed in **Figure 1-4.**

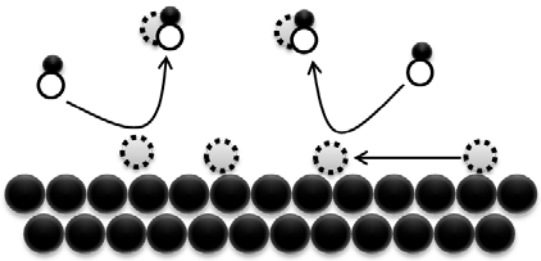

Figure 1-4. Eley-Rideal mechanism

Mars-van Krevelen mechanism

In this mechanism, the oxide surface itself is an active component in the reaction: firstly the reactant reacts with the catalyst surface, forming an oxidized product and then desorbs. Thus, the reduced oxide surface is oxidized by molecular oxygen or another oxidative gas in ambient to end the catalytic cycle. CO oxidation on the full covered FeO_2(111) film supported on Pt(111) surface follows the Mars-van Krevelen mechanism that FeO_2 supplies weakly bound O to directly oxidize CO in ambient and leaves O vacancy on the surface, which is then replenished by ambient O_2 to finish the catalytic cycle. [113-114, 153-154] The schematic process is shown in **Figure 1-5.**

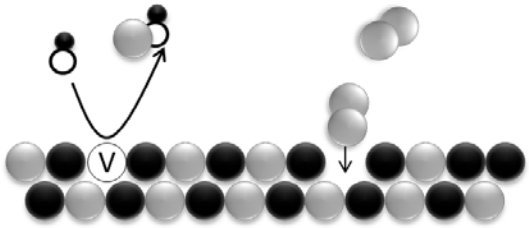

Figure 1-5. Mars-van Krevelen mechanism

1.3. Iron oxide: FeO and Fe_3O_4

Iron oxides are one of the abundant materials in the earth's crust. Because Fe can exhibit +2 and +3 valence states, Fe and O can form crystal structures of different stoichiometry, of which three types of oxides, Fe_2O_3, Fe_3O_4, FeO are stable at ambient conditions. In addition to the traditional source materials for iron and steel production, iron oxides are multi-functional materials and find applications in technology at various levels. Cornell and Schwartzman[155] gave a comprehensive review of the properties and applications of iron oxides and hydroxides. In model catalyst research iron oxide single crystals or well-ordered iron oxide thin films grown on metal single crystals by iron deposition and oxidation at high temperatures are used. We employed Fe_3O_4 and FeO thin films in this thesis.

1.3.1. FeO (Wüstite)

Bulk

Wüstite FeO has a rock-salt structure with lattice constant of 4.3 Å. O^{2-} anions form close-packed fcc sublattice and Fe^{2+} cations octahedrally coordinated to oxygen in the interstitial sites. The model structure of FeO is presented in **Figure 1-6a** and **b**. FeO is usually Fe-deficient, forming non-stoichiometric Fe_xO, with x ranging from 0.83 up to 0.95, which is caused by an oxidation of Fe^{2+} ions to Fe^{3+} in order to maintain the electrical neutrality. Wüstite is unstable at temperatures below 843 K, it disproportionates into metallic Fe and Fe_3O_4. Therefore, this oxide can be only prepared above 843 K and sequential quenching down to room temperature[155].

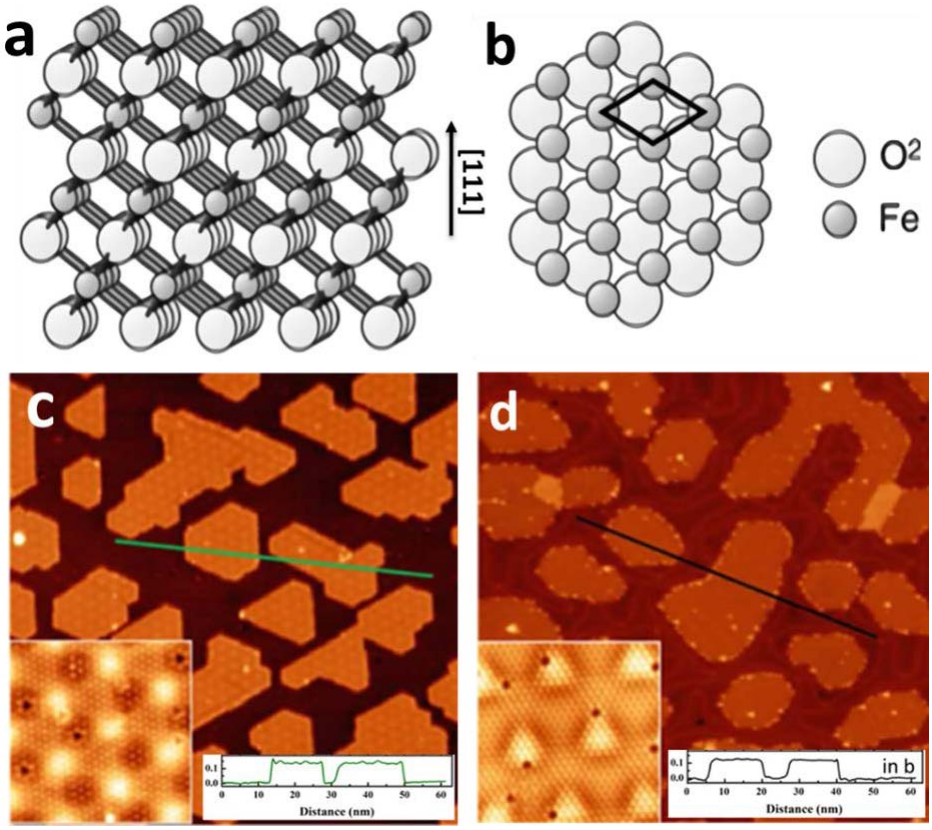

Figure 1-6. Side view (a) and top view (b) of wüstite FeO(111). STM images[156] (86 × 86 nm^2)of 0.5ML FeO(111) on Pt(111) with Moiré periodicity of ~25 Å (c) and FeO(111) on Au(111) with Moiré periodicity of ~35 Å (d). Insets in (c, d) are atomic resolution images and the corresponding scanning profiles along the lines.

Thin films on Pt(111) and Au(111)

In this thesis, FeO(111) thin films are studied supported on Pt(111) and Au(111). FeO/Pt(111) consists of one atomic layer of iron on top and one atomic layer of oxygen at the bottom. Both O and Fe planes have an atomic periodicity of 3.11 Å (3.04 Å in the bulk). ~12 % mismatch between FeO(111) and Pt(111) (2.77 Å at the surface) makes the film exhibit a Moiré pattern which has a periodicity of ~25 Å as shown in **Figure 1-6b**. As the result of surface polar relaxation, the height of 1 ML FeO(111) / Pt(111) is ~2.5 Å and the Pt-Fe and Fe-O interlayer distances are 1.89 Å and 0.62 Å, correspondingly, the Fe-O distance in bulk FeO is 1.25 Å. The film is O terminated which determines its inertness. FeO(111) thin film can grow layer-by-layer on Pt(111) only up to ~2.5 ML, then a three-dimensional growth (Volmer-Weber mode) of Fe_3O_4(111) islands becomes favorable[102].

FeO(111) grown on Au(111) behaves slightly differently. Because of the larger lattice constant of Au(111) (2.88 Å at the surface), FeO/Au(111)'s atomic periodicity of 3.3 Å is also larger than the one on FeO/Pt(111). Correspondingly, the Moiré pattern periodicity increases to ~30 Å as shown in **Figure 1-6d**. Fe-Au binding is

much weaker than Fe-Pt, the termination of Fe-O bilayer on Au(111) is still unclear. Theoretical calculations presented the Fe-terminated surface to be more stable than the O-terminated surface at low pressures, but this conclusion is still not proven by experiments[157].

1.3.2. Fe_3O_4 (magnetite)

Bulk

Fe_3O_4 has an inverse spinel structure. The cubic unit cell includes eight formula units $(Fe^{3+})_{tet}(Fe^{2+}Fe^{3+})_{oct}O^{2-}{}_4$ with a lattice constant of 8.396 Å. As shown in Figure 1-3, on the [001] direction, the structure can be viewed as alternating stacking of Fe_{tet} layers (A layers) and $Fe_{oct}O_2$ layers (B layers), rotated by 90° and shifted by 1/4 of a lattice constant after each double-layer. The tetrahedral sites are exclusively occupied by Fe^{3+} cations, while Fe^{2+} and Fe^{3+} coexist on sites with octahedral coordination. This arrangement of iron is energetically preferable regarding the crystal field energy of Fe^{2+}, which favors the octahedral coordination site. The conductivity of Fe_3O_4 facilitates the STM observation when it's employed as single crystal or thick film grown on metal single crystal. With temperature increasing, the distinction between Fe^{2+} and Fe^{3+} sites breaks down as a consequence of the conductivity of magnetite along the rows of Fe_{oct}. The conduction behavior is described as a mixture of band conduction and small-polar-on hopping, with increasing importance of polar on hopping at elevated temperatures [158].

In surface science the low-index surfaces of Fe_3O_4 have been intensively studied and the (111) and (001) surfaces are the most stable low-index magnetite surfaces. The Fe_3O_4 (111) surface has a hexagonal lattice with a periodicity of 5.94 Å, and the nearest distance in oxygen sublattices is 2.97 Å. The step height is 4.85 Å which corresponds to a distance between equivalent (111) terminations. However, the exact surface terminations of Fe_3O_4(111) are still a matter of discussion. LEED studies performed on Fe_3O_4(111) thin films grown on Pt(111) and STM results suggested a termination with a 1/4 monolayer of tetrahedrally coordinated Fe^{3+} ions over a close-packed oxygen layer (Fe_{tet})[159-160]. A surface stability diagram based on density functional theory (DFT) calculations [161-162] also suggested the Fe_{tet}-terminated surface to be most stable at experimentally relevant pressures and temperatures. However, study of CO adsorption and recent water interaction with Fe_3O_4(111) were both rationalized in terms of a surface terminated by octahedrally coordinated iron ions. Combined TPD, IRAS (Infrared Reflection Absorption Spectroscopy) and DFT calculation for CO adsorption on Fe_3O_4(111), latest study confirmed the reasonability of Fe_{tet}-termination [163].

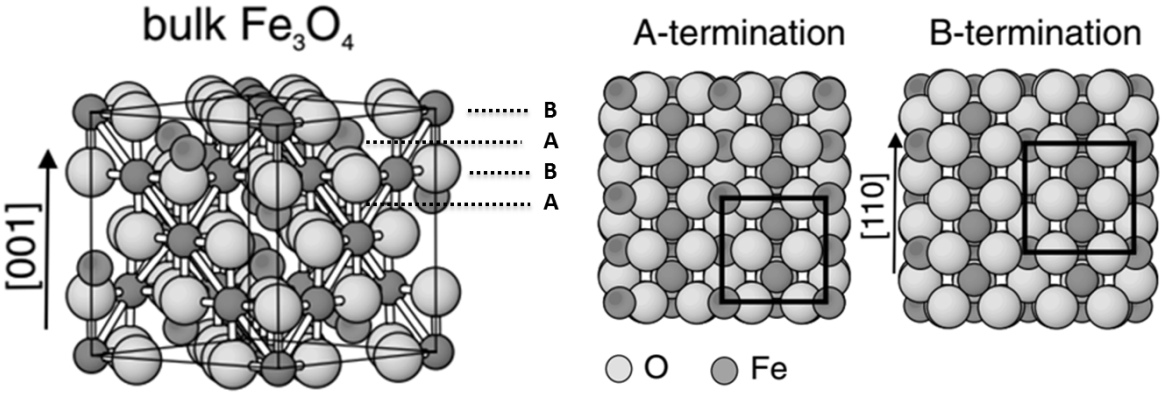

Figure 1-7. The inverse spinel structure of magnetite together with a top view of the two bulk truncations of $Fe_3O_4(001)$ with an A and a B layer, respectively.

In the [001] direction, the layers of tetrahedral iron atoms are denoted as A-layers (Fe^{3+}_{tet}) and the mixed octahedrally coordinated iron and oxygen layers are termed B layers ($Fe^{2+}_{oct}Fe^{3+}_{oct}O_4$) as shown in **Figure 1-7**. It is well established that the $Fe_3O_4(001)$ surface exhibits a $(\sqrt{2}\times\sqrt{2})R45^o$ reconstruction[164-166]. The first atomically resolved STM images of the $Fe_3O_4(001)$ showed undulating rows of Fe atoms along the (110) directions, suggesting a B-layer termination which consists of a layer of octahedrally coordinated iron and tetrahedrally coordinated oxygen, along with one oxygen vacancy per unit cell[165, 167]. The surface phase diagram constructed in the framework of ab initio thermodynamics revealed that a modified B-layer is stabilized over a broad range of oxygen pressures. Instead of an order of surface defects in previously proposed models, In 2005, Pentcheva et al[168]. proposed a structural model for the B-layer termination based on a relaxed Jahn-Teller distortion of a bulk-terminated surface unit cell, that is, a wavelike displacement of Fe and O atoms in the top B layer, whereby the $(\sqrt{2}\times\sqrt{2})R45^o$ superstructure is formed. It has been broadly accepted as the correct surface structure, explaining the experimental observations including quantitative structural analyses using surface X-ray diffraction[168] and LEED[169]. Recently a new structural model based on an ordered array of subsurface Fe vacancies was suggested by Bliem et al[170]. The characteristic Fe cation rearrangement of this structure model creates a strong preference for metal adsorption in one specific site per unit cell. Thus these adatoms are found to be thermally highly stable up to an annealing temperature of 700 K[171].

Another termination with $(\sqrt{2}\times\sqrt{2})$ $R45^o$ symmetry is also possible under excess-Fe conditions. It typically presents Fe(A) dimers on the surface and is equivalent to a polarity-compensated half-filled A-layer termination or a "dimer" termination. It's firstly predicted by molecular dynamics simulations[172]. This termination can be obtained by iron deposition on an initially B-terminated surface [173].

Fe_3O_4(001) thin films

The preparation of Fe_3O_4(001) thin films usually employs MgO(001) as a substrate due to the low lattice mismatch[174-179]. Diebold and coworkers [179] prepared 1mm-thick Fe_3O_4 (001) thin films with $(\sqrt{2} \times \sqrt{2})$ R45° reconstruction but the high temperature annealing caused segregation of substrate Mg to the surface. Korecki and coworkers deposited ~20nm Fe(001) film prior to the preparation as a buffer layer to prevent Mg atoms' migration but the Fe segregation resulted in the "dimer" termination above mentioned. The distance between the dimer centers is 12 Å, whereas the atoms in a dimer are spaced by 4.9 Å, as compared to the 5.96 Å distance between the tetrahedral Fe^{3+} ions in the bulk A-layer. Fonin et al.[175] prepared clean B-terminated Fe_3O_4 (001) thin films on MgO(001) with moderate substrate temperatures of about 300℃ to prevent magnesium diffusion in maintained O_2 pressure. The average step height of the film was found to be ~ 2.1Å, corresponding to the distance between adjacent A-A or B-B planes of the bulk Fe_3O_4 structure. The rows run along the [011] direction in a "wavelike" where the distance between two rows is about 6Å. All these features are in coincidence with the (001) surface of single crystal Fe_3O_4 as shown in **Figure 1-8**.

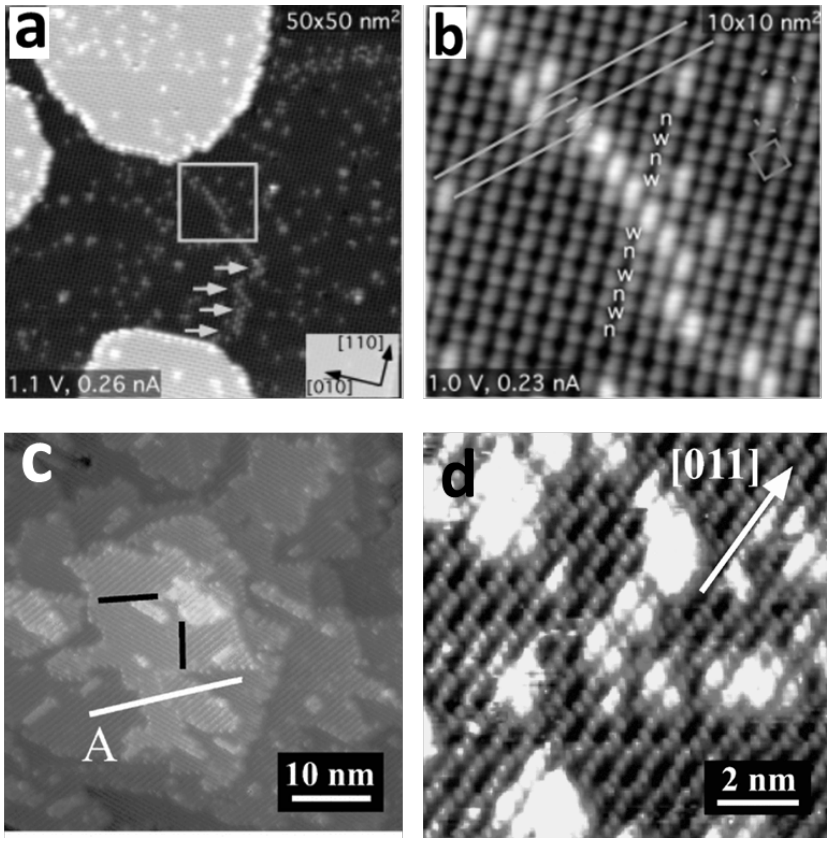

Figure 1-8. (a, b) STM images of the (001) surface of single crystal Fe_3O_4.[180] (b) is the high-resolution STM image of the area contained within the square in panel. (c, d) STM images of Fe_3O_4(001) film grown on MgO(001). [175]

Chapter 2.
Experimental Methods

2.1. Ultra-high Vacuum (UHV)

UHV means a pressure lower than 10^{-9} mbar. Vacuum conditions are necessary to provide mean free path of electrons/ions large enough to permit the use of low energy electron and ion-based experimental techniques without undue interference from gas phase scattering. In addition, adsorption from the residual gases present in the chamber which modifies the surface under study must be minimized during the time of experiment which needs UHV conditions.

According to the kinetic theory of gases, the number of gas molecules impinging on the surface is:

$$\mathbf{R} = \frac{\mathbf{dN}}{\mathbf{dt}} = \frac{\boldsymbol{P}}{\sqrt{\boldsymbol{2\pi mkT}}} = \frac{\mathbf{2.635 \times 10^{22} P_{mbar}}}{\sqrt{\boldsymbol{MT}}}\,\boldsymbol{cm^{-2}s^{-1}}$$

Where m is the molecular mass in kg and M is the molecular mass in units of the atomic mass constant. For a pressure of 10^{-9} mbar and a temperature of 300K, the main kinds of residual gas in the chamber present as follows:

Molecule	H_2	H_2O	CO	O_2	CO_2
M	2	18	28	32	44
R($cm^{-2}s^{-1}$)	1.1×10^{12}	3.6×10^{11}	2.9×10^{11}	2.7×10^{11}	2.3×10^{11}

With the precision of one order of magnitude a surface has 1015 atoms per square centimeter. This means that if every gas molecule at the above conditions adsorb on the surface (the sticking coefficient is unity) the surface remains clean for about one hour which is sufficient to perform an experiment.

Another parameter to describe vacuum is the mean free path of the molecules at a given pressure, which is the mean distance before collision with another molecule

$$\boldsymbol{\lambda} = \frac{\mathbf{kT}}{\sqrt{\mathbf{2}}\boldsymbol{\pi}\boldsymbol{\xi}^{\mathbf{2}}\mathbf{P}}$$

Where ξ is the molecular diameter. For typical UHV pressures the mean free path of the molecules is several meters.

In order to achieve UHV conditions, two steps of pumping are needed for the chamber in general. A rough pump is used to pump the system down to the 10^{-3}mbar

range. The pump of choice for the second stage is a turbo-molecular pump. The gas molecules collide with the fast-moving rotor of turbo-pump and thereby attain an impulse in the direction of the rough pump. In order to achieve efficient pumping, the speed of the rotor has to achieve up to 90 krpm (1500Hz).

Once a low pressure range has been reached, the ion pump can be used to maintain it. The residual gas in ion pump is ionized by a plasma discharge due to the high voltage between anode and cathode. The ionization probability is increased by the presence of the magnetic field which makes the electrons travel on spiral trajectories. When the ions hit the titanium cathode they can be buried in it or react with it. The ion pump does not remove the residual gas from the system. Typically, an ion pump is operated at pressures below 10-8 mbar.

In addition, the Titanium sublimation pump is employed, in particular for hydrogen. It consists of a titanium filament through which a high current (typically around 50 Amps) is applied, which causes the filament to reach the sublimation temperature of titanium, and hence the surrounding chamber walls become coated with a Ti film, residual gases in the chamber are likely to react and to form a stable, solid product. In order to reach UHV conditions, it is necessary to bake out the chamber at 150-200°C for 12-24h.

Experimental setup

The experiments of this thesis were performed in an Omicron Ultra-High Vacuum (UHV) system “MULTI PROBE COMPACT” as shown in **Figure 2.1**. It consists of three parts: a “main chamber”, a “STM chamber” and a home-built high-pressure cell (“HP cell”), all separated by gate valves. Two manipulators were cross-mounted to move the sample between the chambers. The main manipulator positions the sample in main chamber and moves the sample to STM chamber in combined with a wobble stick. The magnetic transfer rod slides between the main chamber and the high-pressure cell. The whole system was placed on an electronic vibration isolation system (Herzan) in order to reduce the influence of mechanical noise on STM measurements. The whole system can be baked to maximum temperature up to 170 °C to recover the UHV as before the chamber is opened.

The main chamber was equipped with sample cleaning, preparation and surface science characterization instruments. The sample can be heated up to 1300 K and cooled down to ~100K on the main manipulator. Gas inlets supply gases in the pressure range of 10^{-5}-10^{-10}mbar monitored by gauges. The HP cell was constructed for sample treatment in reaction conditions. The sample stage can be heated up to ~500K in the pressure range of 10^{-8}-20mbar typically. The STM chamber was equipped with Omicron GmbH MICRO H high-pressure STM. In-situ scanning is possible in pressure up to several mbar at room temperature. The detailed equipment configuration is listed in the table below.

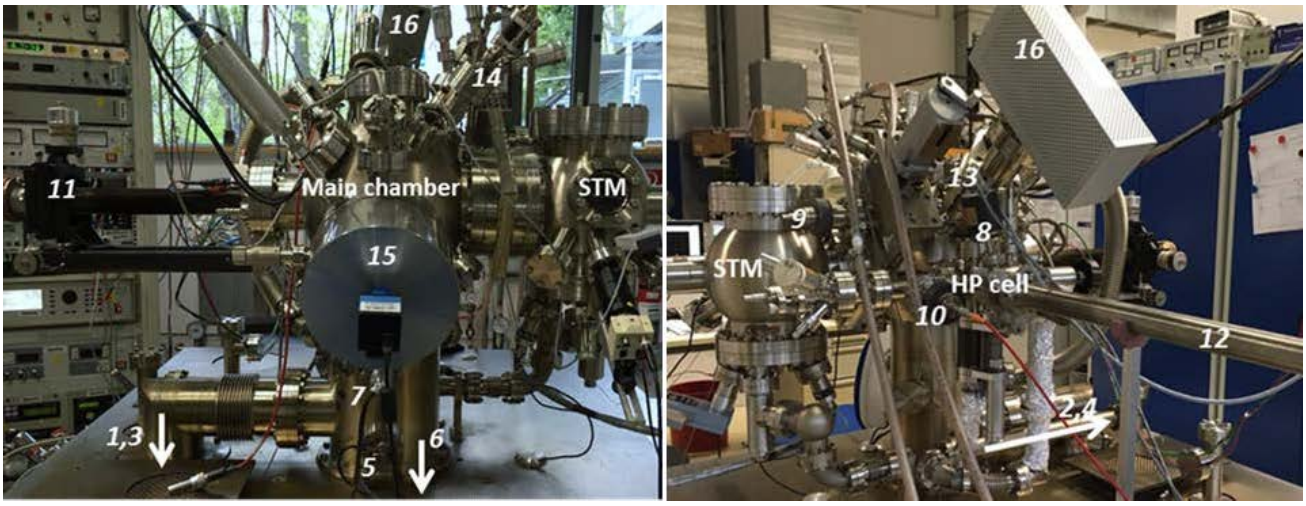

Figure 2-1. The UHV system, the indicating numbers correspond to table in below.

Functional unit	Category	Component
UHV system	Pump	Rough pump (BOC Edwards) [1,2]
		Turbo (Pfeiffer) [3,4]
		Ion pump (Varian) [5]
		TSP (Varian) [6]
	Valve	Gate valve
		Leak valve
	Gauge	Ion gauge (Omicron) [7]
		MKS Baratron® gauge8
		cold cathode gauges (Varian) [9,10]
Sample Processing and Preparation	Positioning and Transfer	Main manipulator [11]
		Magnetic transfer rod (Omicron) [12]
	Cleaning	Sputtering gun (Ion Source IQE 11/35, SPECS) [13]
	Deposition	Evaporator (EFM3, Omicron) [14]
	Annealing	Homemade W-Th filament
		150W halogen lamp (OSRAM)
Analysis	STM	MICRO H high-pressure STM (OMICRON)
	LEED/AES	ErLEED (SPECS) [15]
	QMS	Hidden HAL7 gas analyzer [16]

2.2. Surface Analytical Techniques

2.2.1. Scanning Tunneling Microscopy (STM)

Scanning tunneling microscopy (STM) is the main experimental technique employed in the present work. This technique provides real-space imaging of flat,

conductive surfaces with atomic resolution. STM was invented by Gerd Binnig and Heinrich Rohrer at IBM Zürich in 1981[181]. The discovery was awarded the Nobel Prize in Physics in 1986. The microscope is a member of Scanning Probe Microscopy (SPM) family in which a physical probe scans the surface in an ordered manner, recording the probe-surface interactions (for example the tunneling current in case of STM and atomic forces in case of Atomic Force Microscope (AFM), thus creating an image (topography, current map, etc.) of the surface.

Theory of STM

The microscope is based on the quantum tunneling effect. Tunneling is a concept that arises from quantum mechanics. In classical mechanics an electron moving in a potential U can be described by equation:

$$\frac{\boldsymbol{P^2}_{\boldsymbol{d}}}{\boldsymbol{2m}} + \boldsymbol{U(d)} = \boldsymbol{E}$$

Where P_d is the electron's momentum, m is the electron's mass, U(d) is the potential value at position d and E is the electron's energy. The equation is true only for E > U(d) because only then the electron has a non-zero momentum. It means that in classical theory the electron cannot move to a region where E < U(d). However, in quantum mechanics any particle, such as the electron, has wave-like characteristics. The state of the particle is described by a wave function ψ(d). Assuming the 1-dimensional case in the presence of a potential U(d), the energy levels ψ(d) of the electron are given by solutions to Schrödinger's equation:

$$-\frac{\hbar^2}{\boldsymbol{2m}}\frac{\boldsymbol{\partial^2\psi(d)}}{\boldsymbol{\partial d^2}} + \boldsymbol{U(d)\psi(d)} = \mathbf{E}\boldsymbol{\psi(d)}$$

Where ħ is the reduced Planck's constant. In the classically allowed region the solutions are:

$$\boldsymbol{\psi(d)} = \boldsymbol{\psi(0)e^{\pm i\mathcal{K}d}}$$

Where ψ(0) is the wave function of the surface state of the sample at d=0 and

$$\boldsymbol{\mathcal{K}} = \frac{\sqrt{\boldsymbol{2m(E-U)}}}{\hbar}$$

is the wave vector. In the classically forbidden region quantum mechanics predicts an exponential decaying solution for the electron wave function.

For a rectangular barrier, it has a form:

$$\boldsymbol{\psi(d)} = \boldsymbol{\psi(0)e^{\pm\mathcal{K}d}}$$

Where

$$\boldsymbol{\mathcal{K}} = \frac{\sqrt{\boldsymbol{2m(U-E)}}}{\hbar}$$

is the decay constant. In special cases the electron can penetrate through the barrier in a process referred to as tunneling. This can take place in case of a very small barrier width, when a bias between two sides of the barrier is applied. The probability P of the electron appearing at distance d is proportional to the wave function squared:

$$\mathbf{P} \propto \left(\boldsymbol{\psi_n}(\mathbf{0})\right)^2 \boldsymbol{e}^{-2\mathcal{K}\mathbf{d}}$$

Where ψ_n is a wave function of an electron with energy E_n. Experimentally, the tunneling effect can be observed between conductors separated by a very small width of isolator when a bias V is applied between the conductors. In STM the effect occurs between the scanning tip and the conducting sample. The tip is a sharp metallic needle. The separating potential barrier is typically a space of vacuum. A schematic drawing of a one-dimensional metal-vacuum-metal tunneling junction on these an example of STM is shown in **Figure2-2**.

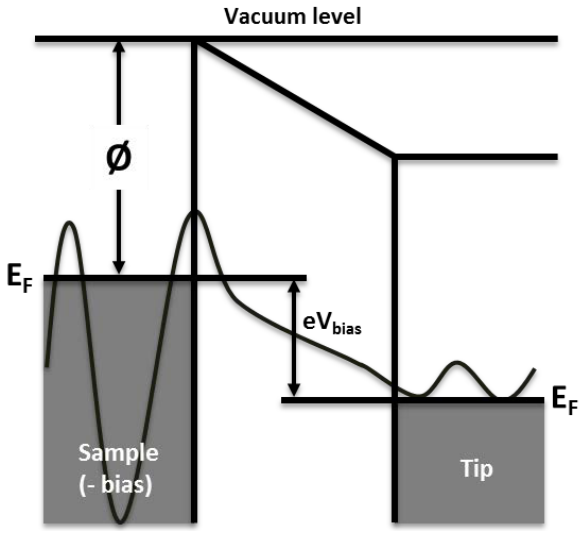

Figure 2-2.The principle of tunneling between the surface and the metal tip (minus sample bias)

In the context of electron distribution on different energy states, tunneling current can be evaluated by summing over all the relevant states including the number of electrons on sample surface and the number among them which have corresponding free states to tunnel into on the tip. At any finite temperature, the electrons in both sides (sample and tip） follow the Fermi distribution. With a bias voltage (–V) on sample, the total tunneling current is:

$$\mathrm{I} = \frac{4\pi e}{\hbar}\int_{-\infty}^{\infty}[f(E_F - eV + \varepsilon) - f(E_F + \varepsilon)] \times \rho_{sa}(E_F - eV + \varepsilon)\rho_t(E_F + \varepsilon)\,|M|^2 d\varepsilon$$

Where f(E) is the Fermi distribution function, and $\rho_{sa}(E)$ and $\rho_t(E)$ are the density of states (DOS) of the sample and tip at energy E. M is the tunneling matrix element, which is constant on a certain (sample-tip) system.

If kT is smaller than the energy resolution required in the measurement, then the

Fermi distribution function can be approximated by a step function. In this case, the tunneling current is

$$\mathrm{I} = \frac{4\pi e}{\hbar}\int_0^{eV} \rho_{sa}(E_F - eV + \varepsilon)\rho_t(E_F + \varepsilon)\,|M|^2\,d\varepsilon$$

In real STM experiment, the tip scans over the sample surface. During a scan, the condition of the tip usually does not vary. The electrons coming to the tip surface have a constant velocity to flow into the tip, thus the tunneling current is directly proportional to the number of states on the sample surface within the energy interval eV near the energy E_F, which are mainly responsible for the tunneling current at measuring temperature. The number of states depends on the local nature of the sample surface. For metals, it is finite. For semiconductors and insulators, the number is very small or zero. For semimetals, it is in between. By including all the sample stales in the energy interval eV, the tunneling current[182]:

$$\mathrm{I} \propto \sum_{En=E_F-eV}^{E_F} |\Psi_n(0)|^2 e^{-2\kappa d}$$

If V is small enough that the density of electronic states not vary significantly within it. Combining upward two equations, the current can conveniently be written in terms of the local density of states at the Fermi level as:

$$\mathrm{I} \propto \mathrm{V}\rho_{sa}(0, E_F)e^{-2\kappa d} \approx \mathrm{V}\rho_{sa}(0, E_F)e^{-1.025\sqrt{\Phi}d}$$

Where the barrier height ϕ is in [eV] and d in [Å], V is the bias voltage. With 5eV as typical value for a work function value, a change of 1Å in distance causes a change of nearly one order of magnitude in current. This facilitates the high vertical resolution of STM.

The microscope

A schematic drawing of the scanning tunneling microscope (STM) is shown in **Figure 2-3**. The working procedure is as follows: the metallic tip, usually made of W or Pt-Ir alloy wire (usually cut or electrochemically etched), is being approached to the sample until a distance of 0.5-1 nm and then a voltage bia, typically of few mV up to few V typically, is applied between them. Because of the very small distance and the applied potential difference, the electrons can tunnel from the tip to the sample (or vice versa, depending on the bia's polarity), which results in a flow of tunneling current. The tip is attached to a scanner made of piezoelectric elements (ferroelectrics with perovskite structure ABO_3, for example $PbTiO_3$). The specificity of these materials is that the length of the element changes, if voltage is applied to its walls (due to polarization of the dipoles inside the material).

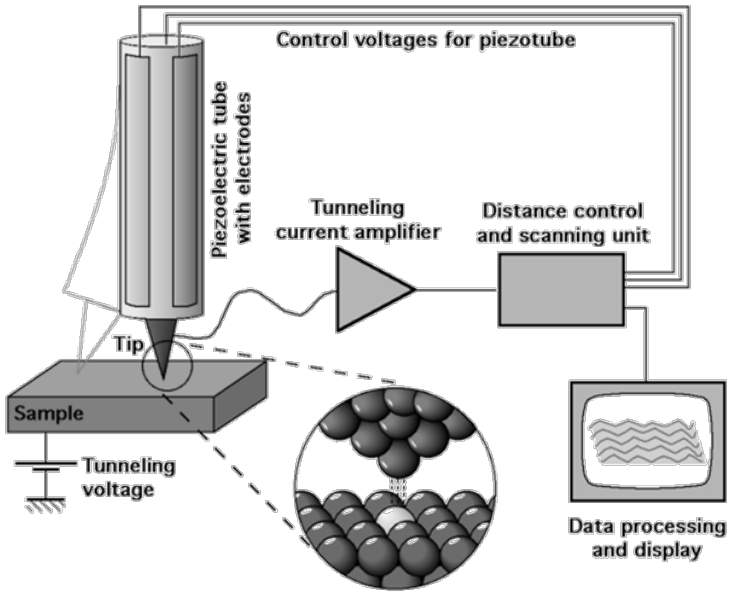

Figure 2-3. Schematic representation of a scanning tunneling microscope (Figure from Michael Schmid, TU Wien[183])

In our system, the microscope (**Figure 2-4**) is Omicron MICRO H high pressure STM working in constant current mode under the operation of SCALA Pro 5.0 software. The tip was Pt-Ir (LOT-Oriel GmbH). The sample was inserted upside-down into the STM and the tip was approaching the sample from the bottom. The sample stage was placed on three ball-bearing piezo carriers which allowed the stage/sample movement in x and y direction. A tube geometry piezoelement was responsible for the precise adjustment of the tip position in z-direction and for the tip scanning in x/y-direction. This kind of tip position control results in a very high lateral resolution of 0.1nm.

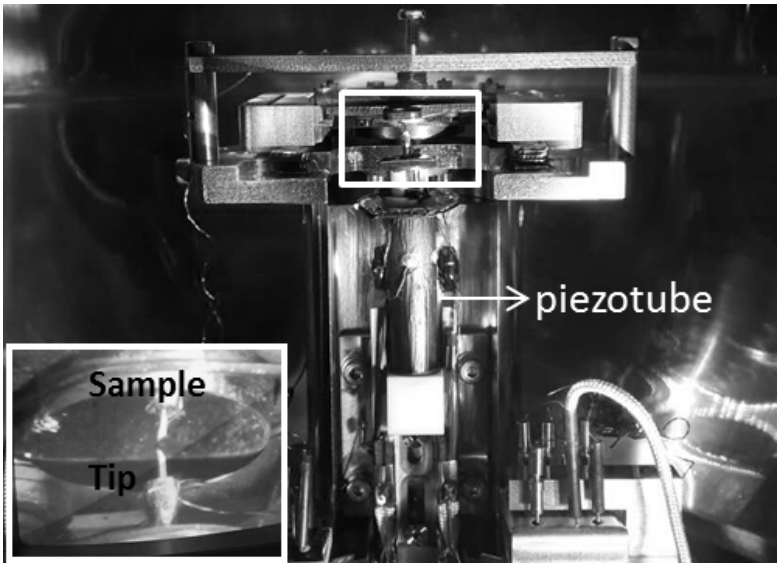

Figure 2-4. Omicron MICRO H STM head

During measurement, the tip moves across the surface of the sample in the x-y plane. The changes in surface height (corresponding to tip-sample distance), as well as the changes in the density of electron states in different regions of the sample, finally result in changes in the tunneling current. Scanning tunneling microscopes typically operate in two modes:

1) ***Constant current mode:*** By using a feedback loop the tip is vertically adjusted in such a way that the current always stays constant. As the current is proportional to the local density of states, the changes in the z and the deviations of the tunneling current are being recorded by a computer. In this way, a topographic image of the surface, as well as the corresponding current map, are created as the tip follows a contour of a constant density of states during scanning. For all STM experiments presented in this work, the constant current mode is used.

2) ***Constant height mode:*** In this mode the vertical position of the tip is not changed, equivalent to a slow or disabled feedback. The current as a function of lateral position represents the surface image. This mode is only appropriate for atomically flat surfaces as otherwise the high surface corrugation would cause tip crash. One of its advantages is that it can be used at high scanning frequencies (up to 10 kHz). In comparison, the scanning frequency in the constant current mode is about 1 image per second or even per several minutes.

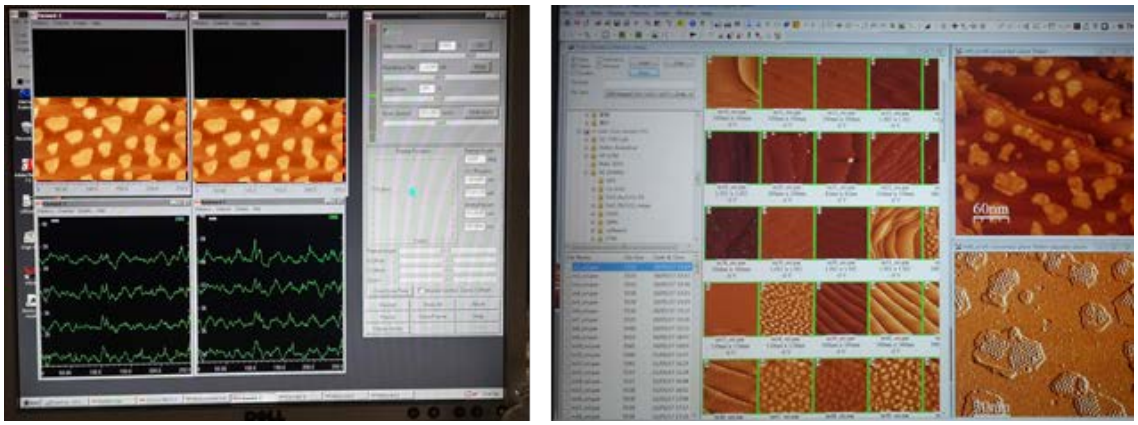

Figure 2-5.Graphical user interface of SCALA Pro 5.0 (lift) and WSxM 5.0 develop 8.4(right).

The Data acquiring are performed on computer with SCALA Pro 5.0 as shown in **Figure 2-5a.** The image is created in a line-by-line manner, with a scanning direction up or down, from left to right or from right to left. Tunneling parameters are very important to get high quality images and they are controlled by the user. The gap voltage (V; in [V]) sets the voltage bias which is applied between the tip and the sample and gives possibility to define the direction of the tunneling current flow (negative vs. positive voltage values). The tunneling current feedback setpoint (I; in

[nA]) allows the definition of the tunneling current setpoint for the feedback loop. The scan area, which is in a form of a square, can be defined in[nm]. During scanning, the tip can be modified by applying single spot pulses or intentional striking to get a better tip state for imaging.

The acquired data is saved in the form of a raster image with a typical resolution of 256^2 or 512^2 pixels (measurement points). The acquired STM images can be processed and analyzed using the software WSxM, for example applying image noise filters, measuring the distances and height profiles, performing roughness and coverage statistical analyses, Fast Fourier Transform (FFT) and so on.

2.2.2. Low Energy Electron Diffraction (LEED)

Low Energy Electron Diffraction (LEED) is an experimental technique based on wave-like nature of low energy electrons (20-200eV) at the surface of crystalline materials. It allows distinguishing different surface crystal structures by monitoring the angular dependence of the electrons which are backscattered from the atoms at the crystal surface. LEED is the principal technique for the determination of the ordered structures on the surface.

The theory of wave-like nature of all particles was first introduced by Louis de Broglie in his PhD thesis in 1924. This means that the particles, including electrons, undergo the effects associated with waves, such as diffraction or interference. This hypothesis, based on Albert Einstein's and Max Planck's works, was awarded the Nobel Prize in Physics in 1929. De Broglie's theoretical work initiated a series of experiments on particles diffraction and interference. In 1927 Davisson and Germer [184]discovered that a monochromatic beam of low energy electrons shot onto a crystalline nickel target surface is elastically backscattered on the high electron density regions, namely the surface atoms, and the intensity of the backscattered electrons have an angular dependence, forming a diffraction pattern. The theoretical explanation for the formation of diffraction patterns from crystal structures is as follows: Coming from de Broglie's equation for the electron's wavelength, the wavelength's dependence on the electron's kinetic energy (determined by the electron beam energy) can be derived:

$$\boldsymbol{\lambda = \frac{h}{P} = \frac{h}{\sqrt{2mE_k}} = \frac{h}{\sqrt{2meV}}}$$

Where λ is the wavelength, $\mathbf{h} = 6.626\times10^{-34}\,Js$ is the Planck's constant, p is the electron's momentum, E_k is the electron's kinetic energy, $m = 9.11\times10^{-31}\,kg$ is the electron mass, $e = 1.6022\times10^{-19}\,C$ is the electron charge and V is the beam energy (20-200V). This means that a beam of low energy electrons results in a small wavelength λ in the range of 2.7 Å-0.87 Å, this is of a size of interatomic distances in a

crystal lattice (< 3 Å), which is why interaction of such electrons with ordered surfaces should result in diffraction.

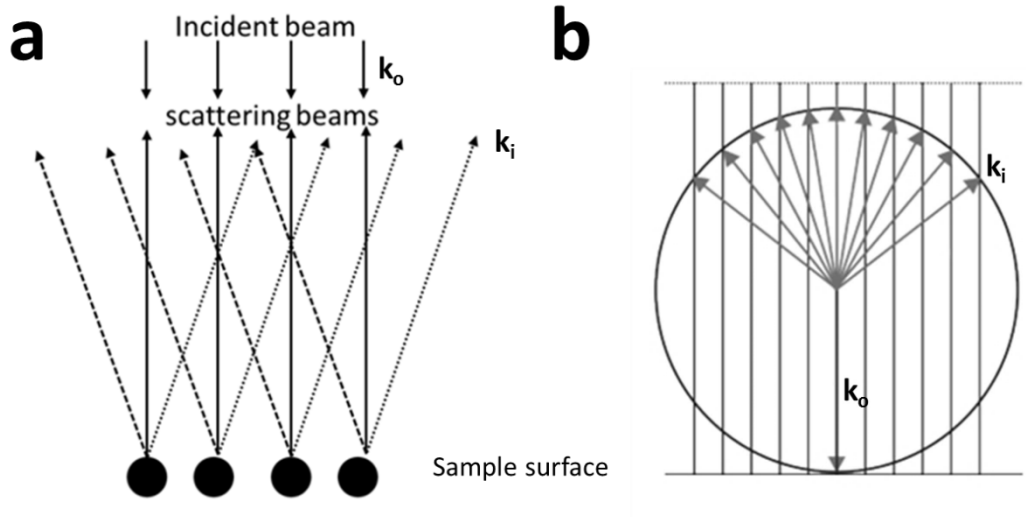

Figure 2-6. (a) Schematic drawing of electron scattering at the crystal surface; (b) The Ewald construction for the low energy electron's surface scattering.

The process and principle of low energy electron diffraction at the crystal surface is schematically shown in **Figure 2-6**. The electrons scattered from a surface give an interference pattern with constructive interference in the directions for which the different path lengths of the electrons are integral multiples of the electron wavelength. In reciprocal space, the diffraction condition is graphically represented by the construction of the Ewald sphere as shown in **Figure 2-6b**. For an incident electron with wave vector:

$$\left|\overrightarrow{k_0}\right| = \frac{2\pi}{\lambda_0}$$

and a scattered wave vector:

$$\left|\vec{k}\right| = \frac{2\pi}{\lambda}$$

Diffraction takes place when the sphere with radius of $2p/\lambda_0$ ray intercepts a node of the reciprocal lattice of the crystal. The diffraction pattern obtained then makes it possible to visualize the reciprocal space of the studied surface.

The basic reason for the high surface sensitivity of LEED is that for low-energy electrons the interaction between the solid and electrons is especially strong. Upon penetrating the crystal, primary electrons will lose kinetic energy due to inelastic scattering processes such as plasmon- and phonon excitations as well as electron-electron interactions. The inelastic processes are commonly treated by assuming an exponential decay of the primary electron beam intensity (I_0), thus it's

intensity in the direction of propagation is:

$$\mathrm{I(d)} = I_0 \times e^{-d/\Lambda(E)}$$

Where d is the penetration depth and $\Lambda(E)$ denotes the inelastic mean free path, defined as the distance an electron can travel before its intensity has decreased by the factor 1/e. In this case the mean free path turns out to be in the rage of 5-10 Å with the energy range of low-energy electrons (20-200 eV). This effective attenuation means that only a few atomic layers are sampled by the electron beam and as a consequence the contribution of deeper atoms to the diffraction progressively decreases.

A schematic drawing of low energy electron diffractometer (LEED) set up is shown in **Figure2-7a**. The standard LEED apparatus comprises a hemispherical fluorescent screen and an electron gun aligned along the central axis of the screen. The sample is placed in front of the electron gun. Electrons of low energy below 300 eV are emitted from the filament with low work functions (LaB_6, W or Ir), which then follow paths along the central axis and finally hit the sample at earth potential in order to prevent charging. The electron beam used has typically a beam diameter of around 1 mm^2. The instruments transfer width (which is essentially the coherence length of the electrons) is of approximately 5-10 nm in modern instruments. Naturally only structures with the extent of at least (100 x 100) Å can produce Bragg reflexes. Structure domains with a smaller diameter than the coherence width will not constructively add to the diffraction pattern but add diffuse background intensity.

The incident electrons are scattered by the surface atoms and the back-scattered electrons are then accelerated sharply onto the screen which is biased to 3-6 kV. The grids in front of the screen provide accurate energy selection to screen out the inelastically scattered electrons. Then a clear diffraction pattern is formed which can be observed directly (by eye) or recorded with a camera.[185]

The LEED patterns are shown in a form of bright diffraction spots on a dark background. The positions and distances between the spots are characteristic for a specific crystallographic structure and the intensities of the spots and the background reflect the quality of the structure. It's convenient to denote by Ewald sphere as shown in **Figure2-7b.**

The sphere has a radius $|\overrightarrow{k_0}|$ and the upper half of the sphere can be considered as the hemispherical fluorescent screen of the LEED apparatus. By default, the incident wave vector $\overrightarrow{k_0}$ lies parallel to electron incidence and the reverse direction diffraction is the reason for the central spot which is marked as [00] spot. The diffraction wave vectors coincide with the Laue condition and form diffraction spots on the fluorescent LEED screen. These spots are numbered by their *hk* value and are named in a matrix notation (spots [01], [10], [11], etc**)**. Note that only the elastically scattered electrons contribute to the pattern. In order to eliminate the inelastically scattered electrons only contributing to the background, a system of grids with regarding potential is positioned on the electrons way to the screen so that only the

electrons with a given energy can pass through the grids.

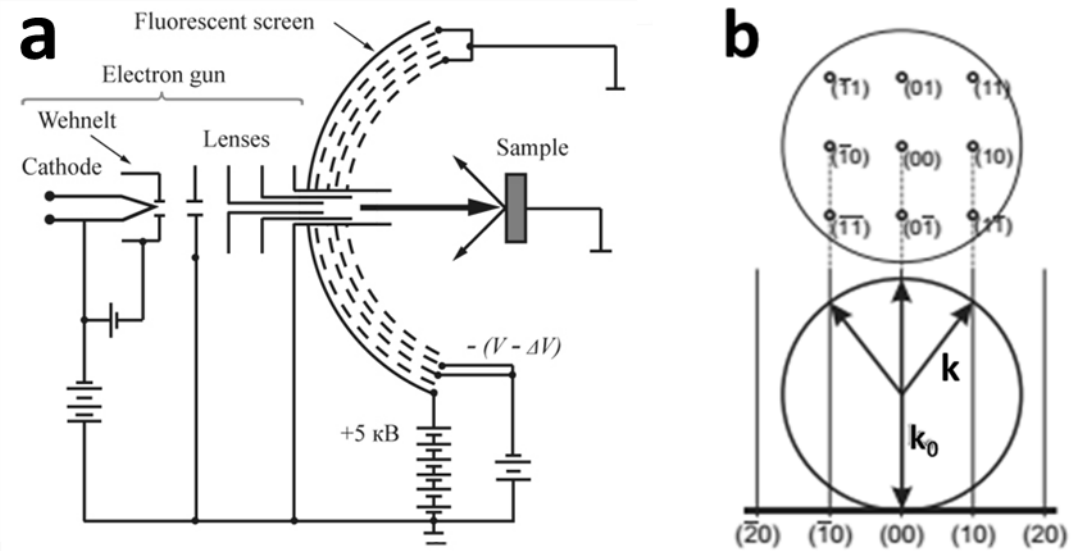

Figure 2-7. (a) Schematic drawing of a Low Energy Electron Diffractometer; image from[186]; (b) labeling of LEED spots in Ewald construction for LEED.

2.2.3. Auger Electron Spectroscopy (AES)

Auger electron spectroscopy (AES) is a surface-sensitive spectroscopic technique based on the so-called Auger effect. The technique allows to determination of chemical composition at the surface of sample by investigating the energies of the Auger electrons emitted from the sample upon electron bombardment.

The Auger effect is a process by which electrons with specific energies are ejected from atoms in response to a downward transition by another electron in the atom. In Auger electron spectroscopy, the vacancy is produced by bombardment with high energy electrons, but the Auger effect can occur if the vacancy is produced by other interactions. It was discovered by Lise Meitner and Pierre Auger independently as one of the methods of electron rearrangement after electron capture into the nucleus[187].

If an inner shell electron is removed from an atom, an electron from a higher level will quickly make the transition downward to fill the vacancy. Sometimes this transition will be accompanied by an emitted photon whose quantum energy matches the energy gap between the upper and lower level. Since for heavy atoms this quantum energy will be in the x-ray region, it is commonly called x-ray fluorescence. This emission process for lighter atoms and outer electrons gives rise to line spectra.

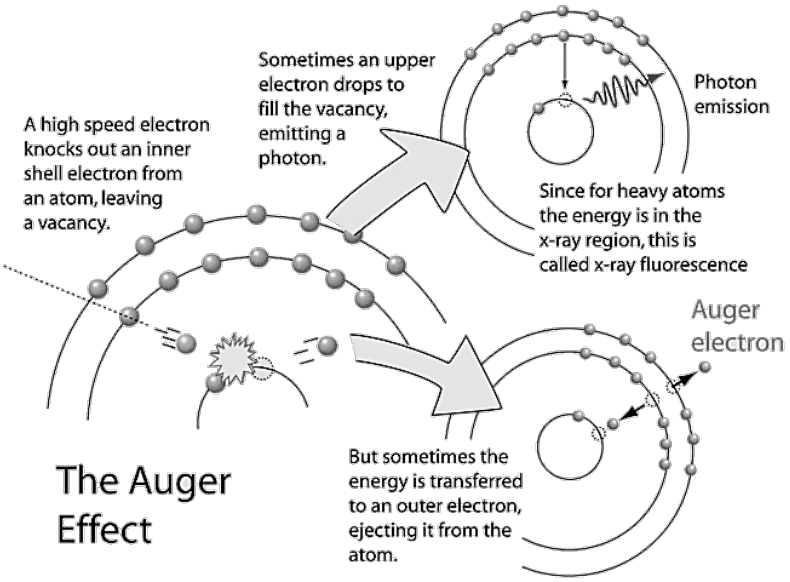

Figure 2-8.Graphical illustration of the Auger effect, image from HyperPhysics site [188].

In other cases, the energy released by the downward transition is given to one of the outer electrons instead of to a photon, and this electron is then ejected from the atom with an energy equal to the energy lost by the electron which made the downward transition minus the binding energy of the electron that is ejected from the atom. Though more involved in interpretation than optical spectra, the analysis of the energy spectrum of these emitted electrons does give information about the atomic energy levels. The Auger effect bears some resemblance to internal conversion of the nucleus, which also ejects an electron. Graphical illustration of the Auger effect is shown in **Figure2-8**.

In the latter case, the kinetic energy of the Auger electron is given by equation:

$$\boldsymbol{E_k = E_{core} - E_{1st-outer} - E_{2nd-outer}}$$

Where E_{core} is the bonding energy of the electron removed from the core shell, $E_{1st-outer}$ is the energy of the electron which fills the hole and $E_{2nd-outer}$ is the bonding energy of the emitted Auger electron. The energies of the Auger electrons are in the range of 50 to 3keV and are characteristic for atoms of a specific element due to unique orbital energies. This allows spectroscopic investigation of the material which is in the basis of the AES. UHV conditions are necessary in order to avoid scattering of the electrons by the gas phase molecules and to be prevented by their adsorption on the sample's surface. That is why, similarly to LEED, AES became popular in 1960s with a development of vacuum surface science.

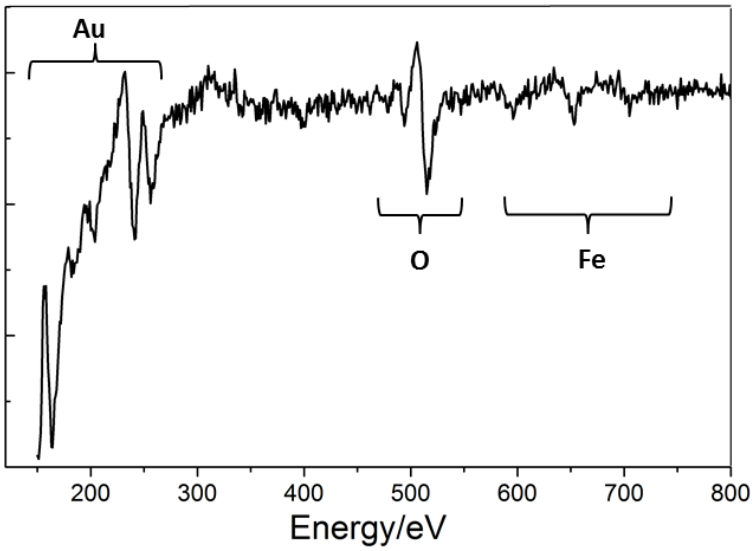

Figure 2-9. A typical AES spectrum of an FeO film on Au(111).

To measure Auger spectra, the same four-grid optics as in LEED is used, as shown in **Figure2-7a**. The electron gun is placed in front of the sample and current is applied to the filament. Emitted electrons hit the sample initiating the Auger process. A set of grids with a retarding potential allows only the Auger electrons with a given energy to pass to the detector. The potential (energy) increases in steps, which allows collecting all the electrons with energies in a given range. The multiplier strengthens the signal which is then recorded by a computer in a form of energy vs. Auger electron intensity plot (derivative). The energies of the Auger electrons emitted from different elements are unique so the chemical composition of the surface can be determined from the acquired spectrum. The technique is surface sensitive due to low energy of the electrons as introduced in (short mean free path). A typical AES curve of ultra-thin layer FeO grown on Au(111) is shown in **Figure2-9**, the fingerprint peaks of Au, O and Fe are highlighted.

2.2.4. Temperature Programmed Desorption (TPD)

Temperature Programmed Desorption (TPD), also called Thermal Desorption Spectroscopy (TDS), is an experimental technique based on mass spectrometry that allows analysis of atoms and molecules which desorb from the surface upon linear temperature increase. It provides qualitative and quantitative information on the adsorbats, such as their atomic masses, bonding energies and the amount. To some extent, the technique also allows the analysis of chemical composition of the thin films and coatings, by measuring the masses during thermal decomposition.

Mass Spectrometry

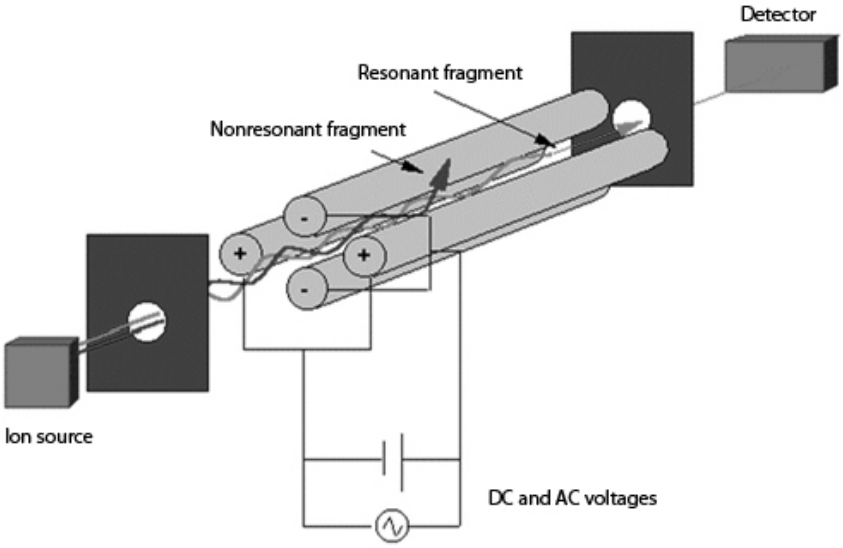

Figure 2-10.A schematic drawing of Quadrupole Mass Spectrometer. Image from Chemical Instrumentation Facility of Iowa State University[189]

Every atom has an atomic mass which is given in atomic mass units (amu). Similarly, every molecule has an atomic mass which is the sum of the atomic masses of atoms which form the molecule. The instrument which is able to detect the atomic masses of gas phase / vaporized atoms and molecules is called Mass Spectrometer (J. J. Thompson, 1911). The working principle is based on the ionization of atoms by electrons emitted from the cathode in the ionizer, separation of ions by mass-to-charge (m/e) ratio in electric and magnetic fields and detection of ions in the detector. The signal is recorded by a computer in the form of intensity vs. mass-to-charge ratio spectrum. The analysis provides qualitative (chemical composition), as well as quantitative (amount of a given chemical compound, ratio between different compounds) information. There are different types of Mass Spectrometers. One of the most commonly used is the Quadrupole Mass Spectrometer (QMS), where the ion separation system consists of four parallel metal rods. The rods are connected in pairs and voltages (+) and (-) are applied to these pairs. Because of the applied voltages, an electric field is formed between the rods and, depending on the voltages, only ions with certain mass-to-charge ratio will be able to pass the rods and reach the detector. A schematic drawing of Quadrupole Mass Spectrometer is given in **Figure2-10.**

Adsorption / desorption processes and TPD analysis

Atoms and molecules can adsorb on the surface from the gas phase when attractive forces exist at a short distance between them. There are two principle modes of adsorption on surfaces: physisorption and chemisorption. The basis of distinction is the nature of the bonding between adsorbates and surfaces. Generally, physisorption is caused by weak van der Waals interaction and chemisorption occurs when chemical bonds are formed. The molecule can adsorb on the surface directly (first-order process)

or the adsorption can be accompanied by molecule's dissociation (second-order). Adsorption strength is represented as adsorption energy (E_a) and it can be measured by the reverse process, namely, desorption, which is defined as the release of adsorbates from the solid surface induced by heating or any other energy injection process. Because the interaction depends both on the nature of the adsorbate and the surface, different adsorbates desorb from different surfaces at different temperatures. In addition, the position within the substrate where the molecule adsorbs (terrace, step edge, defect, etc.) plays an important role.

The energy necessary to desorb the molecule is called the activation energy of desorption E_d and equals the energy of adsorption (or adsorption + dissociation in). Again, a molecule can desorb from the surface directly (first-order process), or two atoms or molecules from neighboring sites may form a molecule and desorb together (second-order).

The energetics and kinetics of adsorption is obtained by analyzing the desorption rate up on heating, defined as the number of molecules desorbing in time, is given by the Polanyi-Wigner equation[190]:

$$\mathbf{r} = -\frac{d\theta}{dt} = v\theta^n e^{\frac{-E_d}{RT}}$$

Where R is the gas constant, T is the temperature, t is the time and θ is the coverage ($0 \leqslant \theta \leqslant 1$) and υ is the pre-exponential Arrhenius factor. Qualitative data analysis is performed on the basis of the so called Redhead formalism[190]. In TPD experiment, the temperature of the sample has to be linearly increased in time. For a constant heating rate the temperature of the sample during heating is given by equation:

$$\mathbf{T} = T_0 + \beta t$$

Where T_0 is the starting temperature and β is the heating rate. With these assumptions, the Polanyi-Wigner equation will have the form:

$$\mathbf{r} = -\frac{d\theta}{dt} = \frac{v}{\beta}\theta^n e^{\frac{-E_d}{RT}}$$

Initially the increasing of the temperature results in an exponential rise of the desorption rate. At the same time coverage of the surface decreases. Three different desorption systems, corresponding to zero-, first-, and second-order kinetics, are shown in **Figure 2-11**. Zero-order desorption is the case that the desorption rate is independent of the coverage ($\theta = 0$). The TPD curves show the same leading edge, and the peak maximum shifts to higher temperature with increasing coverage. For the first order desorption, peaks are asymmetric, but the peak maximum is independent of the initial coverage. Second order desorption process is observed in many dissociative adsorption reactions. The peak positions shift with increasing coverages to lower temperatures, and the peak is symmetric.

Simplified analyses can be established based on the peak maximum temperature observed in a thermal desorption spectrum, which is so-call Redhead's analysis [190], The maximum in the desorption rate occurs when

$$\frac{\mathrm{d}r_{max}}{\mathrm{dt}} = 0$$

In the case of first order desorption (n=1), The relation between E_d and T_{max} can be shown as:

$$\boldsymbol{E_d = RT_{max}\left[ln\frac{\nu T_{max}}{\beta} - 3.64\right]}$$

Calculation of activation energy using this method is generally valid for first-order desorption. A reliable pre-exponential frequency factor ν is typically set to 10^{13} s^{-1}

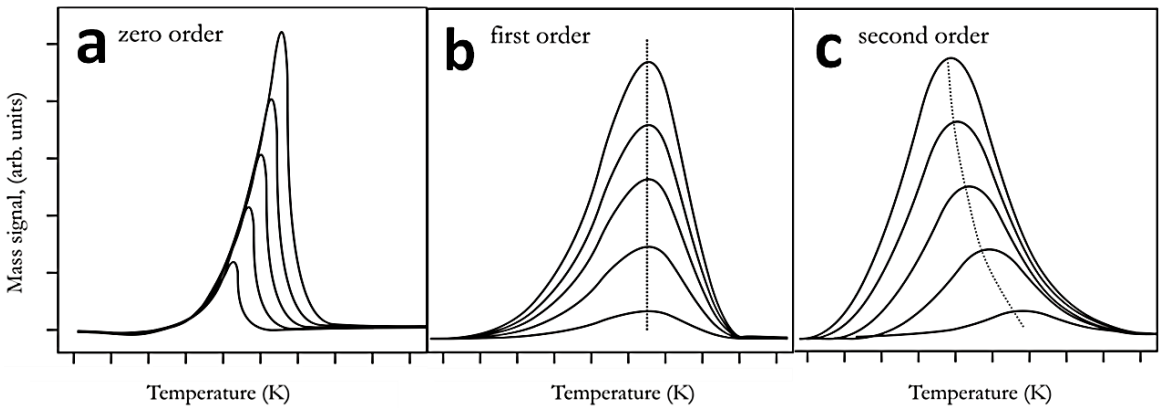

Figure 2-11. Typical sets of zero- (a), first- (b) and second-order desorption (c) curves for different initial coverages.

In a typical TPD experiment, the sample is positioned in front of a differentially pumped QMS and heated with a constant heating rate (typically of 1-5 K/s). At certain temperatures certain adsobates desorb to the gas phase. The desorbing species are monitored by QMS. The computer records the spectrum of a given atomic mass as a function of sample's temperature. Several different masses can be monitored simultaneously. In case of probe molecule desorption studies, the sample is positioned in front of the directional gas doser and exposed to the probe gas before positioning in front of the MS. A typical TPD spectrum of CO adsorbed on Pt(001) and Pt(111) is shown in **Figure2-12**.

Each peak on TPD curve corresponds to various desorbing species. The area under a peak is proportional to the amount of adsorbed species. The position of the peak (the peak temperature) is related to the enthalpy of adsorption. TPD provides information on the strength of the bond between adsorbate and substrate.

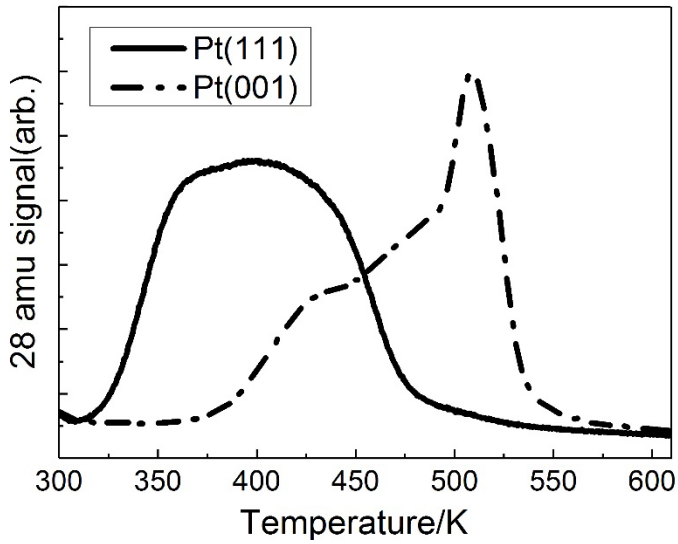

Figure 2-12. TPD spectra of CO adsorbed on Pt(001) and Pt(111). The heating rate is 2K/s

Chapter 3.
Strong metal-support interaction of Pt and Pd on Fe_3O_4(001)

3.3. Introduction

As introduced in **Section 1.1**, the strong metal-support interaction (SMSI) is mostly discussed in terms of the encapsulation of the metal by the oxide layer. In this context, the encapsulation process can intimately be related to the surface structure of oxide support. Indeed, the interaction depends primarily on the adhesion energy between the metal and the oxide, which is envisioned to depend on the interface structure.

Nucleation, growth and thermal stability of Au[191-192], Pd[193], Pt[20, 25, 192] supported on Fe_3O_4(111) thin films have been studied in detail during past years. It was shown that all above mentioned metals form hemispherical nanoparticles that expose (111) top facets. No indication of SMSI between the support and Au was reported. For Pd, an interface oxide layer forms between the particles and the oxide support upon oxidation at 500-550K[193]. Studies at the higher temperatures have not been performed yet. Pt was found to exhibit the typical SMSI effect through encapsulation by a monolayer FeO(111) film[20, 25, 192].

In this Chapter, we show results of preparation of the flat Fe_3O_4(001) thin film on Pt(001) with the thickness of several nanometers. Then we addressed the nucleation, growth, and thermal stability of Pt particles on the film and compare the results with those obtained previously in our laboratories for the Pt/Fe_3O_4(111) system in order to elucidate the surface structure effect to the SMSI. In addition, we also studied the case of Pd and compare it with Pt to demonstrate the metal effect to SMSI.

3.4. Preparation of the Fe_3O_4(001) films[1]

Following epitaxial relationships between Pt and Fe_3O_4 [192, 194], we made use of Pt(001) as a support to grow (001) films. The thin Fe_3O_4(001) film was prepared on Pt(001) single crystal. Pt(001) single crystal was cleaned by repeated Ar^+ ions sputtering and vacuum annealing cycles. The sputtering was performed with energy of 1keV and the sputtering current of 22.5 μA for 1 hour at 530K. After sputtering the

[1] This part of the work was done together with Earl Davis, a PhD student in the group

sample was annealed at 1200 K for 3 min in UHV. In this way, extended flat Pt(001) terraces were obtained in STM images (**Figure 3-1b)** and the characteristic "hex"-reconstruction was observed in LEED (**Figure 3-1a)**. In addition, the crystal was oxidized at 900 K in 1 x 10^{-6} mbar oxygen between sputtering cycles to remove traces of carbon and subsequently flashed to 1000-1100 K. Some precautions had also to be taken to remove iron species which may diffuse into the crystal after preparation of numerous thin film samples [195]. The cleanness of the crystal was checked by AES and STM with no residual carbon species contamination on the surface. (**Figure 3-1c**)

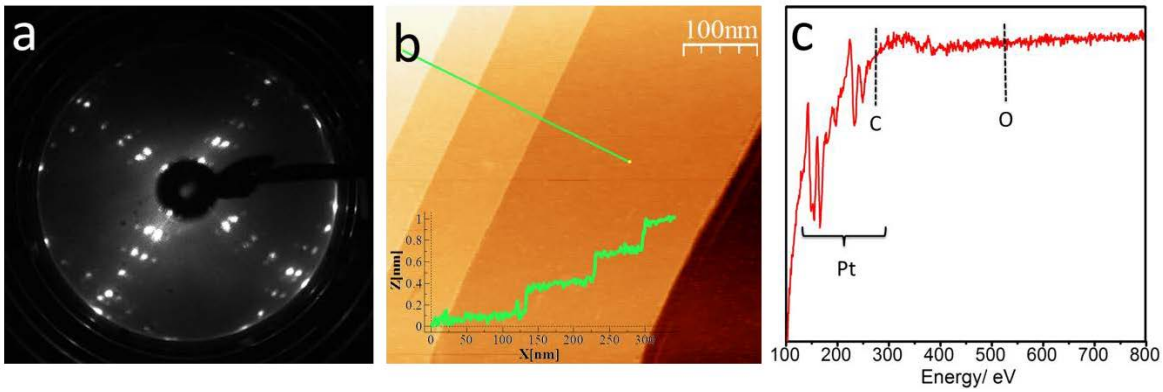

Figure 3-1. Clean Pt(001)-hex reconstructed surface: (a)LEED pattern (at energy 50ev); (b) STM image with profile line showing monatomic steps of 0.2nm(Tunneling conditions: bias −1.9 V, current -0.3 nA); (c) Auger spectra by energy 1keV, the peak(s) position of Pt, C(at 273eV), O(at 505eV) are indicated.

The Fe_3O_4(001) film was grown on a Pt(001) substrate as follow: Prior to deposition, the crystal was flashed to 600K to desorb adsorbates. Firstly, an iron buffer layer was deposited onto the clean Pt(001) surface in UHV, which leads to lifting of the Pt(001) "hex"-reconstruction, the remaining (1×1) diffraction spots **(Figure 3-2a)** could be assigned to the epitaxial grown Fe(001) layer, as it has only a small mismatch with Pt(001). According to the present literature, initial growth of Fe on Pt(001) is fcc, with a transformation to bcc structure as the Fe layer grows to a thickness of 0.8-2.2nm[196-197]. General morphology as shown by STM images **(Figure 3-2d, g)** keeps unchanged compared with Pt(001) except some roughening, and the monoatomic steps still can be seen. Iron protrusions on the surface are 1-2ML in height and occasionally manifest as big particles.

Subsequent reactive deposition of 3nm iron at 300 K in 5×10^{-6} mbar of O_2 resulted in a diffused diffraction LEED pattern **(Figure 3-2b)**, however, STM images **(Figure 3-2e, h)** revealed the appearance of irregular rectangular monolayer oxide island on terraces and continuous belt attached to step edges. This indicates the epitaxial growth of oxide layer on the Pt(001) substrate. In addition, there are many ad-species on the surface which can be assigned to hydroxyl groups formed by the reaction with residual gases in our ultra-high vacuum chamber. After the final annealing at 1000K in UHV for 10min, LEED pattern transformed into the one

well-documented for a $Fe_3O_4(001)$-$(\sqrt{2} \times \sqrt{2})R45^o$ [164, 169, 198-199] reconstructed surface **(Figure 3-2c)**. STM images revealed wide terraces with few screw dislocations. The terraces show atomic rows in the [110] direction and anti-phase domain boundaries, all typical of the B termination. [143, 180] High-resolution images also revealed the reduced existence of residual hydroxyls on surface, some of which aggregated at the grain boundaries as indicated in image. In addition, the depressions could tentatively be attributed to Fe vacancies in the topmost layer. **(Figure 3-2i)**

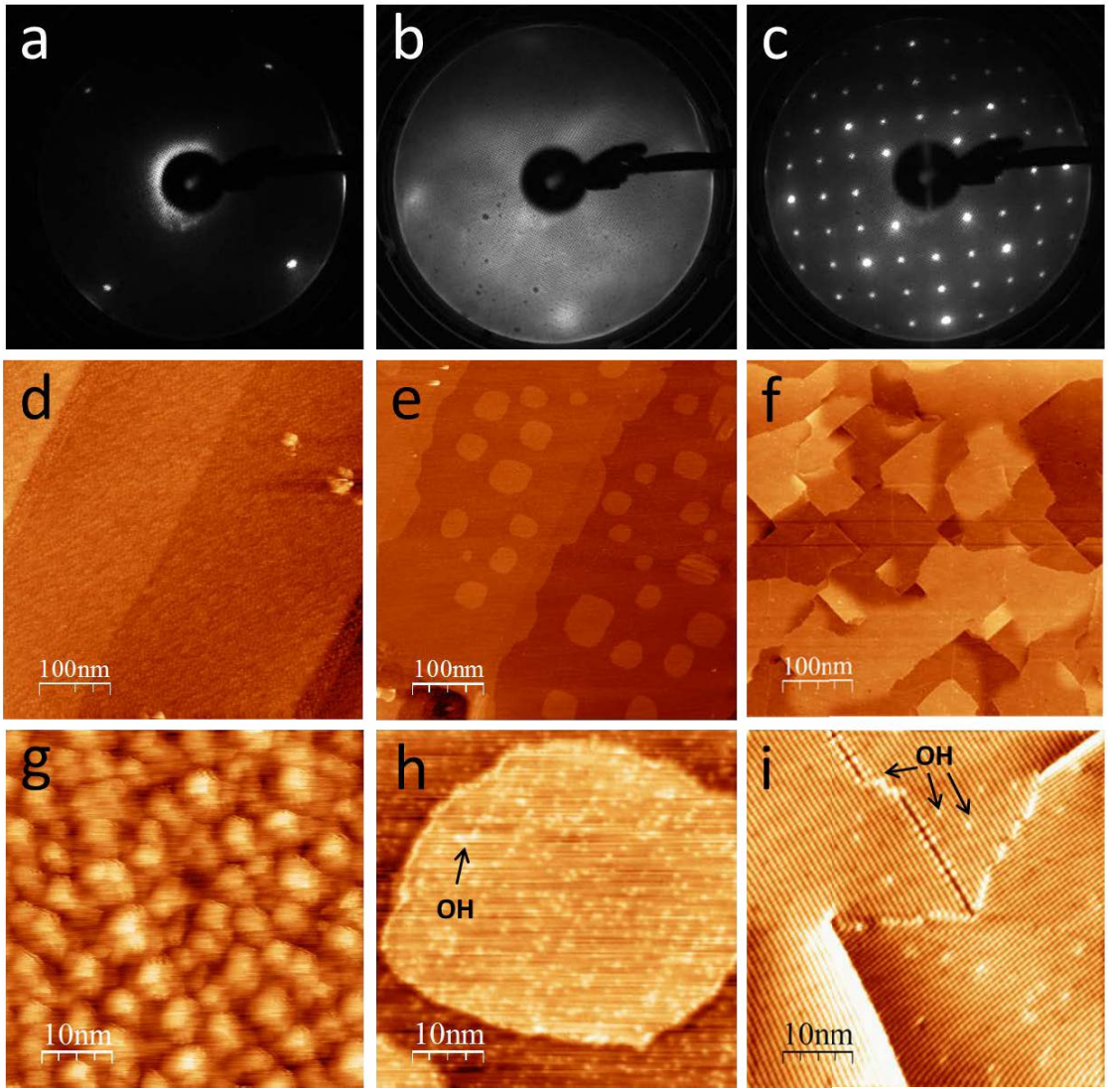

Figure 3-2. LEED patterns and STM images of the $Fe_3O_4(001)$ preparation steps on Pt(001). (a, d, g) Fe buffer layer was deposited; (b, e, h) after Fe reactive deposition in $5x10^{-6}$mbar oxygen ambient at 300 K; (c, f, i) after final annealing in UHV at 1000K for 10min. Tunneling conditions (bias and current): (d,g) −3 V, 0.26 nA; e, f) -2.5 V, 0.25 nA; (f, i) 1.5 V, 4 nA; LEED energy: (a) 50 eV; (b,c) 95eV

The preparation was fully reproducible. Note that in this recipe, the following factors are of particular importance: Firstly, as the existence of Fe buffer layer plays a key role, sample temperature during iron reactive deposition should be relatively low

(RT in this case), otherwise the metallic Fe layer can, at least partly, be oxidized. Reactive deposition at 550 K on top of the 3 nm-thick buffer layer led to the mixture of (001) and (111) surfaces. Secondly, increased oxygen pressure (in the range of 10^{-5} mbar) sometimes caused formation of small areas characteristic of FeO(111)/Pt(001) as judged by LEED. STM inspection of such samples showed deep depressed areas in the film like holes, showing STM images characteristic of FeO(111)-(2x10)[200] on Pt(001) structure.

3.5. Nucleation and growth of Pt on Fe_3O_4(001)

Pt was deposited onto Fe_3O_4(001) at RT. Note that a retarding potential was applied to the samples during depositions using electron beam assisted evaporators (Focus EMT3). The samples were annealed to different temperatures and characterized by LEED, AES and STM. The deposition rate of Pt, as well as the height of monatomic Pt layer, were calibrated by Pt deposition onto a clean Pt(001) single crystal and following analysis of STM images. Pt formed 1 ML thick islands on Pt(001) single crystal which makes an accurate calibration possible.

CO TPD experiments were performed by exposing the samples to CO using a directional gas doser placed in a distance of ~1 mm to the sample and subsequent heating in front of the QMS having a cone which is positioned ~ 0.5 mm away from the sample to minimize parasitic signals from the sample holder. The heating rate was 2 K/s.

We studied adsorption, nucleation and growth of Pt on Fe_3O_4(001). Samples with 0.15, 0.7, 1.0, 1.5 ML Pt were selected for this study after room temperature deposition. The STM images are displayed in **Figure 3-3.**

At the lowest Pt coverage of 0.15 ML **(Figure 3-3(b)**, three different kinds of protrusions are observed as indicated. The first kind protrusions sit on top of the iron rows and can be assigned to hydroxyls as seen on the clean Fe_3O_4(001) **(Figure 3-2 i, 3-3a)**. Accounting for the majority, the second kind protrusions were ~3 Å in height (**Figure 3-2 a**), which is quite similar to the atomic diameter of Pt of 3.54 Å. Most of this kind protrusion locate between the Fe rows and can be assigned to single Pt atoms. Registry analysis in **Figure 3-3 c** reveals that the Pt atoms occupy the so-called "narrow" sites on the $(\sqrt{2} \times \sqrt{2})R45^{o}$-reconstructed Fe_3O_4(001) surface as indicated on the clean Fe_3O_4(001) **(Figure 3-3 b)** which is in the same manner for Pd[201], Au[171], and Ag[202] adsorbed on Fe_3O_4(001).

The third kind protrusions of 6-9 Å in height and 15-20 Å in lateral size are quite rare, which can be assigned to Pt clusters. The Pt adatoms and clusters are distributed randomly on the entire oxide surface and show no preferential anchoring on step edges and screw dislocations in large scale images (not shown here). Majority existence as single atom for Pt implies the relatively strong interaction of the Pt atoms with the $(\sqrt{2} \times \sqrt{2})R45^{o}$ Fe_3O_4(001) surface that results in limited surface diffusion

that, in turn, prevents Pt agglomeration into the larger clusters. The rare formation of Pt clusters in our experiments may also result from the adsorption of residual gases (such as CO) as previously reported for Pd adatoms.[201]

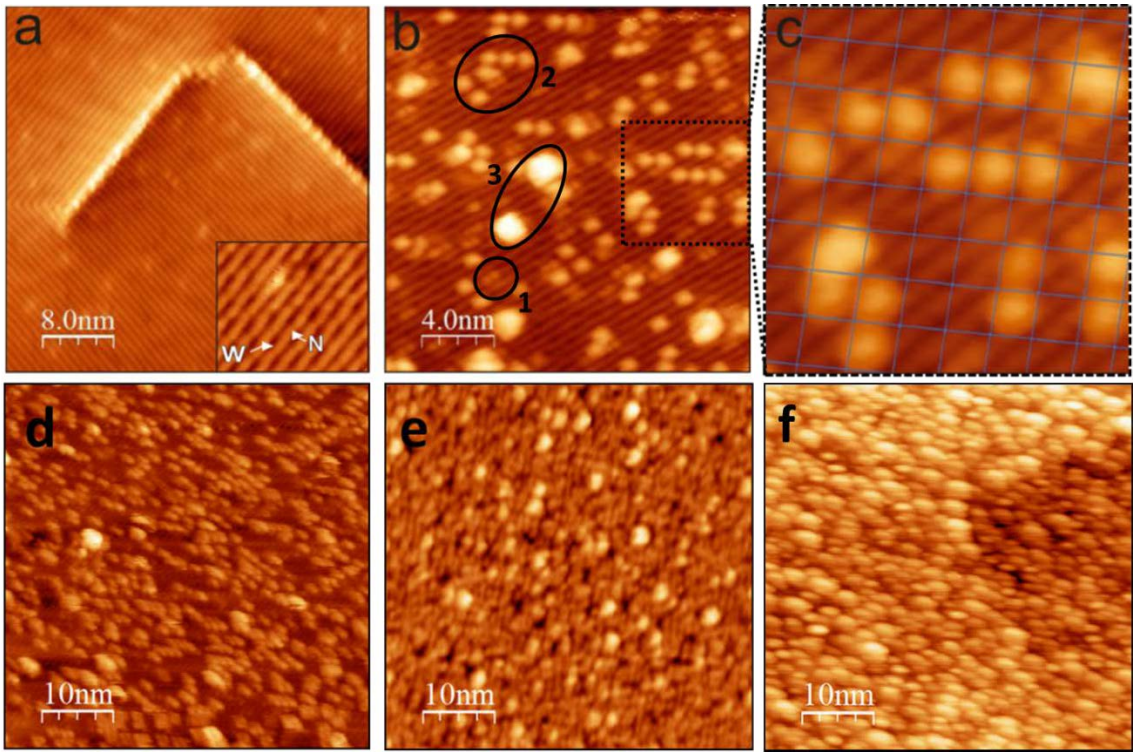

Figure 3-3. STM images of (a) a clean Fe_3O_4(001) film, wide (W) and narrow (N) adsorption sites within the $(\sqrt{2} \times \sqrt{2})$R45°-$Fe_3O_4$(001) unit cell are indicated; (b) 0.15ML Pt; (c) zoom-in of the selected region of b; d-f) 0.7, 1.0, 1.5 ML Pt at 300 K. In panel c, the grid lines join the wide sites, therefore, the Pt adatoms occupy the narrow sites. (Tunneling conditions: (a) bias −1 V, current 0.5 nA; (b) −1 V, 0.7 nA; (d,e) −1.5 V, 1 nA; (f) −2V, 0.4 nA).

Basically, such a nucleation-and-growth mode remains at increasing Pt coverage up to 1 ML, upon which the surfaces are mostly covered by Pt adatoms **(Figure 3-3d,e)**. Similar behavior was reported previously for Ag adatoms on Fe_3O_4(001).[202] A considerably higher density of Pt clusters observed here for Pt compared to Ag may be explained by the stronger interaction of Pt adatoms with residual gas molecules (CO), which, in turn, weakens the Pt bonds to the support and facilitates the diffusion of Pt to form aggregates[201]. Indeed, Au adatoms, as presumably more weakly bound species, showed sintering at considerably lower coverages.[171] Further coverage increase to 1.5 ML triggers three dimensional growth mode, and large Pt particle appears **(Figure 3-3f)**.

3.6. Thermal stability of Pt/Fe_3O_4(001): Encapsulation

Two-dimensional growth of Pt on Fe_3O_4(001) indicates high adhesion energy between the metal and the support. However, because this finding was observed on the "as deposited" samples at room temperature, we need to see what extent this

adhesion can resist the thermal activation which change the particles' size and shape. To examine thermal stability, the samples were annealed stepwise to 500, 700, 850 and 1000 K for 10 min each.

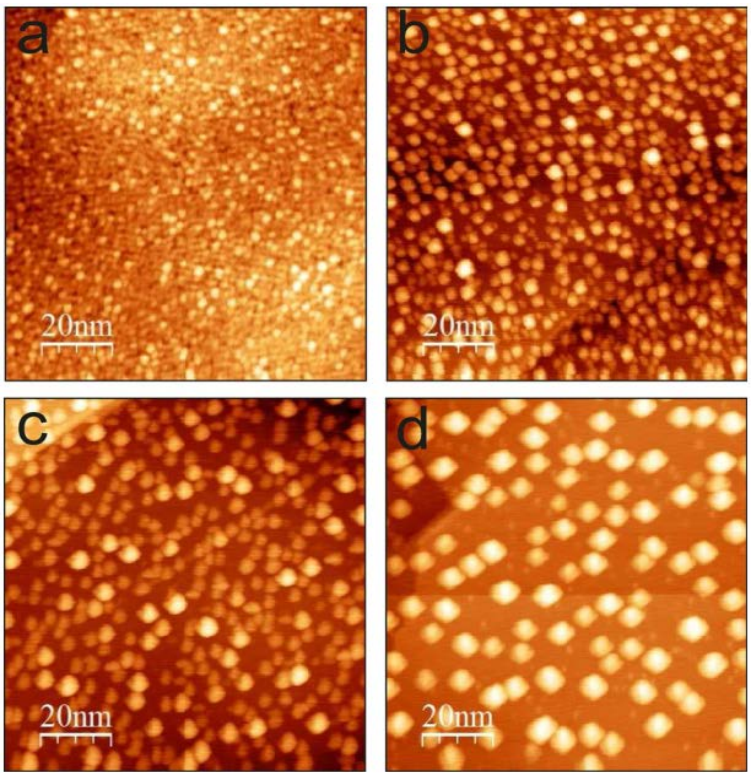

Figure 3-4. STM images of 1 ML Pt/Fe_3O_4(001) annealed stepwise at (a) 500 K, (b) 700 K, (c) 850 K, and (d) 1000 K. (Tunneling conditions: (a, b)bias −2 V, current 0.7 nA; (c, d) −2 V, 1 nA).

A series of STM images obtained for 1 ML Pt/Fe_3O_4(001) are shown in **Figure 3-4**. Compared to the "as-deposited" sample **(Figure 3-3e)**, UHV annealing at 500 K for 10 min does not cause considerable morphological changes **(Figure 3-4a)**, except the density of clusters increases a little bit. Metal sintering becomes substantial after annealing at 700 K **(Figure 3-4b)**. The Pt nanoparticles can clearly be recognized and they grow both laterally and in height at the expense of monoatomic species. Further sintering, presumably by Ostwald ripening, proceeds upon heating to 850 K **(Figure 3-4c)**. Ultimately, after annealing at 1000 K, Pt nanoparticles with a cuboid shape dominate the surface **(Figure 3-4d)**.

Only small morphology change upon 500K UHV annealing indicates that the metal-support interaction is strong enough to pertain two-dimensional metal configuration to 500K at least. STM images for comparison in different coverages after 700K annealing are presented in **Figure 3-5.** Profile lines show selected particles' heights. For the lowest studied coverage of 0.15 ML**(Figure 3-5a)**, clusters of 2 layers in height are dominant and the lateral size does not increase in obvious. This is the indication of the three-dimensional growth mode. At the coverage of 0.7 ML **(Figure 3-5b)**, the particles with 3 layers' height appear and the maximum height of particles

grows further to 6 layers at the coverages of 1 and 1.5ML **(Figure 3-5c,d)**. The particles exhibit round like shapes with some preferential orientation of the edges. As we have seen in **Figure 3-4,** reshaping of the particles are finished after final 1000K annealing and the details of the cuboid shape particles are presented following.

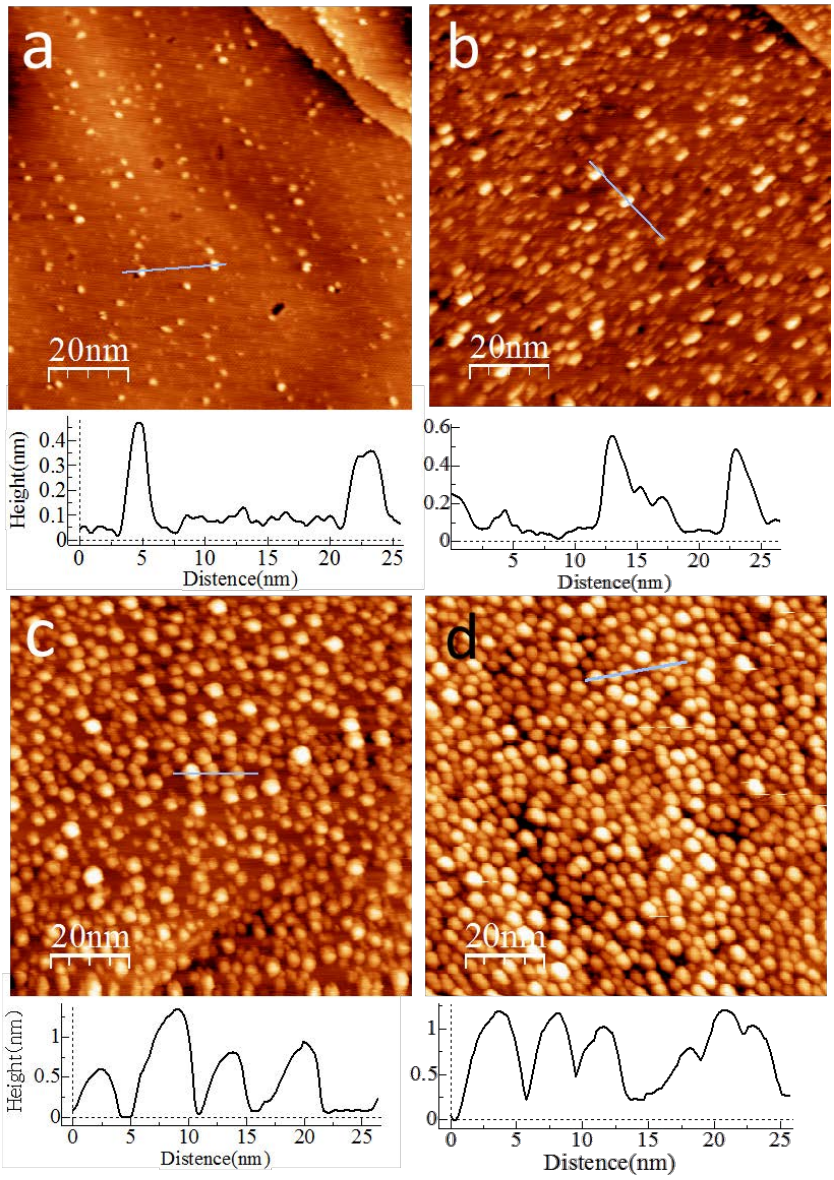

Figure 3-5. STM images of Pt / Fe_3O_4(001) at different coverages annealed at 700 K for 10 min: (a) 0.15 ML, ((b) 0.7 ML, (c) 1.0 ML and (d) 1.5 ML; profile lines show particles height; (Tunneling conditions: (a)bias −1 V, current 0.5 nA; (b) −2 V, 0.7 nA; (c) −2 V, 0.5 nA ; (d) -1.0 V, 0.4 nA)

Similar annealing experiments performed on 4 ML Pt sample reveal essentially the same behavior for annealing at around 700 K (not shown here). However, the roundish shape is not the final state. For comparison, the morphologies of high-coverage samples annealed to 1000 K are shown in **Figure 3-6.** Again, all annealed particles ultimately showed the cuboid shape. The annealing time needed to reach such a shape is relatively long, that is, around 30 min. The annealing of 1.5 ML

Pt sample for 10 min resulted in a mixture of hexagonal and rectangular top facets (**Figure 3-6 b**). The latter dominate the surface only after further annealing for 30 min (**Figure 3-6 c**). For the highest Pt coverage studied here(4 ML), some template effects can be seen in the image shown in **Figure 3-6 d**, as the cuboid Pt particles form quasi ordered arrays along the crystallographic directions of the support. Interestingly, with increasing Pt coverage, the lateral size of the annealed particles, on average, remains the same, and only the particle density and heights increase (we will try to rationalize this finding below).

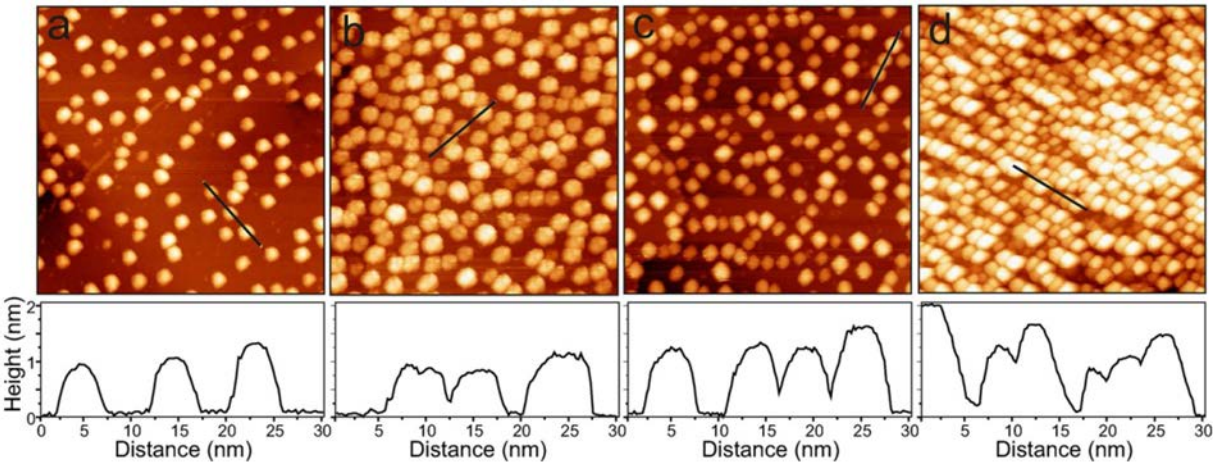

Figure 3-6. STM images and corresponding profile lines of the Pt/Fe_3O_4(001)samples, all annealed at 1000 K. (a) Pt coverage is 1ML, and the annealing time is 30 min; (b)1.5 ML, 10 min; (c)1.5 ML, 40 min; (d)4ML, 30 min. All image sizes are 100 nm x 100 nm. (Tunneling conditions: (a) Bias -2V, current 1nA; (b–d) -1.5 V, 1nA.)

The high-resolution STM image in **Figure 3-7a** reveals that the edges of the Pt particles are oriented along the Fe rows on the surrounding ($\sqrt{2} \times \sqrt{2}$)R45°-reconstructed surface of Fe_3O_4(001). Solely based on these STM images, one can envision that Pt grows in the (001) orientation parallel to the (001) plane of Fe_3O_4, similar to the epitaxial relationships reported in Ref.[194], although these were observed on 2-5 nm thick Pt films grown on Fe_3O_4(001) at high temperatures. Our previous LEED results for the growth of Fe_3O_4(001) films on a Pt(001) substrate showed that lattice vectors of Pt(001) are oriented along the lattice vectors of Fe_3O_4(001)-($\sqrt{2} \times \sqrt{2}$). It is, therefore, plausible that the same mutual orientation holds true for the inverse interface, that is, Pt on an Fe_3O_4(001) substrate. This suggests that the atomic rows on Pt(001) facets run along the Fe rows on the ($\sqrt{2} \times \sqrt{2}$)R45°-reconstructed Fe_3O_4(001) surface.

The 3D view shape of the cluster is shown in **(Figure 3-7b)**. Combined with the contour plot, which shows a 7 layers' particle with truncated top surface **(Figure 3-7a)**, the particle shape can be modeled as truncated square pyramid like. This truncated square pyramid shape could be rationalized by the so-called Wulff construction of the supported metal particle. When the interface energy is lower than

the substrate surface energy, the lower interface energy, the bigger metal-support interface area[203]. A schematic image is given in **Figure 3-7c**.

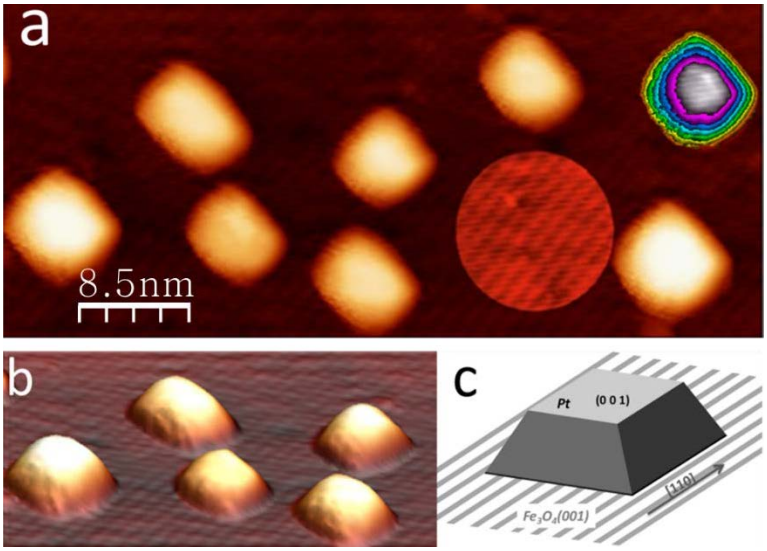

Figure 3-7. (a) STM image of 1 ML Pt/Fe_3O_4(001) annealed at 1000 K. The atomic rows of the support are highlighted in the circle to show the orientation of the particles with respect to the support; top right is the contour plot of the particle at bottom right; (b) 3-dimonsional rendering of (a); (c) Schematic representation of the truncated square pyramid Pt particles. (Tunneling bias −1.5 V, and current 1 nA)

The most straightforward observation of SMSI is the suppression of CO or H_2 uptake. For this, we performed TPD experiments using CO to titrate the Pt surface as the iron oxide support does not adsorb CO at temperatures above 200 K [204]. CO-TPD plots obtained on the 1.5 ML Pt/Fe_3O_4(001) surface annealed stepwise at the specified temperatures are shown in **Figure 3-8a**. Structural characterization after each annealing step was performed by STM and LEED.

The "as-deposited" Pt/Fe_3O_4(001) surface showed a broad desorption signal between 300 and 520 K with a maximum at 450 K, which falls into the range observed for single-crystal Pt surfaces[205]. However, CO-induced sintering of the Pt adatoms, as observed previously for Pd/Fe_3O_4(001)[201], might also affect the first TPD plot. Annealing at 600 K slightly (by≈15 %) reduces the CO uptake, and several desorption features at 360, 420, and 450 K can be resolved. These features remain after annealing at 700 K, which further reduces the CO uptake. The latter decreases to almost zero upon annealing to 850 K, although Pt particles did not show considerable sintering, thus providing direct evidence that the Pt particles exhibit the SMSI effect at elevated temperatures most likely through encapsulation. Indeed, the formation of Pt-Fe alloys as another option to explain the decreased CO uptake would manifest itself as a prominent desorption signal at around 300 K[204], which is not the case here. Ultimately, annealing at 1000 K suppresses CO adsorption totally and it is accompanied by the reshaping of the Pt particles.

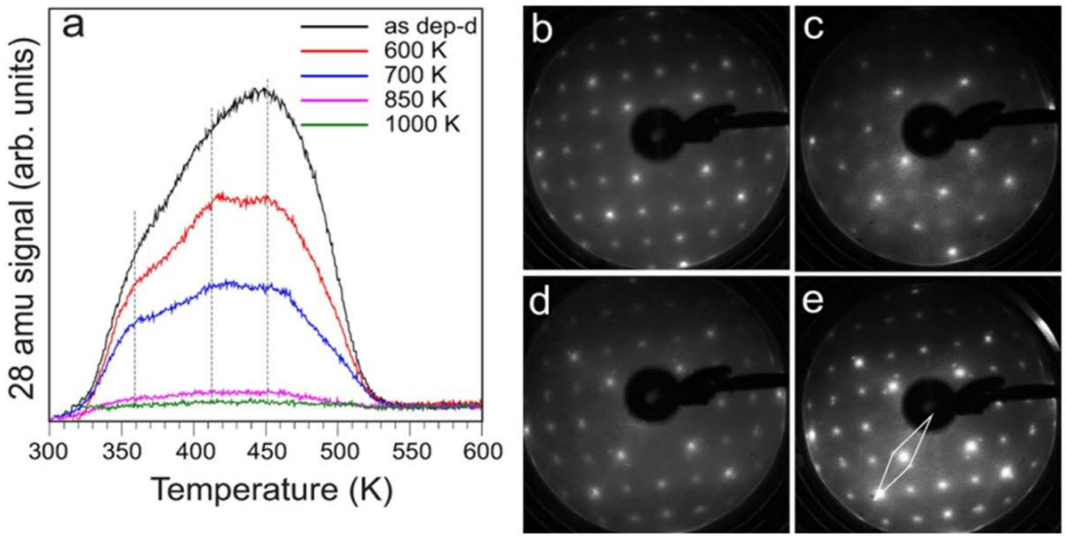

Figure 3-8. (a) TPD spectra of 20 L CO adsorbed at 300 K on 1.5 ML Pt/Fe_3O_4(001) as deposited at 300 K and then UHV-annealed to the indicated temperature. The heating rate is 2 K/s. LEED patterns (at 95 eV) of (b) the pristine ($\sqrt{2}\times\sqrt{2}$)R45°-Fe_3O_4(001) surface, (**c**) after deposition 1.5 ML of Pt at 300 K, and d) after subsequent UHV-annealing to 850 K for 10 min and (**e**) 1000 K for 30 min, respectively. The additional spots are developed, which are assigned to the FeO(111)/Pt(001)-c(2×10) structure as marked in panel **e**.

LEED patterns of the same Pt/Fe_3O_4(001) surfaces recorded before the TPD runs are shown in **Figure 3-8 b-d**. Additional diffraction spots (marked in **Figure 3-8 e**) appear upon annealing that were absent on the pristine Fe_3O_4(001) film annealed at the same temperature (1000 K) before Pt deposition. These spots first develop upon heating to 850 K and become more intense and sharper by annealing at 1000 K. The corresponding surface structure is virtually identical to that observed for an ultrathin iron oxide film grown on a Pt(001) single crystal and assigned to an FeO(111)/Pt(001)-c(2×10) (and/or -(2×9)) coincidence structure[200]). Bearing in mind the cuboid morphology of the annealed Pt nanoparticles, which preferentially expose the top (001) facets, the LEED observation of the FeO(111)/Pt(001) interface can readily be explained by the encapsulation of the Pt particles by an FeO(111) layer. One could argue, however, that the new ordered structure arises from the interface underneath rather than on top of a Pt particle, although the spots seem to be too bright to make the former assignment.

To shed more light on this issue, we performed experiments as follows. The 1.5 ML Pt sample annealed to 1000 K was subjected to a mild Ar^+-ion bombardment (500 eV, 1 μA cm^{-2}, 45° incidence, for 10 s) at room temperature. Certainly, this treatment caused some surface roughening as judged by STM (**Figure 3-9 a**). However, the atomic rows of the ($\sqrt{2}\times\sqrt{2}$) R45°-reconstructed Fe_3O_4(001) between the particles are still visible (**Figure 3-9 c**), thus indicating that ion bombardment under our

conditions does not cause severe sputtering but creates surface defects. However, the FeO(111)/Pt(001) diffraction spots fully disappear (inset in **Figure 3-9 a**). Moreover, CO starts to adsorb on the sputtered surface as observed by TPD (**Figure 3-9 e**), which indicates that the ion sputtering removed the encapsulating layer and exposed the Pt surface.

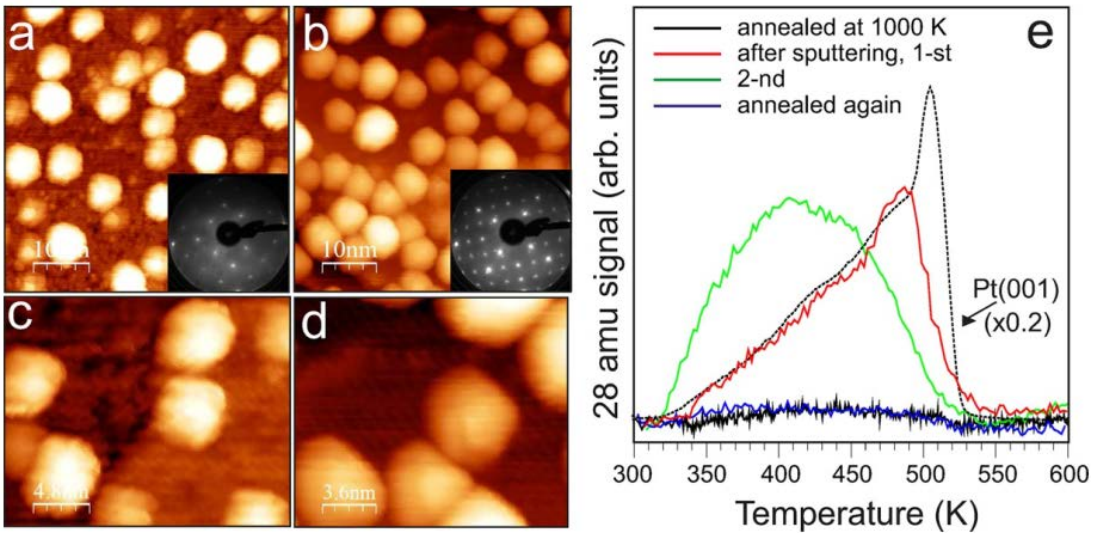

Figure 3-9. (a–d): STM images and corresponding LEED patterns (at 95 eV in insets) of 1.5 ML $Pt/Fe_3O_4(001)$ annealed at 1000 K for 30 min and then (a, c) Ar^+ ion sputtered at 300 K and (b, d) reannealed at 1000 K for 10 min. (Tunneling conditions for all images are bias −1.5 V, and current 1 nA). (e) TPD plot of 20 L CO adsorbed at 300 K on the same samples as indicated. The heating rate is 2 K s^{-1}. The plot of the clean, hex-reconstructed Pt(001) surface, measured before growth of the $Fe_3O_4(001)$ film is shown as a dashed line for comparison.

Interestingly, the first CO-TPD plot revealed a prominent peak at ≈500 K, which shows similarities to the plot measured on the clean hex-Pt(001) surface. It is tempting to assign this feature to the top (001) facets of the Pt particles opened upon ion sputtering of the encapsulated layer. However, such a TPD profile can also be associated with highly stepped Pt surfaces[205] and, more generally, to the low-coordinate Pt atoms formed on the Pt particles upon sputtering of the Pt surface beyond the encapsulating layer. Indeed, the second CO-TPD run already showed a broad signal similar to that measured on "as-prepared" Pt particles (**Figure 3-8 a**). Reannealing of the sample at 1000 K for 10 min, in essence, recovers the initial characteristics of the sample before treatment: the FeO(111)/Pt(001) diffraction spots reappear and the CO uptake decreases back to zero. These presented LEED, STM, and TPD results provide strong evidence that Pt nanoparticles undergo the SMSI effect by encapsulation by an iron oxide layer, which is an FeO(111) monolayer in nature. Unfortunately, atomic resolution of the Pt particles could not be achieved with our microscope (basically, because of their small size), which would otherwise allow us to determine the atomic structure of the Pt top facets more precisely.

3.7. $Pt/Fe_3O_4(001)$ *versus* $Pt/Fe_3O_4(111)$

In order to understand support effect on SMSI, we compare $Pt/Fe_3O_4(001)$ and previously studied $Pt/Fe_3O_4(111)$ systems[20, 22, 25]. On both the (001) and (111) magnetite surfaces, Pt shows no preferential nucleation on defects and appears to be dispersed uniformly across the entire surface. Pt on the $(\sqrt{2} \times \sqrt{2})$ R45°-$Fe_3O_4(001)$ surface adsorbs monoatomically, even at 300 K, and occupies the "narrow" sites. On $Fe_3O_4(111)$, the adsorption sites for Pt could not be determined as STM imaging at low Pt coverages is obscured by the presence of poorly defined adsorbate-like species.[206-207] As DFT predicts the strong adsorption of Pt on $Fe_3O_4(111)$ (i.e. ~2.2 eV on the Fe-terminated surface),[208] one could envision monoatomic Pt adsorption on $Fe_3O_4(111)$ as well. Indeed, STM images of $Pt/Fe_3O_4(111)$ at sub-monolayer coverages revealed a high density of small islands, which are only ~2 Å in height and correspond to a single Pt layer.[25] At increasing coverages, the monolayer islands coalesce and form an extended, irregularly shaped network, and only a few Pt particles two layers in height are observed at 300 K. Therefore, for both $Fe_3O_4(001)$ and (111) surfaces, Pt interacts strongly with magnetite, which leads, in essence, to Pt wetting of the oxide surface at room temperature.

For both systems, high-temperature annealing in UHV causes Pt sintering and the subsequent formation of well-faceted 3 D nanoparticles with their edge at the interface running along the crystallographic direction of the oxide surface. These particles exhibit an octahedral shape on $Fe_3O_4(111)$ but a cuboid shape on $Fe_3O_4(001)$, following the epitaxial relationships between Pt and Fe_3O_4, that is, $Pt(111)[110]//Fe_3O_4(111)[110]$ and $Pt(001)[001]//Fe_3O_4(001)[001]$, and thus resulting in particles that expose Pt(111) and Pt(001) top facets on $Fe_3O_4(111)$ and $Fe_3O_4(001)$, respectively.

A notable difference is, however, that the Pt particles on $Fe_3O_4(111)$ sinter remarkably and form extended Pt islands, when Pt coverage increased from 1.8ML to 4ML. Meanwhile, Pt on $Fe_3O_4(001)$ forms small particles ~5 nm in lateral size, at most, and kept almost constant with Pt coverage increasing from 1.5ML to 4ML. Apparently, this finding may be indicative of the difference in adhesion energy causes by the lattice mismatch at two interfaces. On the other hand, our high-resolution electron microscopy studies of encapsulated $Pt/Fe_3O_4(111)$ particles show Fe enrichment of the interface between a Pt particle and an underlying support that results in more Pt-Fe bonds. As the $Fe_3O_4(001)$ surface is initially terminated both by Fe and O atoms, it may well be that limited lateral growth of the Pt particles on $Fe_3O_4(001)$ along the interface may be linked to the interface structure, but it cannot be addressed with tools employed in the present study.

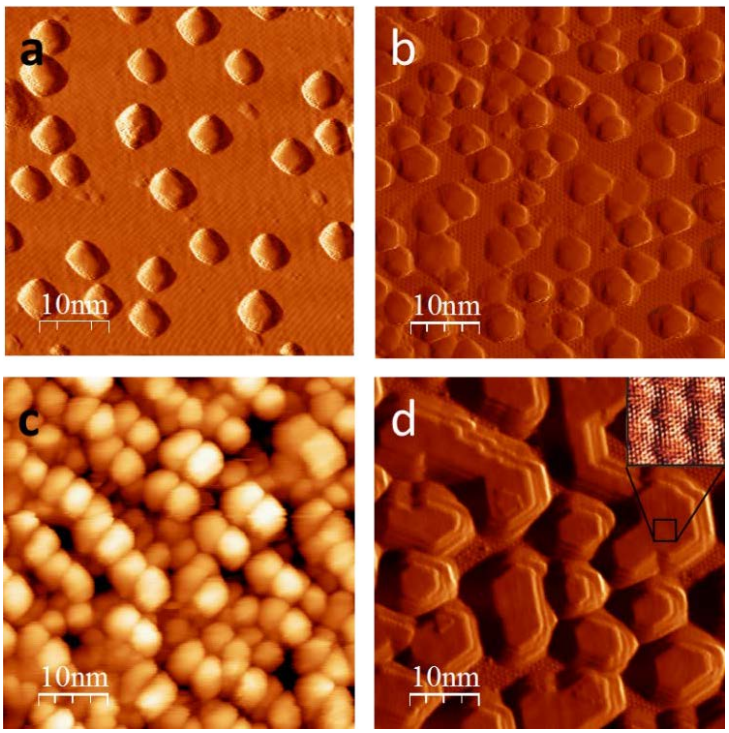

Figure 3-10. STM images of 1.5 ML((a) and (c) 4ML Pt/Fe_3O_4(001) annealed at 1000 K for 30 min; 1.8ML((b) and 4ML(d) Pt/Fe_3O_4(111) at 1000 K for 1 min. (Tunneling conditions: (a, c) -1.5 V, 1nA; (b) 1.4 V, 0.7 nA; (d) 0.5 V, 0.6 n(A). Images (b,d) are provided by Mikołaj Lewandowski, PhD thesis, TU Berlin (2011)

Nonetheless, we may rationalize these results in terms of two processes occurring simultaneously: sintering and encapsulation. Along with the encapsulation, metal decoration with oxide layer would suppress further attachment of metal atoms during Ostwald-type ripening. In addition, metal sintering involves diffusion of the metal ad-atoms which, in turn, depends on the adsorption energy of metal atom on oxide surface. The temperature at which sintering sets in can be estimated from STM images obtained during stepwise annealing. The degree of encapsulation, on the other hand, could be directly estimated by the formation of encapsulating layer on particles' surface, which remains challenging, in particular for Pt particles on Fe_3O_4(001) which are too small to obtain atomic resolution. However, one could use the CO uptake changes as a measure of encapsulation process that after annealing at the encapsulating temperature CO uptake suddenly drops to almost zero. The results are collected in the **Table** below.

	Adsorption energy from DFT (eV)	**Sintering sets in at T (K)**	**Encapsulation temperature (K)**	**Average particle size (nm)**
Pt/Fe_3O_4(001)	-3.89[209]	700	850	~5 (cuboid)
Pt/Fe_3O_4(111)	− 2.24[210]	600	850	~20 (hexagonal)

NOTE: Adsorption energy of Pt on Fe_3O_4(111) is based on the iron-terminated surface; Final

particle size data was taken from the samples of 4 ML Pt on Fe_3O_4 (001) and (111) after UHV annealing at 1000K for 30min and 5min.

As seen from the Table, a higher adsorption energy of Pt on Fe_3O_4(001) of -3.89eV compared with that on Fe_3O_4(111) of -2.24eV is consistent with a higher sintering temperature observed for Pt on Fe_3O_4(001) than on Fe_3O_4(111). Therefore, Pt has more space for growing up on Fe_3O_4(111) than on Fe_3O_4(001), which induces the larger final particle size of Pt on Fe_3O_4(111). Further growth is suppressed by encapsulation which blocks atoms attachment. Also for the same reason, in case the encapsulation happens of Pt on Fe_3O_4(001), Pt particles stop growing and keep final particle size constant as ~5nm when Pt coverage increases from 1 ML to 4ML

3.8. Pd/Fe_3O_4 (001) *versus* Pt/Fe_3O_4(001)

We examined the thermal stability of Pd depsoits on Fe_3O_4(001) films in the same manner as for Pt/Fe_3O_4(001) system. As previously reported by Parkinson's group[201], low coverage deposition of Pd onto the Fe_3O_4(001) surface at room temperature results in single Pd adatoms occupying the preferred "narrow" site in the reconstructed unit cell and 2 dimensional growth similar to the previous observations for Pt. We examined the thermal stability in this system at two higher coverages of 1.5ML and 4ML.

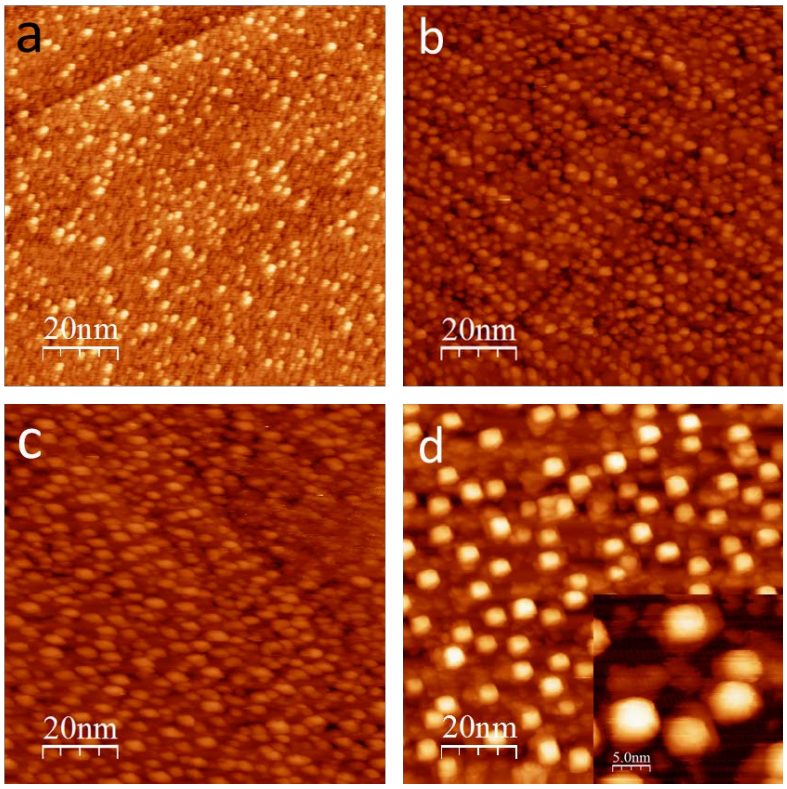

Figure 3-11. STM images of 1.5 ML Pd/Fe_3O_4(001) (a) as deposited, annealed stepwise at (b) 600 K, (c) 700 K, and (d) 850 K, insert as high resolution image. (Tunneling conditions: (a, b) bias −1.5 V, current 0.5 nA; (c, d) −1.5 V, 0.3 nA.

STM images of the samples as deposited and after annealing at Pd coverage of 1.5ML are presented in **Figure 3-11.** For the as deposited sample, majority the oxide surface was covered with 1 ML high particles together with additional particles of 2-3 ML height randomly distributed (**Figure 3-11a)**. Apparently, no preferential Pd nucleation is observed on step edges of Fe_3O_4(001). Annealing at 600K changed the morphology completely (**Figure 3-11b)**. Amount of 3D particles of irregular shape increased and formed quasi-ordered arrays along the crystallographic directions of the support as observed in 4ML Pt on Fe_3O_4(001) after annealing at 1000K in **Figure 3-6d**. Following 700K annealing the particles grow both laterally and in height (**Figure 3-11c**). After further annealing at 850 K, Pd nanoparticles showed cuboid shape with particle size of ~ 4-5nm (**Figure 3-11d**). High-resolution STM image in insert of **Figure 3-11d** reveals that the edges of the Pd particles run along the Fe rows on the surrounding Fe_3O_4(001) $(\sqrt{2} \times \sqrt{2})R45^{o}$-reconstructed surface. Similar to the observation on Pt/ Fe_3O_4(001) in **Figure 3-7**, Pd also grew in the (001) orientation parallel to the (001) plane of Fe_3O_4. Annealing at 1000K resulted in a much less number of Pd particles on oxide surface and showed irregular shape(not shown here), which may be indicative of Pd diffusion into Fe_3O_4 bulk.

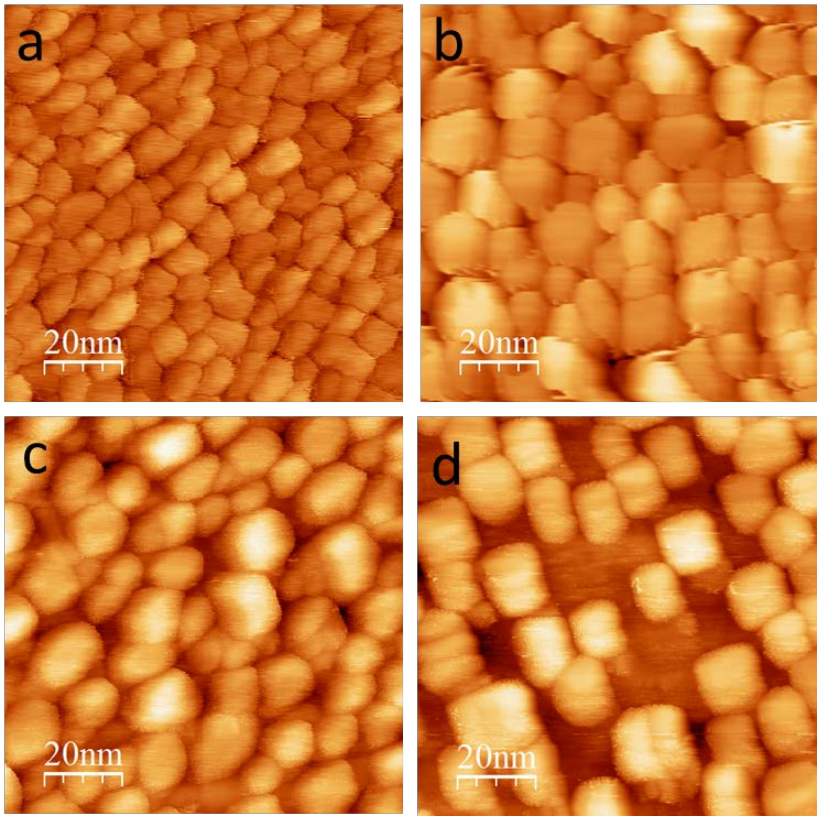

Figure 3-12 . STM images of 4ML Pd/Fe_3O_4(001) (a) as deposited, annealed stepwise at (b) 600 K, (c) 700 K, and (d) 850 K . (Tunneling conditions: (a, b) bias −1.5 V, current 1 nA; (c, d) −1.5 V, 0.5 nA)

When Pd coverage increased to 4ML, Pd exhibited large particles of 7-9 nm immediately after RT deposition on Fe_3O_4(001) as shown in **Figure 3-12a.** This

means that the coalescence of Pd even occurs at room temperature. Compared to the sample of 4ML Pt on Fe_3O_4(001) **(Figure 3-6d)**, bigger particle lateral size of Pd after high temperature annealing (**Figure 3-12c,d**) indicates the lower adsorption energy of Pd on Fe_3O_4(001) than Pt, which is in agreement with the values reported by DFT (Pd: -2.20 eV, Pt: -3.89 eV).[209]

Annealing at 600 K boosted the sintering and the particles grew up to 15-20 nm in lateral size. After further annealing at 700K, it seems that the particles' lateral size stopped increasing, but some particles might grew further. The final 850 K annealing reshaped the particles to cuboid and decreased the small particle's density which may be caused by the Ostwald repining. Edges of the Pd particles are oriented along one direction which has been observed in Pt/Fe_3O_4(001) and 1.5ML Pd on Fe_3O_4(001). Concomitantly, we performed CO adsorption studies by TPD.

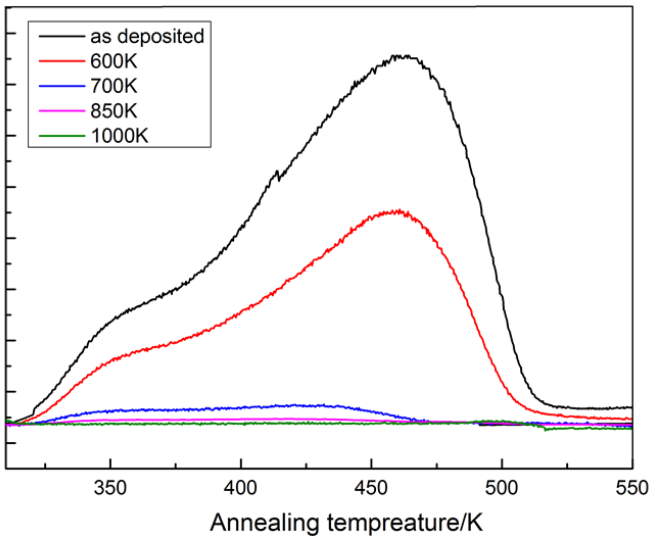

Figure 3-13.TPD spectra of CO adsorbed at 300 K on 4ML Pd/Fe_3O_4(001) during stepwise annealing in UHV. The heating rate is 2 K/s.

On clean Pd particles, CO desorption occurs between 300 and 550 K peaked at ~475 K as shown in **Figure 3-13**. 600 K annealing just deceased the intensity of the CO uptake, but the profile maintains the original shape. However, 700 K annealing suppressed the CO uptake almost to zero which clearly indicates the encapsulation of Pd on Fe_3O_4(001). Simultaneous drop of the CO uptake and stop of Pd lateral size increasing after 700 K UHV annealing, both suggest that these findings are related in the way discussed above for Pt. However, as the Pd sintering on Fe_3O_4(001) occurs at a lower temperature due to a lower binding energy as compared to Pt, the size of Pd particles (~20nm, 4ML, 850 K annealing) is much larger than that of Pt (~5 nm, 4 ML, 1000 K annealing).

Above mentioned qualitive relationship of final particle size and temperature interval between sintering temperature and encapsulating temperature facilitates the controlling of particle size in model system to mimic the real catalyst with

different-size particle. Bigger particles can be obtained by long annealing between sintering temperature and encapsulating temperature; otherwise annealing at temperature higher than encapsulating temperature results in smaller particle.

Chapter 4.
Support effects on structure and reactivity of ultrathin FeO(111) films

4.1. Introduction

Since our group found that an ultra-thin FeO(111) film grown on Pt(111) may show higher CO oxidation rate than the clean Pt(111) surface [21], extensive research have been conducted on FeO(111)/Pt(111) system in many groups worldwide. Both experiment and density functional theory (DFT) calculations showed that[21, 112-114, 153-154, 204, 211], ultra-thin FeO(111) on Pt(111) transforms into an "O rich" FeO_{2-x} structure, which can be described as an O-Fe-O trilayer structure, in pure O_2 or under O_2-rich reaction conditions. This oxygen enrichment is clearly observed in TPD spectra showing additional O desorption peak at lower temperature, which is absent in pristine FeO sample. STM study and DFT calculation suggested that the reaction follows the Mars-van-Krevelen mechanism, that is, the topmost weakly bound oxygen (WBO) atom in the O–Fe–O trilayer reacts with CO and forms CO_2 that desorbs leaving an oxygen vacancy behind, which can be replenished by the reaction with molecular oxygen to end the catalytic cycle. The inverse correlation between reaction rate and oxygen bonding energy suggested the oxygen binding energy as a good descriptor for oxidation reactions over ultrathin oxide films.

In addition, considerable rate enhancement at sub-monolayer oxide coverages suggests the important role of CO adsorption on Pt surrounding FeO_2 islands. The increased residence time of CO on Pt in vicinity to the FeO_2 islands increases the probability to react with weakly bonded oxygen at the islands' edge. This effect has been evidenced by the fact that CO oxidation rate on ZnO(0001) films increased considerably at sub-monolayer coverages when grown on Pt(111), but not on Ag(111). The latter is well known only weakly to adsorb CO. Therefore, CO adsorption on a metal substrate may serve as another descriptor for oxidation reactions over sub-monolayer films.

However, this story has another edition from Prof. Bao and co-workers. Their first paper on this subject in 2010[212] and following study[213] reported a linear relationship obtained between the CO oxidation activity and the perimeter length measured on the 0.25 ML FeO(111)/Pt(111) sample which underwent gradual oxide sintering upon stepwise annealing. The high CO oxidation activity on FeO/Pt(111) was attributed to the coordinatively unsaturated Fe cations at the edge of FeO_{1-x} islands which are oxygen deficient. Explanation from DFT calculations [212, 214] showed these edge-site coordinatively unsaturated Fe cations are highly active for O_2

adsorption and dissociation. The dissociated oxygen that binds to Pt at the FeO/Pt interface is responsible for the facile CO oxidation. The first direct evidence for such scenario came later from Wendt and co-workers[215] by time-lapsed STM imaging on FeO/Pt(111), which showed the appearance of O protrusions at reduced Fe-edges in O_2 and the following consumption in CO exposure, both in UHV-compatible pressure range.

Later, Bao's group also confirmed the formation of FeO_2 trilayer islands upon oxidation of the pristine FeO/Pt(111) films at sub-monolayer coverages[213]. They demonstrated the reversible transformation of FeO to FeO_2 by applying oxidation (5×10^{-6} mbar O_2, 573K) and UHV annealing at 573 K. Using XPS results as indicators of both phases, they claimed that the formation of oxidized phase (FeO_2) leads to the decreased reactivity, favoring FeO as the most active phase [213, 216]. This statement seems contradictory to results from our group. Pan et al. [217] studied CO oxidation on FeO/Pt(1 1 1) films at sub-monolayer oxide coverages at ultrahigh vacuum using TPD and near-atmospheric pressure conditions using gas chromatography. The authors found that the FeO(1 1 1) bilayer islands are inert towards CO_2 formation, whereas the FeO_{2-x} trilayer structure shows substantial CO_2 production that reaches a maximum at ~0.4ML at both pressure conditions.

Apart from the difference in the film preparation recipes and reaction conditions and methods by which the reactivity was measured, the key controversy is about the activity of FeO_2 phase. Series of studies from our group revealed: 1) FeO(111)/Pt(111) full is active in the low temperature CO oxidation reaction in the mbar pressure range due to the transformation of bilayer FeO to trilayer FeO_2 under the reaction conditions; 2) The activity of FeO_2 is closely related with the desorption energy of the weakly bound O; 3) CO oxidation reaction on fully covered FeO_2 films seems to proceed via the Mars-van-Krevelen mechanism. 4) The enhanced reaction rate at sub-monolayer coverages must be attributed to the FeO/Pt interface. However, Bao's group claims the much lower activity of FeO_2 /Pt by comparing with FeO/Pt in CO and O_2 mixture.

In this Chapter, we present studies on the preparation and thermal stability of FeO(111) films on Pt(111) in vacuum and CO, and CO+O_2. In addition, we studied the ultra-thin FeO(111) on Au(111), in order to understand the support effect on the structure, oxidation and reactivity of FeO/Au(111) by comparison with FeO/Pt(111) system.

4.2. FeO films on Au(111): preparation, oxidation and reactivity

Comprehensive studies of various metal-supported ultrathin films (FeO/Pt(111), RuO_2(110)/Ru(0001), MnO/Pt(111), ZnO/Pt(111)) CO oxidation revealed a strong correlation between the activity and the desorption energy of the most weakly bound oxygen species present on these films under net oxidizing conditions at

near-atmospheric pressures. Therefor the oxygen binding energy can serve as a good descriptor for this reaction on thin oxide films.

In the scenario of sub-monolayer coverages of oxide thin films, CO adsorption on metal substrate becomes crucial as well. Previews study of ZnO(0001) films revealed that CO oxidation rate increased considerably at sub-monolayer coverages when grown on Pt(111), but not on Ag(111)[218-219]. The effect was reasonably explained by a much stronger CO adsorption on Pt(111) as compared to Ag(111) which, in turn, increases the residence time for adsorbed CO to react with WBO supplied by ZnO. Therefore, the CO adsorption energy on metal substrate can be considered as another descriptor for the reaction, which may even dominate at sub-monolayer oxide coverages. Higher reactivity was also observed on sumonolayer FeO(111) grown on Pt(111) as compared with full film [217]. However, accompanied by the decreasing of oxygen binding energy at sub-monolayer FeO(111) indicated by the lower WBO desorption temperature, the reactivity increasing cannot be simply attributed to either descriptors above.

To shed more light on the reactivity of metal supported ultrathin films and elucidate the role of a metal support, in this section we show our results of FeO(111) thin films preparation, oxidation and reactivity supported on Au(111) in different coverages as a reference system with previously studied FeO(111)/Pt(111) system. In principle, different to Pt, Au is the most inert noble metal with respect to both CO and O2, and therefore, one can readily assign the observed reactivity (if any) to the iron oxide phase.

4.2.1. Preparation and oxidation of FeO on Au(111)

The Au(111) crystal was cleaned by repeated cycles of Ar^+ sputtering and annealing in UHV at 700 K until a typical Au(111) herringbone reconstruction was observed in STM as shown in Figure 4.2a. The step height of clean Au(111) in our study was found to be ~2.47 Å, comparable to 2.35-2.5 Å reported in the literature[220-223].

We followed the recipe reported by Khan and co-workers to prepare the single-layer FeO(111) film on Au(111)[157]. Firstly, Fe was deposited on Au(111) substrate in UHV at RT, then the Fe was oxidized in 3 x 10^{-7} mbar O_2 at 323 K for 8 min, finally the oxide film was smoothed by UHV annealing at 700 K for 10 min.

STM images after Fe deposition on Au(111) at different coverages are shown in **Figure 4-1**. Clean Au(111) surface is shown in **Figure 4-1 a,** the typical herringbone-like reconstruction is shown in the insert. After Fe deposition at room temperature, the large-scale images (**Figure 4-1 b,d**) show that Fe grows in an ordered array and does not accumulate at step edges. This ordered nucleation of Fe on Au(111) derives from the preferential Fe attachment on the elbow sites of the

herringbone reconstruction (**Figure 4-1 c**), where the surface dislocations bring unsaturated Au atoms[220, 224]. At all coverages, the particles are very uniform and mostly appeared triangular like or round with some sharp edges as present in smaller scale images (**Figure 4-1c,e,f**). At 0.2ML, the particles are approximately 2-5 nm in lateral size, they grew up to 5-7 nm and started coalescence at 0.8ML, further coverage increasing to 1.2ML renders Fe to coalesce to continue lines. Notably, at 0.2ML the second layer has started to nucleate on the first layer of particles. The thickness of single layer island is approximately 2.5 Å which is slightly smaller than the Fe atomic diameter of 2.8 Å.

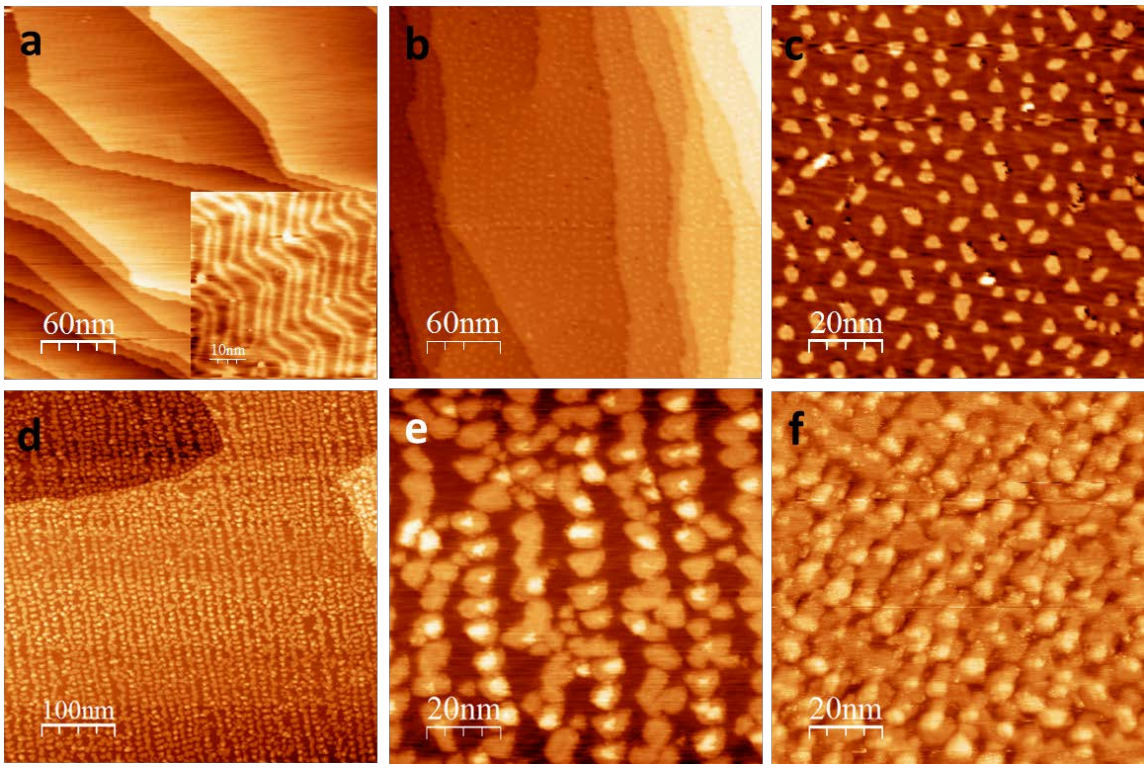

Figure 4-1. STM images of (a) clean Au(111) surface, the typical herringbone-like reconstruction is shown in the insert. (b-f) after deposition of Fe in different coverage: (b,c) 0.2ML; (d,e) 0.8ML; (f)1.2ML. STM Tunneling conditions: (a)0.6 V, 0.1 nA , insert 0.6V, 0.05nA; (b)0.5 V, 0.1 nA; (c) -1.0 V, 0.5 nA; (d) -0.5 V, 0.08 nA; (e) -0.5 V, 0.1 nA; (f) -1 V, 0.1 nA

After following low temperature oxidation and final annealing, the FeO(111) films are present in **Figure 4-2.** Estimation of total amounts of FeO in all three samples reveals that the final surface Fe coverage decreases by 40%-50% as compared with the initial amount Fe deposited. The equivalent FeO coverage is ~0.1ML, 0.45ML and 0.8ML apparently. This may mainly derive from the Fe diffusion into subsurface region after low temperature annealing, which was also observed by Khan et al. [157] by LEIS. For the ~0.1ML FeO sample (**Figure 4-2a**), the particles appear blurry and coalesced to larger entities compared with the Fe islands. Surprisingly, most particles were embedded in the terrace or attached to the terrace edge, together with triangular pits distributing on the terraces. Similar images were

also reported by Khan et al. The pits should relate with the embedded iron oxide particles in Au(111) steps, but the detailed formation process is not well-understood.

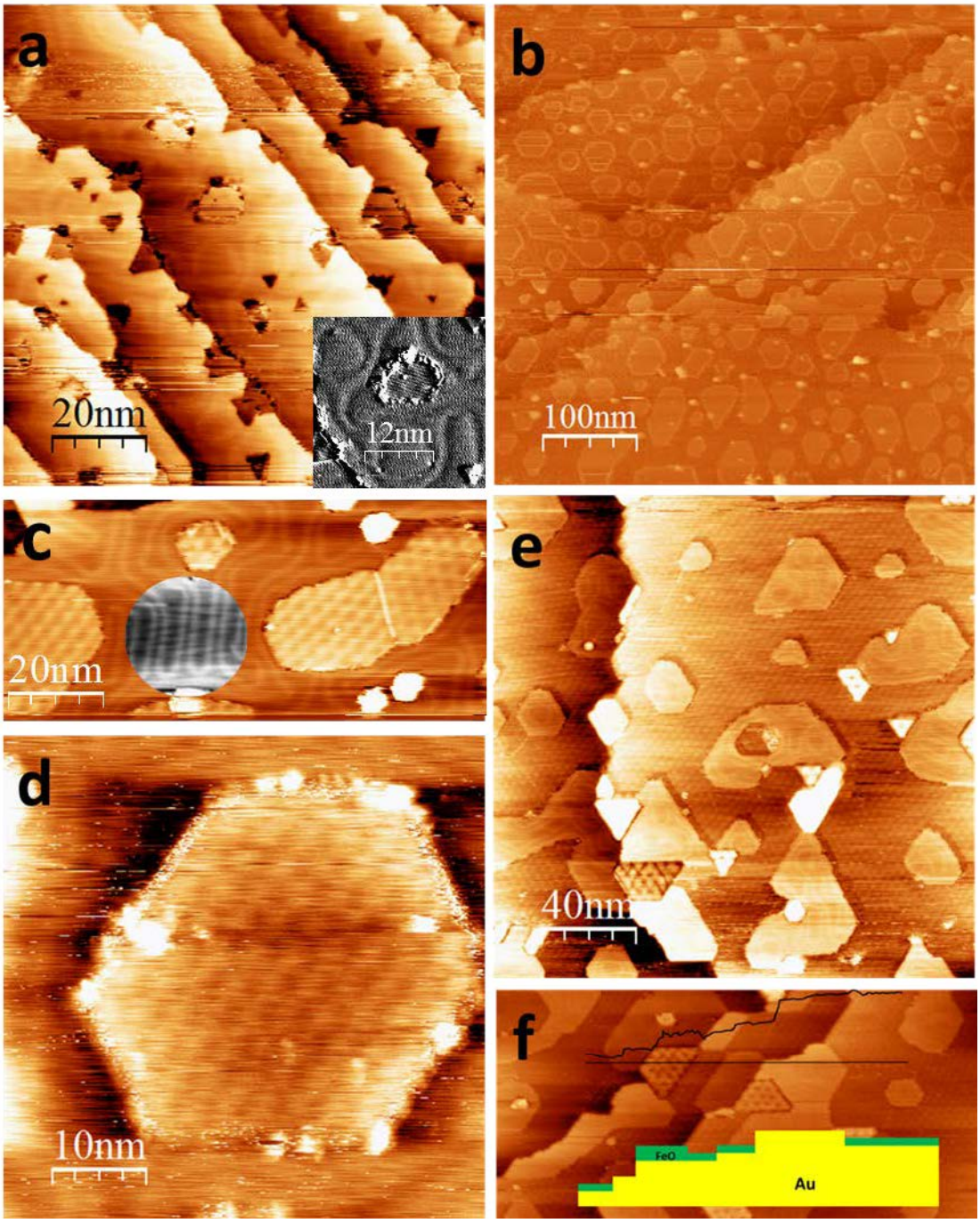

Figure 4-2. STM images of as prepared FeO(111) supported on Au(111) at different coverages: (a) 0.1ML; (b,c,d) 0.45ML; (e,f) 0.8ML. The distorted herringbone reconstruction are indicated by dashed black lines in (a, c, e). The grayscale image inserts in (a, c) with a high contrast show the distorted herringbone reconstruction. Insert in (f) presents the schematic diagram of side sectional view of the film and the thickness profile as indicated by the black line. STM Tunneling conditions: (a) -0.1V, 0.1nA; (b)-0.06 V, 0.1 nA (c) -0.7 V, 0.15 nA; (d)-0.07 V, 0.14 nA; (e,f) -1.0 V, 1.2 nA.

For the sample of 0.45 ML FeO(111) coverage, large-scale image (**Figure 4-2b**) shows that FeO particles lost the ordered arrangement of Fe island but still distributed uniformly. In high-resolution images (**Figure 4-2c,d**), the reconstruction corrugation lines appear to move around the particles in contrast to the Fe metal particles which grow on the elbows of the reconstruction. FeO(111) islands are readily identified by the Moiré structure with a ~30 Å periodicity (**Figure 4-2c,d**). The apparent height of the islands is about 0.8 Å (depending on the tunneling conditions, though). Note also, that under certain tunneling conditions the island edges look much higher than the interior region, thus indicating very different electronic structure of the step edges.

As shown in **Figure 4-2e,f** are STM images of the sample which was prepared by deposition of 1.2 ML Fe to form a continuous FeO(111) film with equivalent film coverage of 0.8ML. The Au and oxide surfaces in the film displayed in **Figure 4-2e** can clearly be distinguished by the "herring-bone" (on Au) and Moiré (on FeO) patterns. In contrast to the low coverage regime, Au(111) ad-islands are surrounded by the FeO(111) surface. This formation of Au islands on the Au(111) surface has also been observed after lifting the reconstruction by high exposures to CO[225]. These islands are most likely resulted from ~4 % excess of the Au atoms accommodated in the top layer [226-227]. Profile analysis indicates that two layers' thick iron oxide islands may also be formed as shown in in the insert of **Figure 4-2f**.

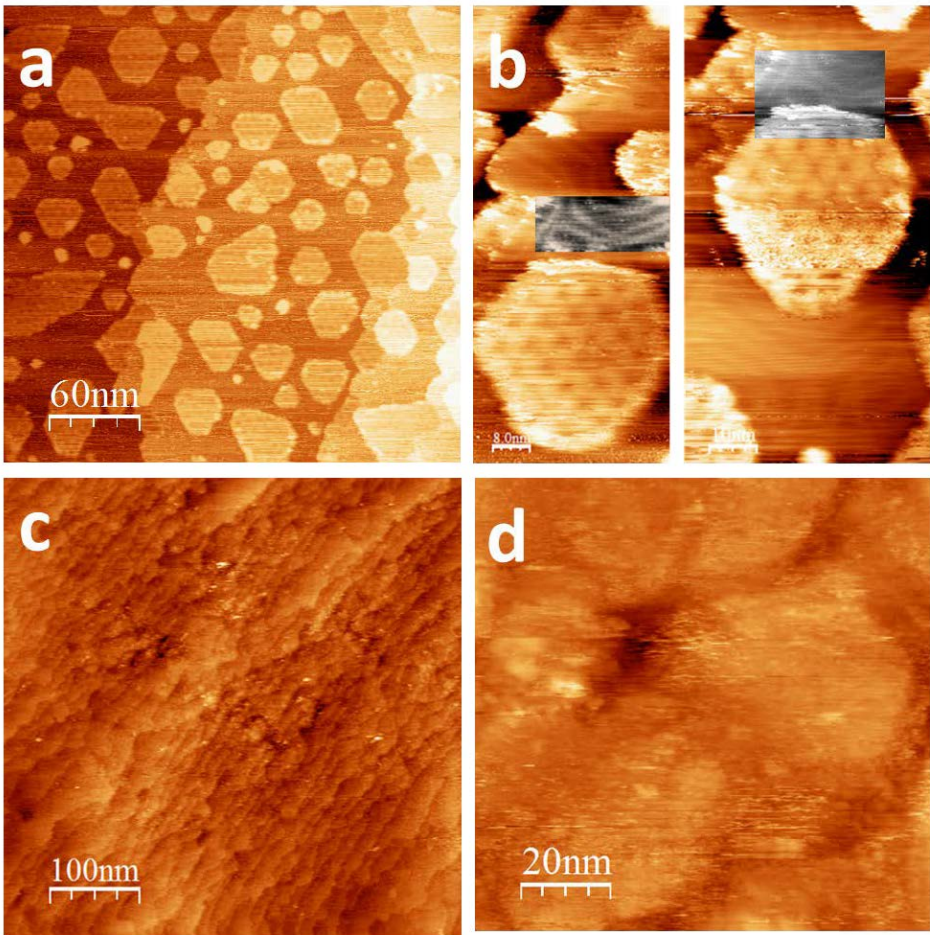

Figure 4-3. STM images of oxidized FeO/Au(111): (a,b) 0.45ML; (c,d) 0.8ML. The distorted herringbone reconstruction is indicated by dashed black lines in (b). The grayscale image inserts in (b) with a high contrast show the distorted herringbone reconstruction. STM Tunneling conditions (a)-1.0 V, 0.14 nA ; (b) -0.9 V, 0.08 nA; (c)-1.0 V, 1.2 nA; (d) -2.1 V, 0.5 nA.

To directly link to reactivity measured in the mbar range, we oxidized the as prepared film in 10 mbar of O_2 at 470 K. STM images of the 0.45ML sample are displayed in **Figure 4-3a**. Basically, the film morphology remains the same: The lateral size and shape of oxide islands are not changed, and the "herringbone" Au(111) surface between islands can still be resolved. However, the Moiré periodicity on the islands increased from ~30 to ~45 Å. This finding well agrees with the LEED results we got in another chamber showing that the lattice constant considerably decreases upon high-pressure oxidation.[115] Indeed, a shortening of the FeO(111) lattice constant reduces the mismatch with the Au(111) surface and hence increases the periodicity of the coincidence structure, which can be described as $14\times aFeO_x=15\times aAu(111)=43.2$ Å, using $a(FeO_x)=3.08$ Å [115]. In addition, the islands height increased from initial 0.8 to 1.5 Å, albeit both affected by the tip conditions and tunneling parameters.

In contrast to the 0.45ML sample, oxidation of the 0.8ML sample, showing extended FeO(111) patches, resulted in substantial surface reconstruction as shown in **Figure 4-3b,c**. The terraces now expose such a rough surface that oxide and metal phases can hardly be differentiated. Although the structure of the film underwent substantial reconstruction, oxygen enrichment of this sample seems consistent with the low coverage sample, which is confirmed by the following TPD and AES measurements.

As shown in **Figure 4-4**, the O/Au intensity ratio comparison indicates that the films became enriched in oxygen and approached the formal stoichiometry FeO_{1+x} (x~0.27 at 0.45ML and ~0.38 at 0.80ML) upon exposure to 10 mbar O_2 at 470 K as measured by AES. However, in the case of FeO(111)/Pt(111), same treatment gave the x as 0.8-0.9 due to the transformation from Fe-O bilayer to an O-rich O-Fe-O trilayer structure. Less O enrichment in Au(111) supported films than in Pt(111) supported ones manifests formation of another O-rich phase on Au(111).

The oxygen enrichment is also evidenced by TPD. In order to avoid the risk of damaging the Au crystal because of the low melting point, heating was stopped at 850 K, which is not sufficient to decompose the FeO overayer, usually occurring at around 1150 K. Only negligible amounts of oxygen desorption was detected from O-rich FeO /Au(111) samples at both coverages. The peak area basically scales with the film coverage increasing from 0.45ML to 0.8ML.

The TPD experiments were also conducted in another set up for both FeO/Pt(111) and FeO/Au(111) systems [115]. Again, the results shows that desorbed O_2 on FeO_{1+x}/Au(111) surface is much smaller than that on FeO_2/Pt(111) and constitutes only ~5% of that on 1 ML FeO_2/Pt(111) surface. Since dissociative adsorption of O_2 on Au single crystal is not energetically favorable [228], it appears that this is essential to

facilitate the oxidation of FeO into FeO_2 when supported on Pt(111). As a result, less oxidized iron oxide phase is observed on Au(111).

Limited resolution of the STM images cannot provide direct evidence for atomic structure of the O-enriched phase. However, there is a certain effect of high pressure oxygen treatment on FeO(111) islands, ultimately causing changes in the surface lattice parameter and island height as measured by STM. On one hand, such a "thickening" would be consistent with the formation of additional O-layer in the structure. On the other hand, the amount of WBO measured by TPD is equivalent to about 8 additional oxygen atoms that have to be distributed in the entire Moiré supercell, which in turn consists of 80 FeO(111) unit cells. In principle, a shortening of the surface lattice constant could readily increase the surface rumpling and hence the apparent height[229]. The interpretation to the detailed structure of the O-enriched phase needs further DFT calculations.

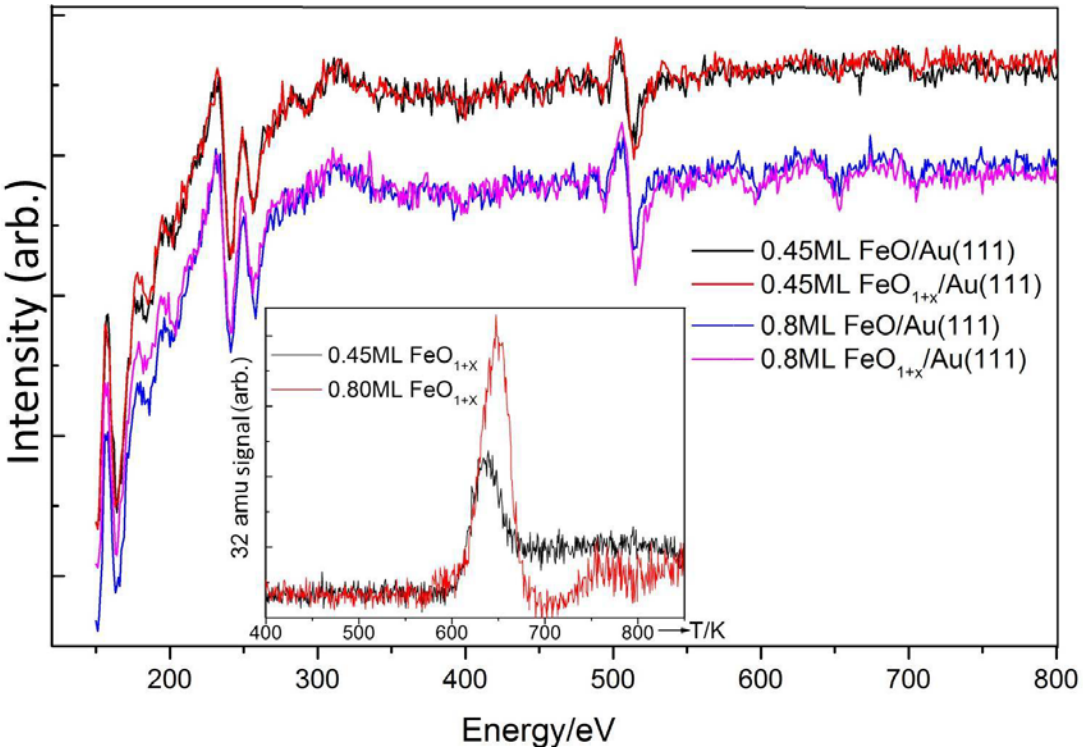

Figure 4-4. AES spectra of the 0.45ML and 0.8ML FeO/Au(111) films before and after oxidation in 10 mbar O_2 at 470 K. Insert: 32 amu (O_2) signal in TPD spectra of oxidized films. The heating rate is 2 K/s.(see text)

4.2.2. CO oxidation on FeO/Au(111)

CO oxidation reaction on FeO/Au(111) was tested in another setup which was not equipped with STM to directly measure the FeO(111) coverage. Therefore, we first address coverage calibration. Film thicknesses estimated from XPS and/or AES measurements using tabulated values for fitting parameters (such as a mean free path

of electrons and across section) which are commonly derived from experiments performed on few nanometers thick films becomes rather inaccurate in the case of ultrathin, e.g. monolayer films[230].

In our previous study, the coverage of sub-monolayer FeO(111) films supported on Pt(111) could be determined by CO titration of the bare Pt surface with TPD since FeO(111) does not adsorb CO[217]. However, in the case of Au(111) as a substrate, the metal surface could hardly be titrated by CO and other probe molecules because all desorption signals on Au(111) at temperatures above 90 K accessible with our setup are commonly associated with the surface defects. Nevertheless we can calibrate the coverage of ultra-thin FeO/Au(111) by taking FeO/Pt(111) as a reference and linking two systems via AES. The rationalities of this approach is based on certain prerequisites:

1) Precise morphology of the islands does not affect the CO uptake results as the DFT calculations showed only small changes of the CO adsorption energy for the Pt sites close to FeO(1 1 1) islands as compared to the regular sites.

2) Au and Pt, being neighbors in the Periodic Table, exhibit similar fingerprints in AES (and XPS). A very small kinetic energy difference of Auger electrons in Au and Pt (239 and 237 eV, respectively) implies the same mean free path.

3) Measurements on both systems were carried out with the same spectrometer and the same parameters (e.g. excitation energy, oscillation voltage, acquisition time, etc.) all apparatus effects are self-cancelled.

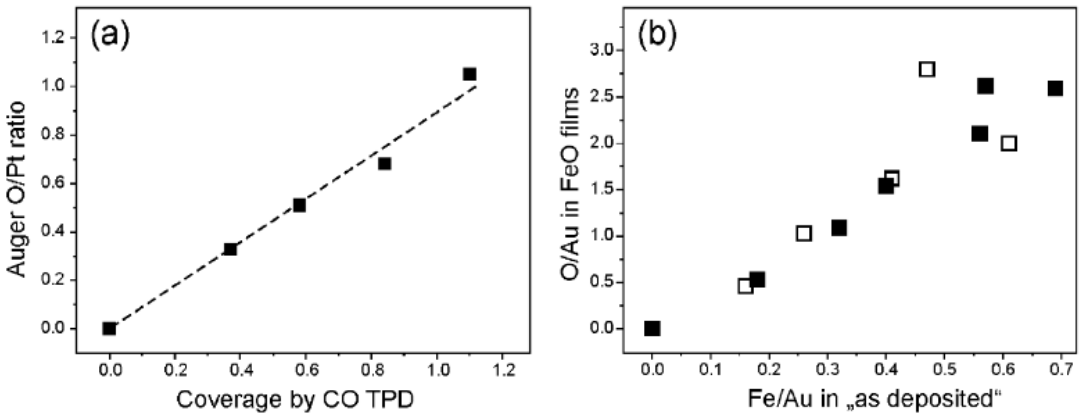

Figure 4-5. (a) The relationship between the Auger O(512 eV)/Pt(237 eV) signal ratio and film coverage obtained for FeO(111)/Pt(111) films and measured by CO titration.(NB: The sample at 1.1 ML showed no CO uptake and the coverage was determined by extrapolation using the Fe deposition time). (b) The relation-ship between the Auger Fe(653 eV)/Au(239 eV)signal ratio obtained after Fe deposition on Au(111)and the O(512 eV)/Au(239 eV) signal ratio measured after oxidation step. The opened and filled symbols show data for the samples used for reactivity

studies and structural characterization upon high pressure oxygen treatment, respectively. (The results in (a) are provided by Dr. Pan)

The intensity ratio of the O (at 512 eV) and Pt (at 237 eV) Auger electrons is linearly proportional to the FeO coverage measured by CO uptake as shown in **Figure 4-5a**. Because the elemental sensitivity of the corresponding Auger line in Au is about 5 % higher than in Pt.[230] the FeO(111) coverage on Au(111) can fairly well be determined by measuring the intensity (I) of the O(512 eV) and Au(241 eV) signals and taking into account a 5 % higher elemental sensitivity of Au as compared to Pt. This finally results in the FeO(111) coverage (θ_{FeO}, in ML) on Au(111) as:

$$\theta_{FeO/Au} = \frac{I_{O@512eV}}{I_{Au@239eV}/1.05} \times \frac{1}{S_{FeO/Pt}} = 0.95 \times \frac{I_{O@512eV}}{I_{Au@239eV}}$$

Where $S_{FeO/Pt}$ is the slope of the curve in **Figure 4-5a**.

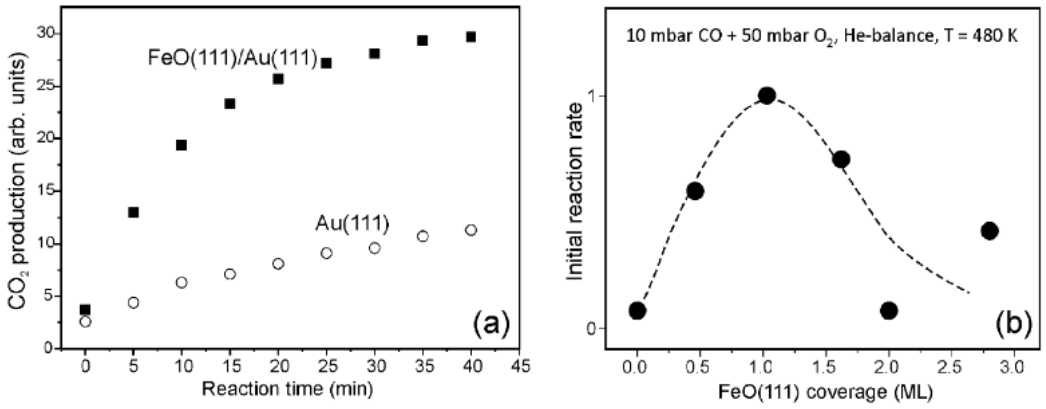

Figure 4-6.(a) Kinetics of CO_2 production in the circulating mixture of 10 mbar of CO and 50 mbar of O_2 (He balance to 1 bar) on the pristine and FeO(111) covered Au(111) surfaces at 480 K. (b) The initial rate as a function of the FeO coverage.(measured by Dr.Weng [115])

The reactivity was performed in the circulating mixture of 10 mbar of CO and 50 mbar of O_2 (He balance to 1 bar) at 480 K. The reaction was performed in excess of oxygen in order to avoid film dewetting occurred in stoichiometric or CO-rich conditions in FeO/Pt(111) system[112].

Figure 4-6 presents a comparison between the CO_2 production on FeO/Au(111) and Au(111) single crystal. As expected, the clean Au(111) surface is inert in this reaction. (Some CO_2 production can be attributed to reactions on the sample holder and heating wires). We focus solely on the initial reaction rate measured within the first 10-15 minutes. The rate strongly depends on the FeO(111) coverage and shows a maximum at about 1 ML (**Figure 4-6b**). Data scatter at high coverages where iron oxide phases other than monolayer FeO(111) can readily be formed[157].

Such a volcano-type curve has previously been observed in our experiments on FeO/Pt(111)[217] but the highest rate was got at the 0.4 ML. So the active sites at

oxide-metal interface were invoked for explanation. Apparently, maximum rate obtained at about 1 ML in FeO/Au(111)system, the reaction is related to the total surface area of the FeO(111) phase rather than the interface premier. These results suggest that: 1) the reaction primarily occurs on oxide surface rather than at oxide/metal interfacial sites; 2) at nominal film thickness above 1 ML, other structures start to form which are inactive in this reaction, but dominate at high film thicknesses. Both conclusions are quite different with the scenario of sub-monolayer FeO/Pt(111). Indeed, CO very weakly adsorbs on the Au(111) surface in contrast to Pt(111), and hence the reaction on Au supported islands does not benefit from having the oxide/metal interface. With increasing nominal film thickness above one monolayer, FeO(111) may transform into another phase such as Fe_3O_4(111) which shows no rate enhancement[112].

4.3. FeO(111) films on Pt(111) at sub-monolayer coverage

4.3.1. Preparation

Structure and preparation of ultrathin FeO(111) film supported on Pt(111) has been extensively studied since early 1990s[231-235]. Generally, these two-steps preparation recipes can be divided to two categories: 1) Fe deposition in UHV followed by high temperature postoxidation[231-233, 235], which is adopted by our group, denoted as **Recipe I**; 2) Fe deposition in O_2 followed by UHV annealing[212-213, 234], which is adopted by Bao's group, denoted as **Recipe II**. Both kinds of recipes can give a well-ordered FeO(111) film and the annealing temperature is crucial for the morphology at sub-monolayer FeO coverage. Previously, our group used oxidation in the pressures of mbar range, while Bao's group found that that sub-monolayer FeO on Pt(111) can be transformed into FeO_2 upon oxidation in 5.0×10^{-6} mbar O_2, and the FeO to FeO_2 transformation on closed FeO film occurs at the O_2 partial pressure above 1.0×10^{-3} mbar. In order to compare and see the difference, if any, we examined both recipes in one setup. In the first part of this section, we will address morphology evolution of 0.7ML FeO(111) with different temperature post-annealing and their transformation to FeO_2. In the second part we studied 0.5ML FeO(111) oxidized in mbar range and ~$5x10^{-6}$ mbar O_2.

The cleanness of Pt(111) surface was first checked by AES and STM to ensure the complete consumption of C contamination as shown in **Figure4-7a.** 0.7 ML FeO(111) was prepared by **Recipe I**: 0.7 ML of Fe was deposited onto Pt(111) single crystal at room temperature followed by oxidation in 1 x 10^{-6} mbar O_2 at 900 K for 2 min, STM images are shown in **Figure4-7b,c**. FeO(111) shows as almost continuous film with some uncovered hexagonal-like "holes" and exhibits the well-known Moiré pattern with periodicity of ~2.5 nm and a corrugation amplitude of ~0.1 Å[102]. In addition, some second-layer islands attach at the edge of the holes.

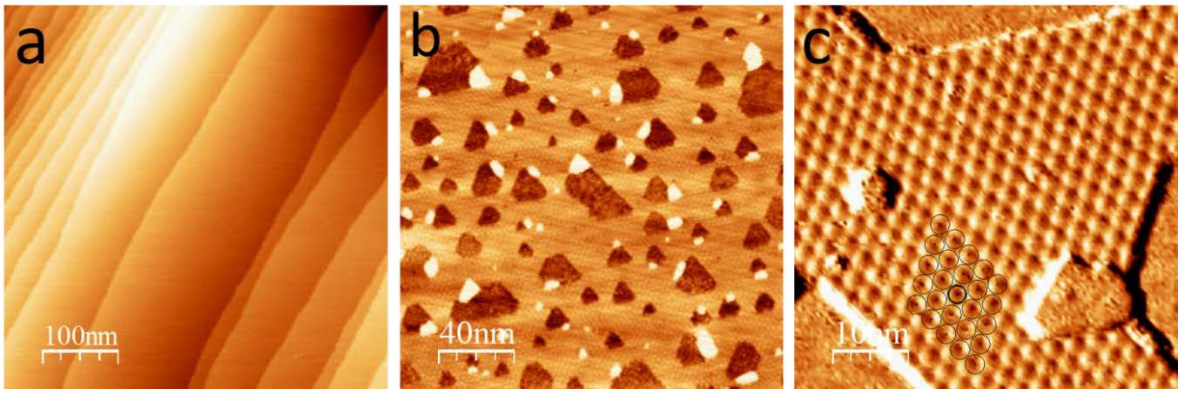

Figure 4-7. STM images of (a) Clean Pt(111) single crystal surface; (b, c) 0.7ML FeO(111). Tunneling conditions: (a)1.0V, 0.3nA; (b, c)-0.7, 0.09nA.

Then we prepared FeO(111) following **Recipe II**. 0.7ML Fe was reactively deposited in $1x10^{-7}$mbar O_2 at room temperature, and then annealed in UHV at different temperatures. Corresponding STM images are shown in **Figure 4-8.** Applying 570K post-annealing, most islands are highly dispersed and worm-like with width of ~7 nm **(Figure 4-8a)**. Increasing the annealing temperature to 673K results in aggregation of the FeO nano-islands with more regular shape, and they are still highly dispersed**(Figure 4-8b)**; further temperature increasing renders FeO to form continuous film with uncovered holes **(Figure 4-8c)** just like what we observed for **Recipe I** in **Figure 4-7b.** High resolution images show the same Moiré pattern periodicity with the film prepared by **Recipe I** too, which indicates the films prepared by both recipes are all FeO(111), except the final morphology depending on annealing temperature.

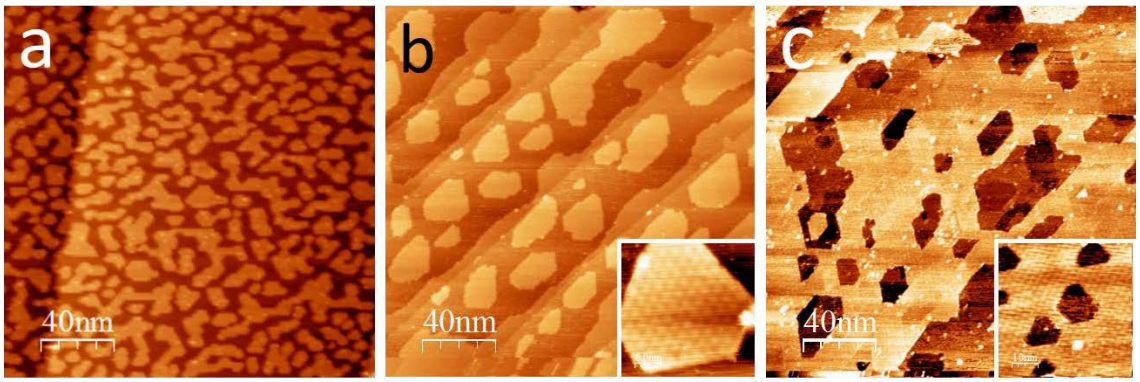

Figure 4-8. STM images of 0.5ML FeO(111) with elevated post-annealing temperatures: (a) 570K; (b)670K; (c) 770K. Inserts are higher resolution images. Tunneling conditions: (a) 2.0V, 0.1nA; (b) 3.0V, 0.05nA; (c) 2V, 0.1nA.

Next step, we oxidized the sub-monolayer FeO(111) prepared by **Recipe II** in 10 mbar O_2 at 470K and $5x10^{-6}$mbar O_2 at 570K respectively, which is in accordance

with the FeO_2 preparation recipes reported by both groups. Corresponding STM images are shown in **Figure 4-9**. Both samples show similar morphology: compared with the pristine FeO(111), the Moiré periodicity of the both oxidized samples have been kept but the surface corrugation become larger, all typical FeO_2 features reported. However, there are more surface contaminations on FeO_2 oxidized at 10 mbar O_2 **(Figure 4-9a,c)**, which could, in principle, be attributed to hydroxyl species derived from reaction of the FeO_2 surface with traces of water at such high pressures [211].

The conclusion that sub-monolayer FeO structure can be oxidized to the FeO_2 trilayer structure under high vacuum and mbar range oxidative conditions is in consistent with Bao's group[236]. With respect to the necessity of O_2 partial pressure above 1.0×10^{-3} mbar range for full coverage sample oxidation, the ease oxidation in ~10^{-6} mbar for sub-monolayer sample may be due to the presence of opened Pt surface, which facilitates the O_2 dissociation and O intercalation at the FeO/Pt interface [236].

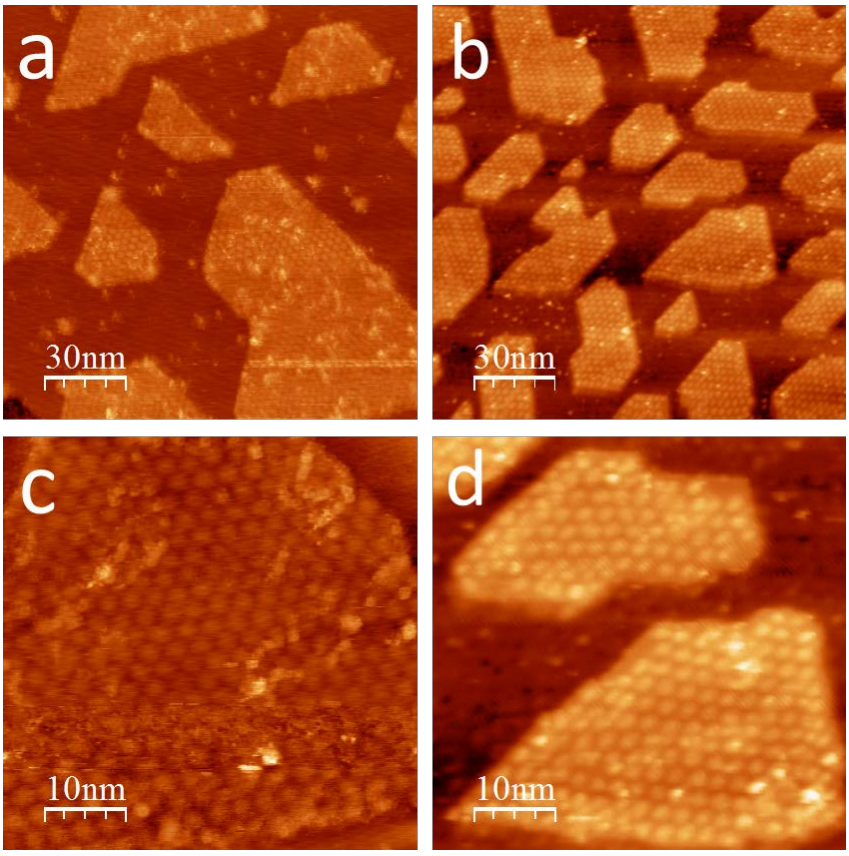

Figure 4-9. STM images of FeO(111) oxidized (a,c) in 10mbar O_2 at 470K and (b,d) 5x10^{-6}mbar O_2 at 570K. Tunneling conditions: (a,c) -1.5V, 0.1nA; (b,d) 2.0V, 0.1nA.

4.3.2. Thermal reduction of sub-monolayer FeO_2/Pt(111)

Our group's study of various metal-supported ultrathin films (ZnO, FeO, RuO_2 and MnO) in CO oxidation reveals that the reaction rate is inversely proportional to the binding energy of the most weakly bound oxygen,[142] at least for fully covered films. For FeO/Pt(111) system, coverage decreasing to 0.6ML gives rise to a lower O_2 desorption temperature [217], which can be used as a qualitative measure of the WBO binding energy. Apparently, the WBO binding energy is dependent of the film structure changes brought by the sub-monolayer coverage, which is in agreement with the recent results of ref [237]. In order to shed more light on this issue, we examined thermal reduction of sub-monolayer FeO_2/Pt(111) by STM, TPD and AES.

The experiment was performed on a 0.5ML FeO/Pt(111) sample. After oxidative treatment at 10mbar O_2 and 470K, the obtained FeO_2 was firstly flashed to 870K to get a full desorption curve of WBO. Then the sample was re-oxidized and stepwise flashed to 630K and 700K in front of the QMS to record the O_2 desorption. Followed every flash, AES and STM measurements were conducted to measure composition and morphology changes. Subsequently, 900K UHV annealing was applied to completely reduce the FeO_2 to FeO. At last, we re-oxidized the sample again.

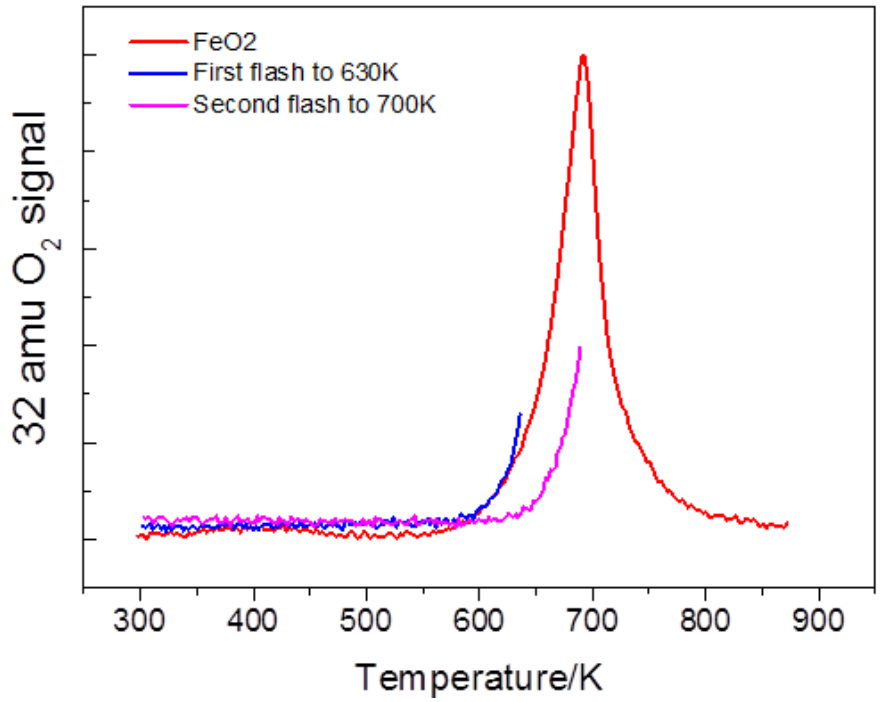

Figure 4-10. O_2 (32 amu) TPD spectra of 0.5ML FeO_2/Pt(111). Heating rate is 2K/s. (see the text)

Figure 4-10 shows O_2 TPD spectra. Continuous heating to 870K gave rise to a desorption peak that starts at ~600K and reaches the maximum at 702K. This peak is at considerably lower temperature than previously observed for the closed films, i.e. at ~850 K. The first flash only to 630K basically coincides with the previous spectrum.

The second flash to 700K starts, however, at the final temperature of the previous TPD run, i.e. at 630K. STM images after every heating are presented in **Figure 4-11.**

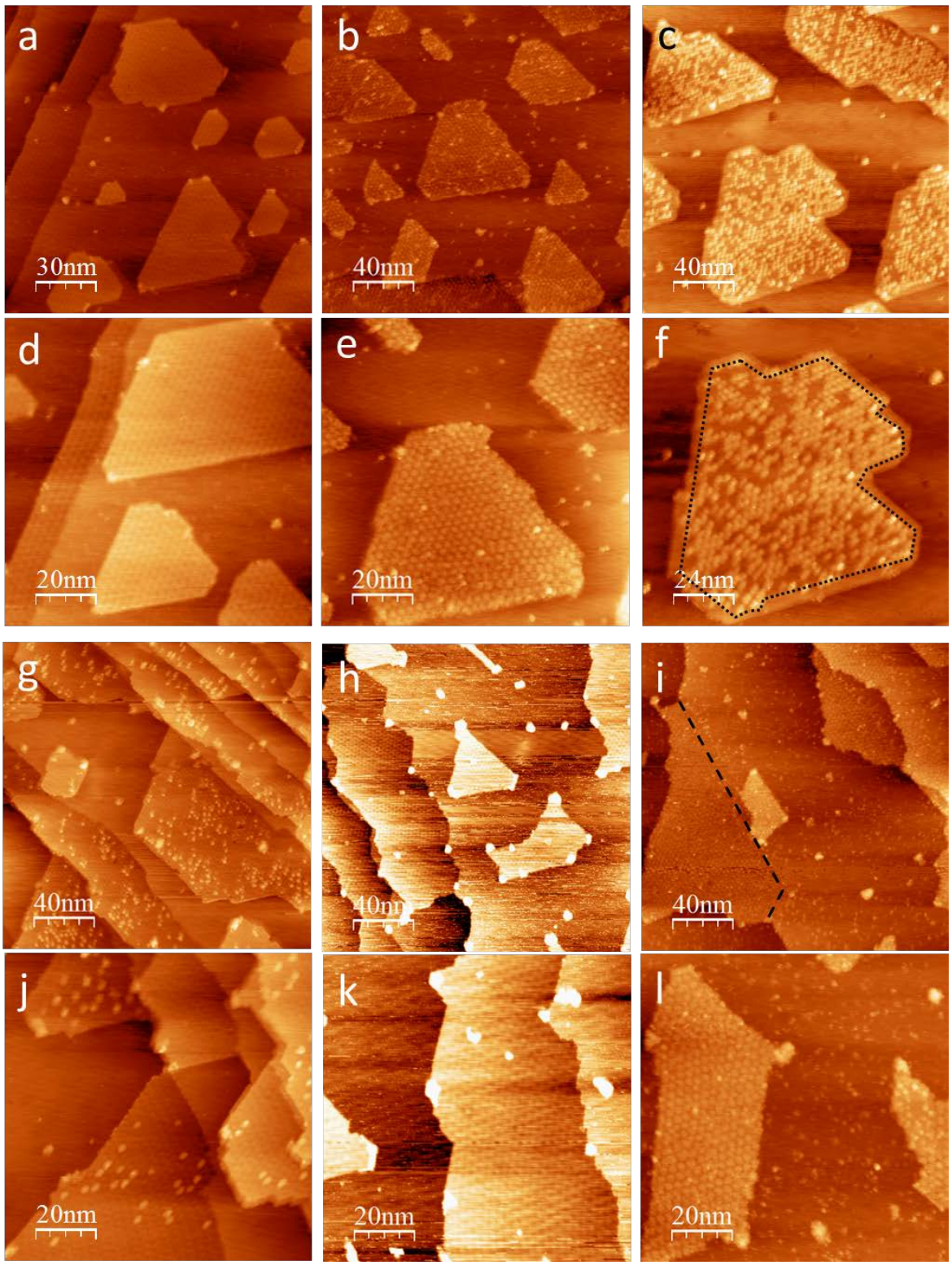

Figure 4-11. STM images of as prepared FeO(111) (a,d), oxidized to FeO_2(b,e), flash to 630K(c,f); further flash to 700K(g,j); following annealing at 900K for 1min(h,k); re-oxidized to FeO_2(i,l).

Dashed profile line in (f) represents the border of undesorbed top layer O; dashed broken line in (i) represents the interface between FeO island and the Pt terrace. Tunneling conditions: (a,) -2.4V, 1.6nA; (d)-2.0V, 1.6nA; (b,e)-1.8V, 0.5nA; (c,f)-1.8V, 1.1nA; (g) -1.8V, 0.7nA; (j) -1.7V, 1.0nA; (h, k) -2.2V, 1.0nA; (j) -1.7V, 1.0nA; (i) -1.8V, 1.0nA; (j) -2.0V, 1.0nA;

STM images of the "as deposited" FeO(111) **(Figure 4-11a, d)**, which shows individual islands with Moiré structure on top as presented in last section. After oxidative treatment at 450K in 10mbar O_2, AES shows a ~2 times enhancement of O signal at 510eV **(Figure 4-12 red)**. General morphology of the obtained FeO_2 phase remains the same, except larger surface corrugation of the Moiré structure and more surface contaminations both on the support and oxide islands **(Figure 4-11b, e)**. Interesting phenomena appears after 630K flash: The Moiré spots like domains related to FeO_2 structure disappears but not randomly. Those are mostly missing at the edge of the islands, thus forming FeO_2 - free "belt" with width of ~3.5nm alongside the edge as highlighted by the dashed line in **Figure 4-11f.** Although desorption may also happened in the inner part of islands, the preferential desorption at the edge is obvious, which indicates the weaker bonding of oxygen at the edge of the islands. Thus the continuity of desorption in the second TPD run that starts at 630K become reasonable; the onset desorption temperature of the oxygen left at the rim of WBO region of the FeO_X island is 630K. The amount of FeO_2 features becomes less after 700K flash. **(Figure 4-11g, j)** This may suggest the movement of top layer O is activated in between 630-700K. The FeO_2-free area shows virtually identical Moiré structure as of pristine FeO(111). Also O signal intensity gradually decreases compared to the oxidized FeO_2 phase in AES spectra **(Figure 4-12 blue, pink)**. Final UHV annealing to 900 K completely decomposes the FeO_2 leaving a FeO/Pt(111) behind **(Figure 4-11h, k)**, also confirmed by the Fe:O ratio in AES **(Figure 4-12 green)**. In addition, the islands' coalescence was also observed and the islands shape became irregular. After following reoxidation, the FeO_2 structure is recovered as shown in **Figure 4-11i, l** and the corresponding AES signal (**Figure 4-12 deep blue**) is equivalent to that of original FeO_2(**Figure 4-12 red**).

The desorption temperature can be used as a qualitative measure of the WBO binding energy. Lower desorption temperature of top layer O at the edge compared with at interior of the islands is in consistent with the DFT+U results of Giordano et al.[238] Their model is composed of regions of bare and FeO(111)-covered Pt(111) surfaces that coexist with regions of embedded FeO_2 trilayer islands. They found that the easiest to reduce are the edge sites of the FeO_2 islands, with the desorption energy as low as 0.71 eV. O desorption (vacancy formation) is accompanied by a substantial electron transfer towards the Pt substrate, and the structural relaxation enables a local recovery of the quasiplanar FeO structure. The second easiest desorption site locates at FeO_2/FeO boundary with desorption energy of 1.38eV. This configuration completely supports the ordered desorption of top layer O from the edge towards the center of the island as shown above.

In the next step, we monitored reaction of FeO_2 islands with CO.

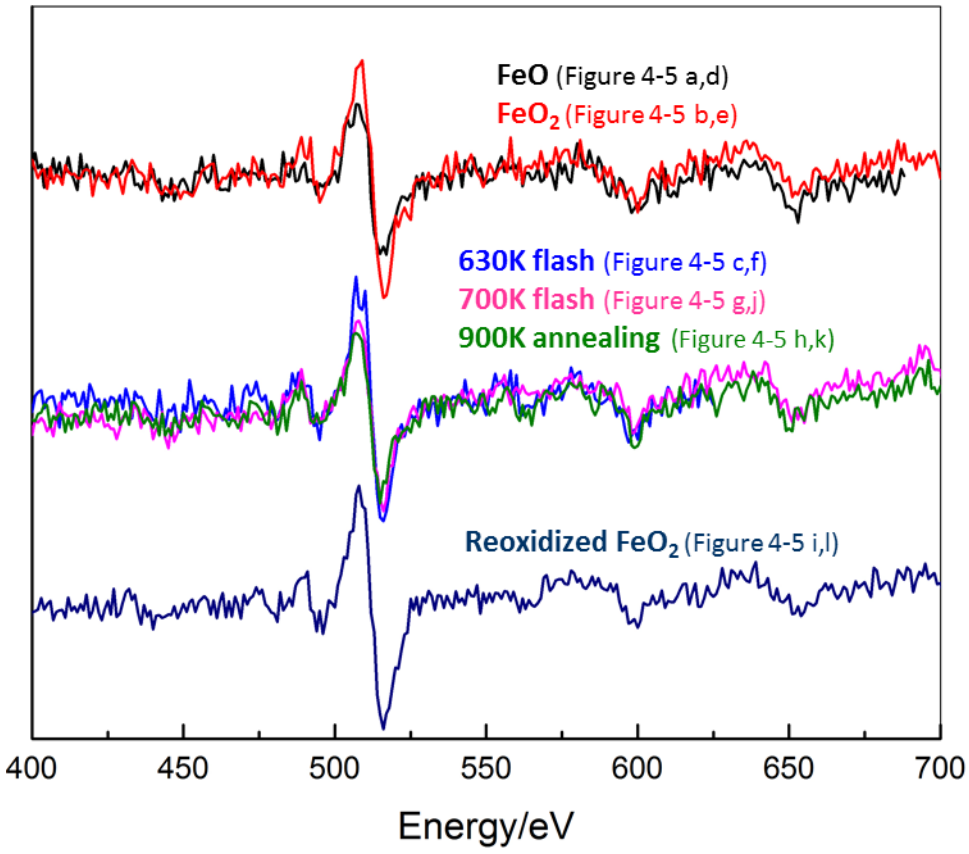

Figure 4-12. AES of FeO(111) corresponding to STM images in Figure 4-11.

4.3.3. CO reaction with FeO_2/Pt at sub-monolayer coverage

Mars-van-Krevelen process for CO oxidation on full oxide film surfaces includes CO oxidation by the oxide lattice oxygen and O vacancy replenishment by gas phase oxygen. Our group's work provided solid evidence that the full coverage FeO(111) is inert to CO oxidation, but the O-enriched FeO_2 phase formed in mbar rage oxygen or oxygen-rich mixture gas is quite active. Experiment and DFT calculation suggest the reaction process follows Mars-van-Krevelen mechanism [113-114, 153-154]:

1) Ambient CO binds strongly at the C end to one lattice O in the top layer of FeO_2, with formation of a CO_2 molecule that desorbs leaving an oxygen vacancy.

2) Oxygen vacancy is replenished by one O atom of the O_2 molecule and the second O react with CO to produce another CO_2 molecule

Note that the above scenario was suggested on close, dense films. In the case of the sub-monolayer coverage, the reaction rate is enhanced, which reaches a maximum at approximately 0.4 ML.[217] It was suggested that CO adsorption on Pt at the periphery of FeO_2 island increases the residence time to react with WBO supplied by

the island edge through a Langmuir-Hinshelwood mechanism.

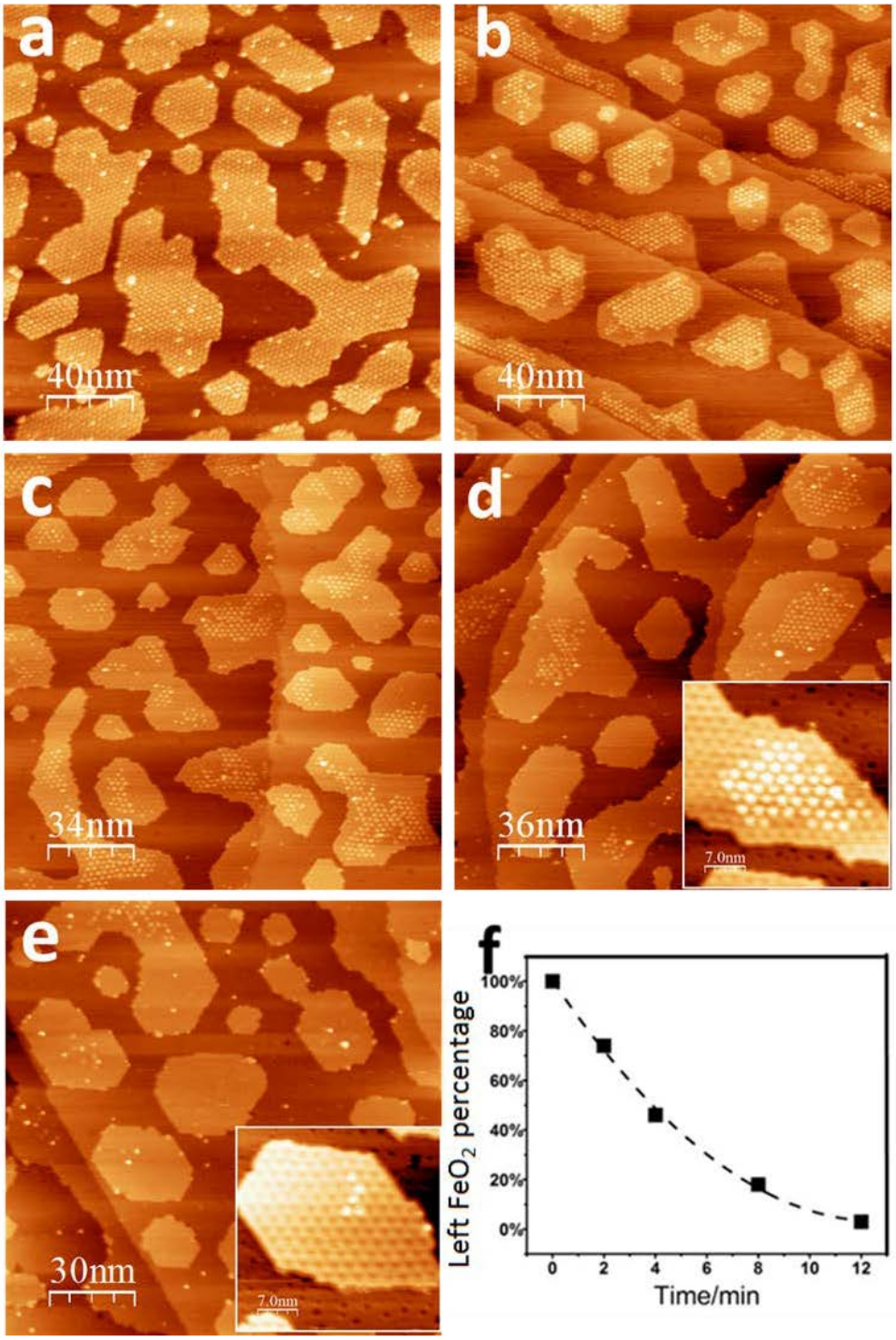

Figure 4-13. STM images of top layer O change with CO exposure time: (a) as oxidized; (b-e): elapsed time of 2min, 4min, 8min, 12min. inserts in d and e are the zoom in images to show the left FeO-like surface underneath the top layer O; (f) shows the top layer O amount decreases with CO exposure time with quadratic fit. The temperature is 450K. Tunneling conditions: (a, b)-3V, 0.1nA; (c, d)-3V, 0.07nA; (e)-3V, 0.06nA.

Based on the above O desorption results and previous results for CO oxidation,

the following experiment was performed in ambient CO of pressure $1x10^{-6}$ mbar at different temperatures to monitor the reaction of FeO_2 islands with CO. After certain time's exposure, the sample was observed by STM. Prior to the experiment, the fully-oxidized samples were annealed at corresponding temperatures in UHV (without CO) as blank experiment and no O desorption was observed in the temperature range of 450-300K.

STM images of sample exposed to CO at 450K for the different times are shown in **Figure4-13**. The first 2min reaction eliminates the Moiré spots-like FeO_2 domains at the edge of islands. As exposure time increases, the reaction propagates from islands' edge to interior. The resulted FeO_2-free region shows the structure virtually identical of the pristine FeO/Pt(111) (inserts of **Figure4-13d,e**). The island was completely reduced to FeO(111) after 13min exposure in total (not shown here). The reduction kinetic determined by STM is shown in **Figure4-13f**. The decay is fitted with an excellent parabolic fit for the left FeO_2 area percentage with exposure time:

$$FeO_2\ percentage = 0.006t^2 - 0.153t + 1.000$$

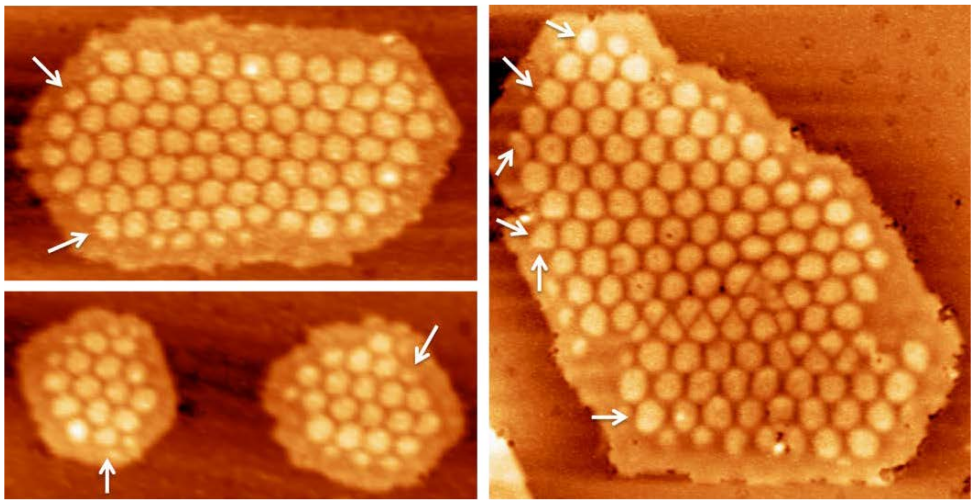

Figure 4-14. High resolution STM images of partially reduced FeO_{2-x} islands. Tunneling conditions: -3V, 0.05nA.

A closer examining on higher resolution images in **Figure4-14** shows that O Moiré spots-like domains' shrink from the outer boundary of FeO_2/FeO similarly to that observed on closed films at mbar pressures by Lewandowski[154]. Although the detailed mechanism is still not clear, it's obviously that the reaction front velocity depends on many parameters such as edge orientation and even island size. Although precise relationships are difficult to establish, the kinetics of parabolic decay fit of FeO_2 reduction in is characteristic for decay of two-dimensional islands involving bond-breaking at the edge sites, as observed, for example, for graphene etching in hydrogen atmosphere, and can be explained by the model of a detachment-limited etching process following first-order kinetics: [239-240]

$$\frac{\mathrm{dr}}{\mathrm{dt}} = constant$$

With r is the radial length of top layer O area.

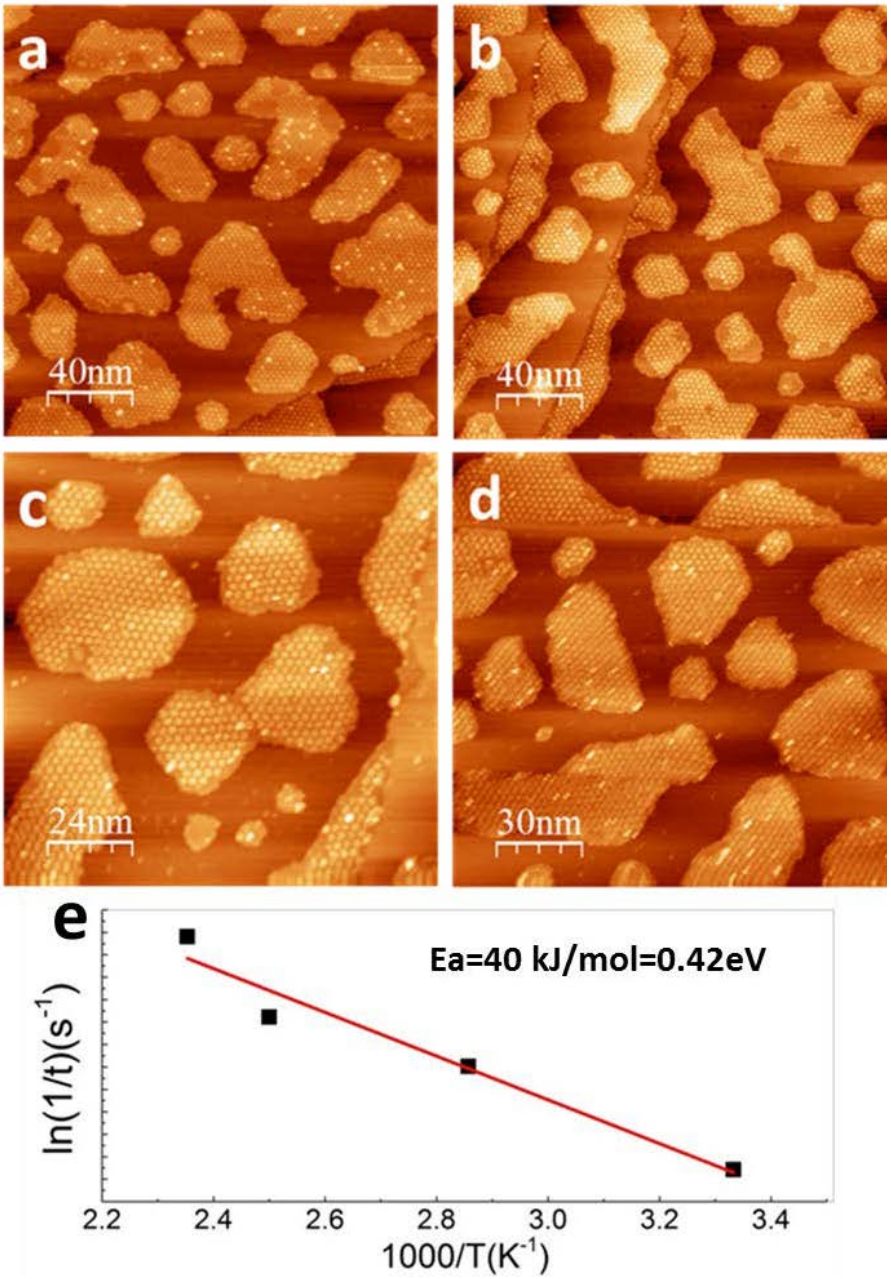

Figure 4-15. STM images of the first circle of Moiré like O domain at islands edge reacting in $1x10^{-6}$ mbar CO with temperatures and time of 425K,1min(a), 400K, 6min(b), 350K, 18min(c), 300K, 65min(d). (e) Arrhenius plot for the reaction rate(1/t) signal as a function of reaction temperature. Tunneling conditions: (a-d) -3V, 0.1nA.

The experiments were performed at different temperatures between 300 and 450 K. The reaction slows down at low temperatures as demonstrated by STM image **Figure4-15(a-d)**: morphology after reaction for 1 min at 425 K (**Figure4-15a**) is

equivalent to to that for 6 min at 400 K **(Figure4-15b)**. Because the complete transformation at low temperatures requires too much time, as a crude approximation, we used the reacting time it takes to remove the Moiré spots like O domains at the edges to estimate the reaction rate. The reaction at 450 K was found too fast to determine the decay time precisely. Assuming that the CO reaction with O in oxide follows an Arrhenius-type behavior, the plot shown in **Figure4-15e** yields ~40 kJ/mol for the apparent activation energy. This value is substantially smaller than ~ 115 kJ/mol reported for CO oxidation on dense films in the mixture of 10 mbar CO and 20 mbar O_2 at 410-450 K, which indicates that it is likely the replenishment of oxygen atoms reacted with CO that is the rate-limiting step in the CO oxidation reaction at steady state.

We could not achieve high resolution with our apparatus to address the atomic structure. However, the STM images displayed show that the Moiré spots like O domains disappear not uniformly, but from the side that is closer to the island edge. Apparently, the FeO_2 spots in the interior region remain unperturbed. This finding indicates that, under low pressure conditions used, the reaction does not occur on the "intrinsic" FeO/FeO_2 interface within the FeO_2 structure, which otherwise should result in uniform and homogeneous shrinking of the FeO_2 spots throughout the entire island surface. The results show that oxide reduction by CO primarily takes place at the interface between the compact FeO_2 surface and the reduced FeO(111)-like surface formed by reaction with CO, which is quite different with the "intrinsic" FeO phase at the O domains' interface.

Observation of Lewandowski et al [154] on closed FeO_2 films at the mbar pressure CO indicates the top layer O vacancy defects ignite the reduction process. Although these defects are still poorly defined, corresponding enlarged holes undergoing reaction with CO also present FeO-like phase on the bottom. In the case of partially covered films, the reaction is definitely initiated at the island edges. It appears that such sites ignite the reduction process in CO ambient, which then propagates across the surface leaving the FeO-like surface behind. In principle, this would be consistent with the DFT predictions[217], which shows the lowest O vacancy formation energy (1.31 eV) belong to the oxygen atoms at the FeO_2/FeO interface, although the value was calculated for the case of "intrinsic" FeO/FeO_2. The respective energies for interfacial oxygen atoms at FeO_2/Pt are 1.58 and 1.53 eV, i.e. considerably lower than for topmost oxygen in FeO_2 trilayer (1.67 eV), and all these are more weakly bound than on the FeO/Pt interface (2.15 eV). This means that once the O vacancy is formed on FeO_2 surface, the ambient CO will preferentially react with the surrounding O on FeO_2, which induced the expansion of this vacancy. However, oxygen extraction characteristics are quite sensitive to the oxide coverage and the local structure of the FeO_x/Pt interface that, in turn, depends on the oxide/metal registry within the Moiré cell. Nonetheless, our STM results clearly show that CO first reacts at FeO_2 /Pt interface due to its strong adsorption on Pt(111) providing large residence time to react.

Based on results and analysis upwards, a proposed scenario is schematically showed in **Figure 4-16**. For simplicity, the edge solely exposes FeO_2/Pt. First, CO adsorbed on Pt reacts with the O atom at the island edge (the binding energy 1.67 eV) and the produced CO_2 desorbs immediately. The Fe atoms around the O vacancy relax and strongly bind to Pt, thus forming locally a FeO-like bilayer structure. Further CO reaction with this site is hardly possible as it requires about 2.15 eV to extract oxygen from FeO/Pt, thus the reaction pathway involving CO on Pt is self-terminated. However, CO can readily react with newly formed FeO/FeO_2 interface created in the first step, as the oxygen extraction from the latter costs only 1.31 eV. In principle, CO may either react directly with this weakly bonded O atom via Eley-Riedel type mechanism or adsorb on a neighboring low-coordinated Fe atom via Langmuir-Hinshelwood mechanism. In any case, this process repeats itself and the interface spatially shifts towards the O-rich phase in the interior region such that the reaction propagates like a wave. In principle, the proposed scenario can be adopted for other possible FeO_x/Pt structures at the island edge in the oxidized films. Also, in the initial stages the reaction may propagate along the island edge via the same mechanism, ultimately consuming the O domains at the edges as observed by STM. It is important to note, that although the O-depleted areas left behind the reaction front showed STM fingerprints of well-ordered FeO(111), its atomic structure and hence interface to the "compact" FeO_2 domains remaining in the interior region seems to considerably differ in reactivity as compared to the "intrinsic" FeO/ FeO_2 interface in the pristine FeO_2 films. Therefore, the interface between initially present "O-rich" FeO_2 structure and "O-poor" structure formed upon reduction may become highly reactive towards CO oxidation.

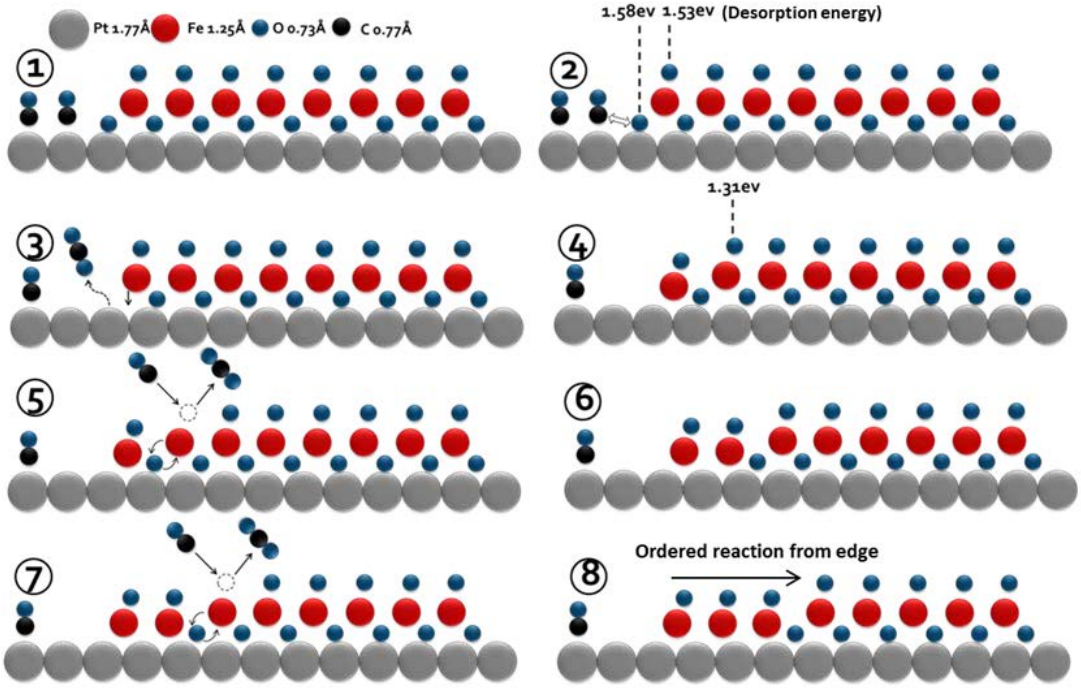

Figure 4-16. Proposed scenario of CO reaction with FeO_2/Pt(111) island: ① initial state of the

system with FeO_2 island and CO adsorbed on Pt; ② adsorbed CO reacts with O at the bottom of the island edge ; ③ Produced CO_2 desorbs and the edge Fe atom relaxes down to bind with Pt support and ④ form the first FeO-like structure; ⑤ O at FeO/FeO_2 edge reacts with CO to produce CO_2, the left Fe-O pair relaxes and flips to form normal FeO/Pt(111) configuration; ⑥-⑧ Repeated ④-⑤ process with ambient CO reacting with O at FeO/FeO_2 interface and Fe-O pair flipping.

4.3.4. Reaction in the CO and O_2 mixture

To examine the above-mentioned possibility, we exposed FeO_2 samples to CO and O_2 mixture with different ratios at 450K for 6min. The STM images are presented in **Figure 4-17.**

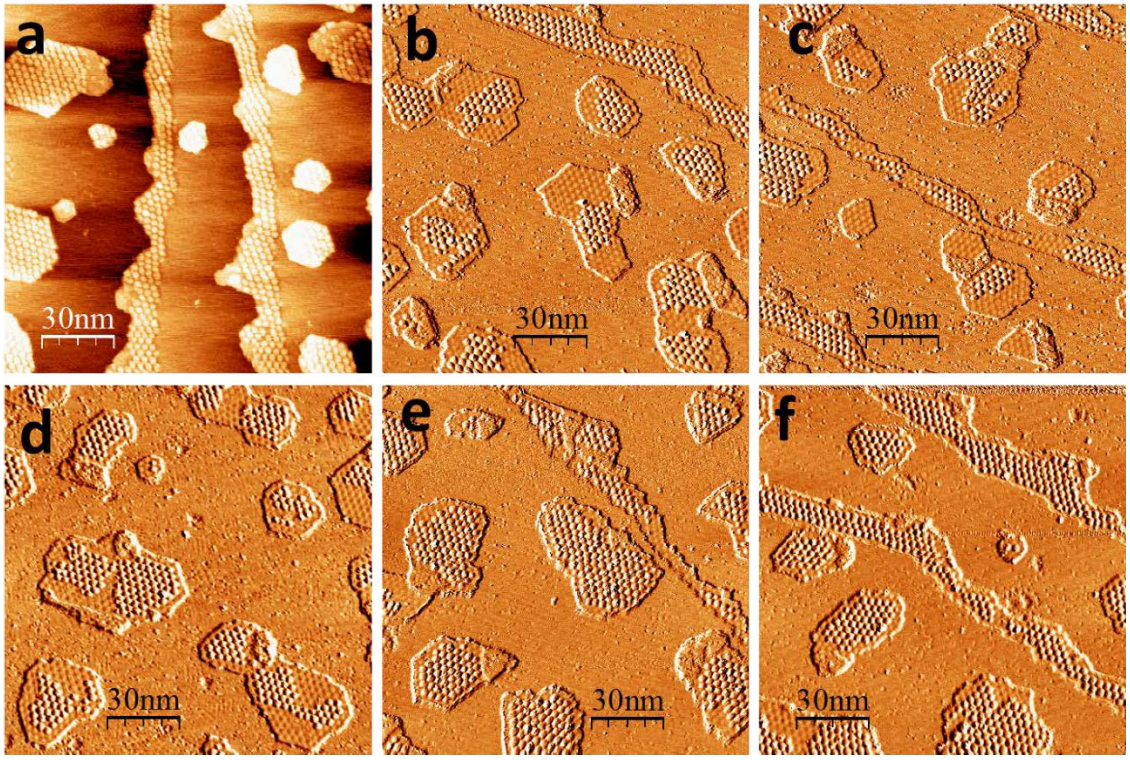

Figure 4-17. STM images of (a): fully oxidized FeO_2 sample; (b): fully oxidized FeO_2 sample exposed to $1x10^{-6}$mabr CO for 6min; (c): fully oxidized FeO_2 sample exposed to mixture of $5x10^{-7}$mabr O_2 and $1x10^{-6}$mabr CO for 6min; (d): sample(c) exposed to mixture of $5x10^{-6}$mabr O_2 and $1x10^{-6}$mabr CO for 6min; (e): fully oxidized FeO_2 sample exposed to mixture of $5x10^{-6}$mabr O_2 and $1x10^{-6}$mabr CO for 6min; (f): fully oxidized FeO_2 sample exposed to mixture of $9x10^{-6}$mabr O_2 and $1x10^{-6}$mabr CO for 6min. Numbers attached are the corresponding left top layer oxygen percentage. (b-f) are current images. The tunneling conditions: (a) -2.3V, 1.9nA; (b-d)-2.1V, 1.9nA; (e,f)-3.0V, 1.9nA;

As comparison, surface morphology before and after exposure to pure CO for 6 min is shown in **Figure 4-17 a, b.** After surface re-oxidation and exposure in the

mixture with stoichiometric ratio (CO: O_2=2:1), the sample (**Figure 4-17 c**) exhibits virtually identical structure as in pure CO. Subsequent 6 min exposure to the O-rich mixture (CO: O_2=1:5) "freezes" the previous structure (**Figure 4-17 d**), which otherwise would completely be reduced in pure CO. However, direct exposure of this sample (after re-oxidation) to the O-rich mixture (CO: O_2= 1:5 and 1:9) still cannot stabilize the original structure close to the island edges, although the interior regions remain essentially intact (**Figure 4-17 e, f**).

Similarity of **Figure4-17b** and **c** indicates that the chemical potential of ambient O_2 is not high enough to replenish the top layer O on FeO_{2-x} consumed by CO. However, that oxygen suppresses oxide reduction by CO in the O-rich atmosphere, it's a rational interpretation that under high O chemical potential, the top layer O can be replenished and finished the catalytic cycle to produce CO_2 without the further consumption of top layer O on FeO_{2-x} island as shown in **Figure 4-18 c**.

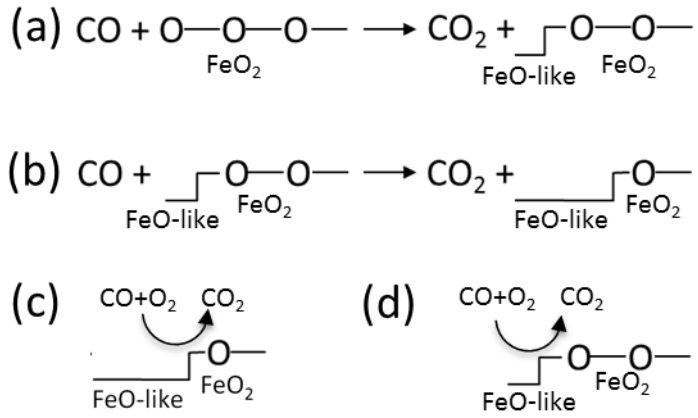

Figure 4-18. Schematic representation of the FeO_2 island in pure CO and $CO+O_2$ ambient.

Small consumption of top layer O at the edge of the islands after exposure in O-rich mixtures confirms the stability of the top layer O at the island interior in O-rich mixture as depicted in **Figure 4-18d.** Replenishment of top layer O in O-rich atmosphere implies the FeO/FeO_2 boundary is active site where the CO oxidation finishes the catalytic cycle. DFT calculation to oxygen trapping and extraction characteristics at a large variety of sites in sub-monolayer FeO_{2-x} indicates that moderate oxygen storage/release ability at FeO/FeO_2 boundary makes it possible to act as active site[238]. In contrast, the easiest to reduce at FeO_2/Pt boundary also implies it's difficult to oxidize back as shown in **Figure4-17e f.**

4.3.5. Next step

There still many questions remain for the ultrathin FeO at the standing point, such as: 1). Where's the active site for CO oxidation? 2). What's the mechanism of

edge effect for CO oxidation on FeO/Pt(111)? 3). What's the structure of FeO_{1+x} (oxidized FeO) on Au(111)? Therefore, the next studies may include:

1. To measure CO oxidation rate in 10^{-6} mbar range to combine with above shown STM results.
2. Using probe molecules which do not adsorb on Pt surface at room temperature to exclude the residence time factor of CO oxidation on sub-monolayer FeO/Pt.
3. DFT studies may greatly contribute to elucidate the reaction mechanism, in particular to shed light on the structure of oxidized FeO on Au(111)
4. Based on the preliminary STM result of partially reduced FeO_{1+x}/Au(111) as shown in **Figure 4-19,** reduction of FeO_{1+x}/Au(111) shows an opposite behavior: Oxygen desorption seems to start in the interior area leaving edge sites O-rich. This, again, suggests an important role of a metal substrate in the stabilization and reduction of iron oxide ultrathin layer.

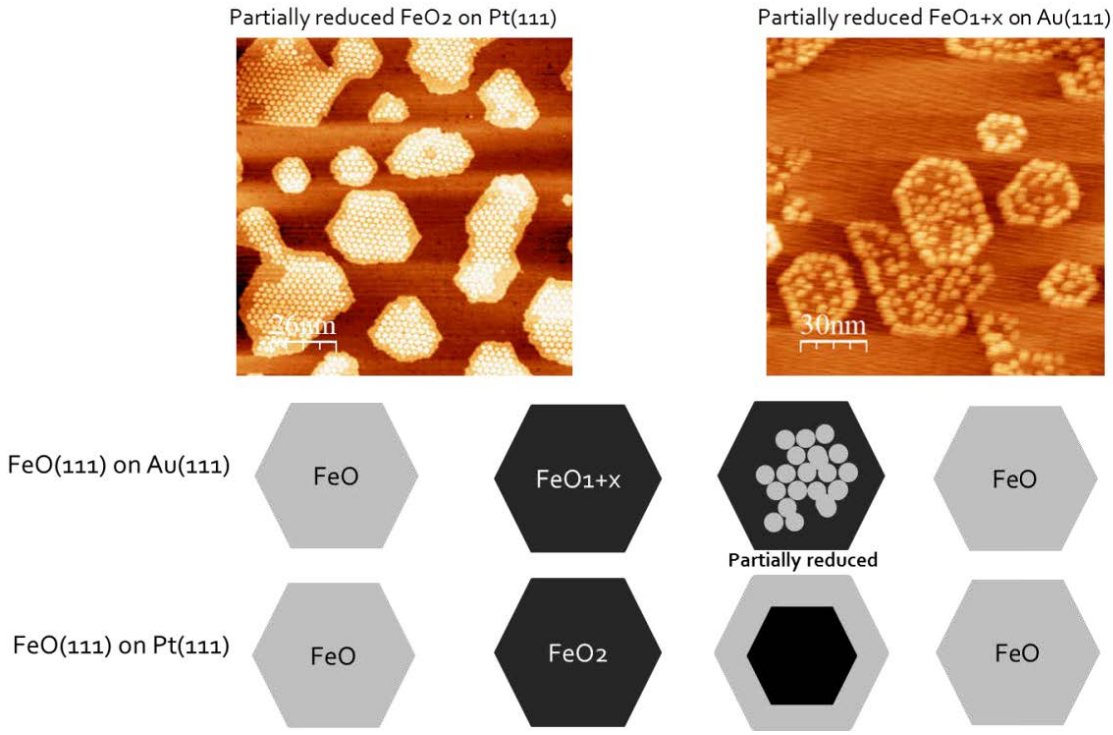

Figure 4-19. Partially reduced FeO_2/Pt(111) and FeO_{1+x}/Au(111) (up). Schematic drawing of FeO oxidation-reduction process on Pt(111) and Au(111) (bottom).

Summary

In the first part of the Thesis, we studied SMSI effects for Pt and Pd deposited onto Fe_3O_4 thin film supports. The main observations can be summarized as follows:

1. At low and medium coverages, Pt and Pd preferentially adsorbs monoatomically on the so-called "narrow" sites of $Fe_3O_4(001)$-$(\sqrt{2} \times \sqrt{2})R45°$ surface. Vacuum annealing above 700 K leads to Pt sintering and concomitantly to particle reshaping into cuboid Pt nanoparticles at about 1000 K with the edges oriented along the crystallographic directions of the $Fe_3O_4(001)$ surface.

2. High-temperature UHV annealing suppresses CO uptake on Pt and Pd, thus manifesting a SMSI effect via metal encapsulation by the support. For Pt/$Fe_3O_4(001)$ system, the combined LEED, STM, and TPD results provide strong evidence for the encapsulating overlayer to be identified as FeO(111).

3. The comparison of the Pt/$Fe_3O_4(001)$ and Pt/$Fe_3O_4(111)$ systems suggests that the SMSI effect is insensitive to the particular surface structure of the oxide.

4. Apparently, encapsulation and metal sintering (presumably via Ostwald ripening), both occurring at elevated temperatures, defines the particle's size and morphology, as encapsulation blocks metal ripening. Due to the relatively weaker adsorption energy of Pd than of Pt on iron oxide, Pd sintering takes place at lower temperature and thus results in larger particles as compared to Pt.

In the second part of the Thesis, the structure and reactivity of ultra-thin FeO(111) films supported by Pt(111) and Au(111) were studied. The results are summarized as follows:

1. Sub-monolayer FeO(111) on Au(111) transform into an O-rich phase FeO_{1+x} in 10 mbar O_2 at 470K. However, the oxygen enrichment measured is remarkably lower as compared to FeO_2/Pt(111) system, although he lattice constant of resultant FeO_{1+x}/Au(111) decreases from 3.20 to 3.05 Å, Oxidation of the dense film causes severe reconstruction. Due to weak interaction with underlying Au support, phase transformations on Au are most likely determined by stability of iron oxide phase, whereas a Pt support is deeply involved in stabilization mechanism.

2. Sub-monolayer FeO/Pt(111) can be oxidized to FeO_2 in $5x10^{-6}$mbar O_2 at 570K.

3. TPD and STM results on O-rich FeO_2 islands show that oxygen thermal desorption is accompanied by FeO_2 transformation into FeO that propagates

from the islands edge towards the interior part., This finding is indicative of the lower binding energy of O at FeO_2/Pt and also FeO_2/FeO interface.

4. Similarly, FeO_2 to FeO transformation occurs in 10^{-6} mbar CO ambient at low temperatures, again from island edge to interior. Temperature dependence of this reaction at 425-300K suggests the activation energy of ~40 kJ/mol.

5. STM study on FeO_2 island in CO/O_2 mixture suggests the FeO/FeO_2 interface sites as the active site for CO oxidation.

References

1. I. Chorkendorff, J. W. N., *Concepts of Modern Catalysis And Kinetics, Second Edition*. 2 Ed.; Wiley-Vch Verlag Gmbh & Co. Kgaa: **2007**.
2. Tauster, S. J.; Fung, S. C.; Garten, R. L., Strong Metal-Support Interactions - Group-8 Noble-Metals Supported On TiO2. *Journal of The American Chemical Society* **1978,** *100* (1), 170-175.
3. Navrotsky, A.; Ma, C. C.; Lilova, K.; Birkner, N., Nanophase Transition Metal Oxides Show Large Thermodynamically Driven Shifts In Oxidation-Reduction Equilibria. *Science* **2010,** *330* (6001), 199-201.
4. Kinloch, A. J., *Adhesion And Adhesives: Science And Technology*. Chapman & Hall: London, 1987.
5. Schwab, G. M.; Schultes, H., Modes of Action From Catalytic Mixes During Breakup of The Nitrogein Oxidules. *Zeitschrift Fur Physikalische Chemie-Abteilung B-Chemie Der Elementarprozesse Aufbau Der Materie* **1930,** *9* (4/5), 265-288.
6. Bernal, S.; Botana, F. J.; Calvino, J. J.; Cifredo, G. A.; Perezomil, J. A., Hrem Study of The Behavior of A Rh/Ceo2 Catalyst Under High-Temperature Reducing And Oxidizing Conditions. *Catalysis Today* **1995,** *23* (3), 219-250.
7. Bernal, S.; Cauqui, M. A.; Cifredo, G. A.; Gatica, J. M.; Larese, C.; Omil, J. A. P., Chemical And Microstructural Investigation of Pt/CeO2 Catalysts Reduced At Temperatures Ranging From 473 to 973 K. *Catalysis Today* **1996,** *29* (1-4), 77-81.
8. Kepinski, L.; Wolcyrz, M., Microstructure of Pd/CeO2 Catalyst: Effect of High Temperature Reduction In Hydrogen. *Applied Catalysis A-General* **1997,** *150* (2), 197-220.
9. Bernal, S.; Calvino, J. J.; Cauqui, M. A.; Omil, J. A. P.; Pintado, J. M.; Rodriguez-Izquierdo, J. M., Image Simulation And Experimental Hrem Study of The Metal Dispersion In Rh/CeO2 Catalysts. Influence of The Reduction/Reoxidation Conditions. *Applied Catalysis B-Environmental* **1998,** *16* (2), 127-138.
10. Bernal, S.; Calvino, J. J.; Cauqui, M. A.; Gatica, J. M.; Larese, C.; Omil, J. A. P.; Pintado, J. M., Some Recent Results On Metal/Support Interaction Effects In NM/CeO2 (NM : Noble Metal) Catalysts. *Catalysis Today* **1999,** *50* (2), 175-206.
11. Bera, P.; Patil, K. C.; Jayaram, V.; Subbanna, G. N.; Hegde, M. S., Ionic Dispersion of Pt And Pd On CeO2 By Combustion Method: Effect of Metal-Ceria Interaction On Catalytic Activities For NO Reduction And CO And Hydrocarbon Oxidation. *Journal of Catalysis* **2000,** *196* (2), 293-301.
12. Ayastuy, J. L.; Gil-Rodriguez, A.; Gonzalez-Marcos, M. P.; Gutierrez-Ortiz, M. A., Effect of Process Variables On Pt/CeO2 Catalyst Behaviour For The Prox Reaction. *International Journal of Hydrogen Energy* **2006,** *31* (15), 2231-2242.
13. Ferreira, A. P.; Zanchet, D.; Araujo, J. C. S.; Liberatori, J. W. C.; Souza-Aguiar, E. F.; Noronha, F. B.; Bueno, J. M. C., The Effects of CeO2 On The Activity And Stability of Pt Supported Catalysts For Methane Reforming, As Addressed By In Situ Temperature Resolved Xafs And Tem Analysis. *Journal of Catalysis* **2009,** *263* (2), 335-344.
14. Ou, D. R.; Mori, T.; Togasaki, H.; Takahashi, M.; Ye, F.; Drennan, J., Microstructural And Metal-Support Interactions of The Pt-CeO2/C Catalysts For Direct Methanol Fuel Cell Application. *Langmuir* **2011,** *27* (7), 3859-3866.
15. Bruix, A.; Rodriguez, J. A.; Ramirez, P. J.; Senanayake, S. D.; Evans, J.; Park, J. B.; Stacchiola, D.; Liu, P.; Hrbek, J.; Illas, F., A New Type of Strong Metal-Support Interaction And The Production of H-2

Through The Transformation of Water On Pt/CeO2(111) And Pt/CeOx/TiO2(110) Catalysts. *Journal of The American Chemical Society* **2012,** *134* (21), 8968-8974.

16. Carrasco, J.; Barrio, L.; Liu, P.; Rodriguez, J. A.; Ganduglia-Pirovano, M. V., Theoretical Studies of The Adsorption of Co And C On Ni(111) And Ni/CeO2(111): Evidence of A Strong Metal-Support Interaction. *Journal of Physical Chemistry C* **2013,** *117* (16), 8241-8250.
17. Tereshchuk, P.; Freire, R. L. H.; Ungureanu, C. G.; Seminovski, Y.; Kiejna, A.; Da Silva, J. L. F., The Role of Charge Transfer In The Oxidation State Change of Ce Atoms In The TM13-CeO2(111) Systems (TM = Pd, Ag, Pt, Au): A Dft Plus U Investigation. *Phys Chem Chem Phys* **2015,** *17* (20), 13520-13530.
18. Carrasco, J.; Lopez-Duran, D.; Liu, Z. Y.; Duchon, T.; Evans, J.; Senanayake, S. D.; Crumlin, E. J.; Matolin, V.; Rodriguez, J. A.; Ganduglia-Pirovano, M. V., In Situ And Theoretical Studies For The Dissociation of Water On An Active Ni/CeO2 Catalyst: Importance of Strong Metal-Support Interactions For The Cleavage of O-H Bonds. *Angewandte Chemie-International Edition* **2015,** *54* (13), 3917-3921.
19. Wang, Z. H.; Fu, H. F.; Tian, Z. W.; Han, D. M.; Gu, F. B., Strong Metal-Support Interaction In Novel Core-Shell Au-CeO2 Nanostructures Induced By Different Pretreatment Atmospheres And Its Influence On Co Oxidation. *Nanoscale* **2016,** *8* (11), 5865-5872.
20. Qin, Z. H.; Lewandowski, M.; Sun, Y. N.; Shaikhutdinov, S.; Freund, H. J., Encapsulation of Pt Nanoparticles As A Result of Strong Metal-Support Interaction With Fe(3)O(4) (111). *Journal of Physical Chemistry C* **2008,** *112* (27), 10209-10213.
21. Sun, Y. N.; Qin, Z. H.; Lewandowski, M.; Kaya, S.; Shaikhutdinov, S.; Freund, H. J., When An Encapsulating Oxide Layer Promotes Reaction On Noble Metals: Dewetting And In Situ Formation of An "Inverted" FeOx/Pt Catalyst. *Catalysis Letters* **2008,** *126* (1-2), 31-35.
22. Lewandowski, M.; Sun, Y. N.; Qin, Z. H.; Shaikhutdinov, S.; Freund, H. J., Promotional Effect of Metal Encapsulation On Reactivity of Iron Oxide Supported Pt Catalysts. *Applied Catalysis A-General* **2011,** *391* (1-2), 407-410.
23. Zhang, K.; Shaikhutdinov, S.; Freund, H. J., Does The Surface Structure of Oxide Affect The Strong Metal-Support Interaction With Platinum? Platinum On Fe_3O_4(001) Versus Fe_3O_4(111). *Chemcatchem* **2015,** *7* (22), 3725-3730.
24. Willinger, M. G.; Zhang, W.; Bondarchuk, O.; Shaikhutdinov, S.; Freund, H. J.; Schlogl, R., A Case of Strong Metal-Support Interactions: Combining Advanced Microscopy And Model Systems To Elucidate The Atomic Structure of Interfaces. *Angewandte Chemie-International Edition* **2014,** *53* (23), 5998-6001.
25. Qin, Z. H.; Lewandowski, M.; Sun, Y. N.; Shaikhutdinov, S.; Freund, H. J., Morphology And Co Adsorption On Platinum Supported On Thin Fe_3O_4(111) Films. *J Phys-Condens Mat* **2009,** *21* (13).
26. Sankar, G.; Vasudevan, S.; Rao, C. N. R., Strong Metal-Support Interaction In Ni/Nb2O5 And Ni/TiO2 Catalysts. *J Phys Chem-Us* **1988,** *92* (7), 1878-1882.
27. Dulub, O.; Hebenstreit, W.; Diebold, U., Imaging Cluster Surfaces With Atomic Resolution: The Strong Metal-Support Interaction State of Pt Supported On TiO2(110). *Phys Rev Lett* **2000,** *84* (16), 3646-3649.
28. Bernal, S.; Calvino, J. J.; Cauqui, M. A.; Gatica, J. M.; Cartes, C. L.; Omil, J. A. P.; Pintado, J. M., Some Contributions of Electron Microscopy To The Characterisation of The Strong Metal-Support Interaction Effect. *Catalysis Today* **2003,** *77* (4), 385-406.
29. Diebold, U., The Surface Science of Titanium Dioxide. *Surface Science Reports* **2003,** *48* (5-8), 53-229.
30. Bowker, M.; Stone, P.; Morrall, P.; Smith, R.; Bennett, R.; Perkins, N.; Kvon, R.; Pang, C.; Fourre, E.; Hall,

M., Model Catalyst Studies of The Strong Metal-Support Interaction: Surface Structure Identified By Stm On Pd Nanoparticles On TiO2(110). *Journal of Catalysis* **2005,** *234* (1), 172-181.

31. Fu, Q.; Wagner, T., Interaction of Nanostructured Metal Overlayers With Oxide Surfaces. *Surface Science Reports* **2007,** *62* (11), 431-498.
32. Weerachawanasak, P.; Mekasuwandumrong, O.; Arai, M.; Fujita, S. I.; Praserthdam, P.; Panpranot, J., Effect of Strong Metal-Support Interaction On The Catalytic Performance of Pd/TiO2 In The Liquid-Phase Semi Hydrogenation of Phenylacetylene. *Journal of Catalysis* **2009,** *262* (2), 199-205.
33. Singh, C. A.; Bansal, L.; Tiwari, P.; Krishnan, V. V., Strong Metal Support Interactions of Infiltrated Ni With TiO2 In A Porous YSZ Anode Matrix - A Possible Method For Ni-Stabilization. *ECS Transactions*. **2009**, 25 (2), 1897-1904
34. Park, J. B.; Graciani, J.; Evans, J.; Stacchiola, D.; Senanayake, S. D.; Barrio, L.; Liu, P.; Sanz, J. F.; Hrbek, J.; Rodriguez, J. A., Gold, Copper, And Platinum Nanoparticles Dispersed On CeOx/TiO2(110) Surfaces: High Water-Gas Shift Activity And The Nature of The Mixed-Metal Oxide At The Nanometer Level. *Journal of The American Chemical Society* **2010,** *132* (1), 356-363.
35. Zhu, X.; Shen, M.; Lobban, L. L.; Mallinson, R. G., Structural Effects of Na Promotion For High Water Gas Shift Activity On Pt-Na/TiO2. *Journal of Catalysis* **2011,** *278* (1), 123-132.
36. Colmenares, J. C.; Magdziarz, A.; Aramendia, M. A.; Marinas, A.; Marinas, J. M.; Urbano, F. J.; Navio, J. A., Influence of The Strong Metal Support Interaction Effect (SMSI) of Pt/TiO2 And Pd/TiO2 Systems In The Photocatalytic Biohydrogen Production From Glucose Solution. *Catalysis Communications* **2011,** *16* (1), 1-6.
37. Bonanni, S.; Ait-Mansour, K.; Brune, H.; Harbich, W., Overcoming The Strong Metal-Support Interaction State: Co Oxidation On TiO(2)(110)-Supported Pt Nanoclusters. *Acs Catalysis* **2011,** *1* (4), 385-389.
38. Linsmeier, C.; Taglauer, E., Strong Metal-Support Interactions On Rhodium Model Catalysts. *Applied Catalysis A-General* **2011,** *391* (1-2), 175-186.
39. Bonanni, S.; Ait-Mansour, K.; Harbich, W.; Brune, H., Effect of The TiO2 Reduction State On The Catalytic Co Oxidation On Deposited Size-Selected Pt Clusters. *Journal of The American Chemical Society* **2012,** *134* (7), 3445-3450.
40. Baker, L. R.; Kennedy, G.; Van Spronsen, M.; Hervier, A.; Cai, X. J.; Chen, S. Y.; Wang, L. W.; Somorjai, G. A., Furfuraldehyde Hydrogenation On Titanium Oxide-Supported Platinum Nanoparticles Studied By Sum Frequency Generation Vibrational Spectroscopy: Acid-Base Catalysis Explains The Molecular Origin of Strong Metal-Support Interactions. *Journal of The American Chemical Society* **2012,** *134* (34), 14208-14216.
41. Zhang, J. W.; Zhang, M.; Jin, Z. S.; Wang, J. J.; Zhang, Z. J., Study of High-Temperature Hydrogen Reduced Pt-0/TiO2 By X-Ray Photoelectron Spectroscopy Combined With Argon Ion Sputtering-Diffusion-Encapsulation Effect In Relation To Strong Metal-Support Interaction. *Appl Surf Sci* **2012,** *258* (8), 3991-3999.
42. Kim, M. S.; Chung, S. H.; Yoo, C. J.; Lee, M. S.; Cho, I. H.; Lee, D. W.; Lee, K. Y., Catalytic Reduction of Nitrate In Water Over Pd-Cu/TiO2 Catalyst: Effect of The Strong Metal-Support Interaction (Smsi) On The Catalytic Activity. *Applied Catalysis B-Environmental* **2013,** *142*, 354-361.
43. Tiwari, P.; Basu, S., Ni Infiltrated YSZ Anode Stabilization By Inducing Strong Metal Support Interaction Between Nickel And Titania In Solid Oxide Fuel Cell Under Accelerated Testing. *International Journal of Hydrogen Energy* **2013,** *38* (22), 9494-9499.

44. An, K.; Zhang, Q.; Alayoglu, S.; Musselwhite, N.; Shin, J.-Y.; Somorjai, G. A., High-Temperature Catalytic Reforming of N-Hexane Over Supported And Core-Shell Pt Nanoparticle Catalysts: Role of Oxide-Metal Interface And Thermal Stability. *Nano Letters* **2014,** *14* (8), 4907-4912.
45. Bowker, M.; Sharpe, R., Pd Deposition On TiO2(110) And Nanoparticle Encapsulation. *Catalysis, Structure & Reactivity* **2015,** 1(3), 140-145.
46. Rui, Z. B.; Chen, L. Y.; Chen, H. Y.; Ji, H. B., Strong Metal-Support Interaction In Pt/TiO2 Induced By Mild Hcho And Nabh4 Solution Reduction And Its Effect On Catalytic Toluene Combustion. *Industrial & Engineering Chemistry Research* **2014,** *53* (41), 15879-15888.
47. Wang, L.; Wang, H.; Rice, A. E.; Zhang, W.; Li, X.; Chen, M.; Meng, X.; Lewis, J. P.; Xiao, F.-S., Design And Preparation of Supported Au Catalyst With Enhanced Catalytic Activities By Rationally Positioning Au Nanoparticles On Anatase. *Journal of Physical Chemistry Letters* **2015,** *6* (12), 2345-2349.
48. Lee, J.; Burt, S. P.; Carrero, C. A.; Alba-Rubio, A. C.; Ro, I.; O'neill, B. J.; Kim, H. J.; Jackson, D. H. K.; Kuech, T. F.; Hermans, I.; Dumesic, J. A.; Huber, G. W., Stabilizing Cobalt Catalysts For Aqueous-Phase Reactions By Strong Metal-Support Interaction. *Journal of Catalysis* **2015,** *330*, 19-27.
49. Kovtunov, K. V.; Barskiy, D. A.; Salnikov, O. G.; Burueva, D. B.; Khudorozhkov, A. K.; Bukhtiyarov, A. V.; Prosvirin, I. P.; Gerasimov, E. Y.; Bukhtiyarov, V. I.; Koptyug, I. V., Strong Metal-Support Interactions For Palladium Supported On TiO2 Catalysts In The Heterogeneous Hydrogenation With Parahydrogen. *Chemcatchem* **2015,** *7* (17), 2581-2584.
50. Tang, H. L.; Liu, F.; Wei, J. K.; Qiao, B. T.; Zhao, K. F.; Su, Y.; Jin, C. Z.; Li, L.; Liu, J. Y.; Wang, J. H.; Zhang, T., Ultrastable Hydroxyapatite/Titanium-Dioxide-Supported Gold Nanocatalyst With Strong Metal-Support Interaction For Carbon Monoxide Oxidation. *Angewandte Chemie-International Edition* **2016,** *55* (36), 10606-10611.
51. Sterchele, S.; Bortolus, M.; Biasi, P.; Bostrom, D.; Mikkola, J. P.; Salmi, T., Is Selective Hydrogenation of Molecular Oxygen To H2o2 Affected By Strong Metal-Support Interactions On Pd/TiO2 Catalysts? A Case Study Using Commercially Available TiO2. *Comptes Rendus Chimie* **2016,** *19* (8), 1011-1020.
52. Zhang, S.; Plessow, P. N.; Willis, J. J.; Dai, S.; Xu, M. J.; Graham, G. W.; Cargnello, M.; Abild-Pedersen, F.; Pan, X. Q., Dynamical Observation And Detailed Description of Catalysts Under Strong Metal-Support Interaction. *Nano Letters* **2016,** *16* (7), 4528-4534.
53. Shi, X. Y.; Zhang, W.; Zhang, C.; Zheng, W. T.; Chen, H.; Qi, J. G., Real-Space Observation of Strong Metal-Support Interaction: State-of-The-Art And What's The Next. *Journal of Microscopy* **2016,** *262* (3), 203-215.
54. Jang, M. H.; Agarwal, R.; Nukala, P.; Choi, D.; Johnson, A. T. C.; Chen, I. W., Observing Oxygen Vacancy Driven Electroforming In Pt-TiO2-Pt Device Via Strong Metal Support Interaction. *Nano Letters* **2016,** *16* (4), 2139-2144.
55. Zhao, E. W.; Zheng, H. B.; Ludden, K.; Xin, Y.; Hagelin-Weaver, H. E.; Bowers, C. R., Strong Metal-Support Interactions Enhance The Pairwise Selectivity of Parahydrogen Addition Over Ir/TiO2. *Acs Catalysis* **2016,** *6* (2), 974-978.
56. Naldoni, A.; Riboni, F.; Marelli, M.; Bossola, F.; Ulisse, G.; Di Carlo, A.; Pis, I.; Nappini, S.; Malvestuto, M.; Dozzi, M. V.; Psaro, R.; Selli, E.; Dal Santo, V., Influence of TiO2 Electronic Structure And Strong Metal-Support Interaction On Plasmonic Au Photocatalytic Oxidations. *Catalysis Science & Technology* **2016,** *6* (9), 3220-3229.
57. Matsubu, J. C.; Zhang, S. Y.; Derita, L.; Marinkovic, N. S.; Chen, J. G. G.; Graham, G. W.; Pan, X. Q.; Christopher, P., Adsorbate-Mediated Strong Metal-Support Interactions In Oxide-Supported Rh

Catalysts. *Nature Chemistry* **2017,** *9* (2), 120-127.

58. Chen, P. R.; Khetan, A.; Yang, F. K.; Migunov, V.; Weide, P.; Sturmer, S. P.; Guo, P. H.; Kahler, K.; Xia, W.; Mayer, J.; Pitsch, H.; Simon, U.; Muhler, M., Experimental And Theoretical Understanding of Nitrogen-Doping-Induced Strong Metal-Support Interactions In Pd/TiO2 Catalysts For Nitrobenzene Hydrogenation. *Acs Catalysis* **2017,** *7* (2), 1197-1206.
59. Ito, S.; Chibana, C.; Nagashima, K.; Kameoka, S.; Tomishige, K.; Kunimori, K., CO Hydrogenation Over RhVO4/SiO2, Rh/V2O3 And Rh/SiO2 Catalysts: Reduction And Regeneration of RhVO4. *Applied Catalysis A-General* **2002,** *236* (1-2), 113-120.
60. Penner, S.; Stoeger-Pollach, M.; Thalinger, R., Metal-Support Interaction In Pt/Vox And Pd/Vox Systems: A Comparative (Hr)Tem Study. *Catalysis Letters* **2014,** *144* (1), 87-96.
61. Kunimori, K.; Ito, K.; Iwai, K.; Uchijima, T., Strong Metal-Support Interaction (Smsi) Behavior of Rh/Nb2O5 Catalyst Studied By Ethane Hydrogenolysis And Hydrogen Chemisorption. *Chemistry Letters* **1986,** (4), 573-576.
62. Silva, R.; Schmal, M.; Frety, R.; Dalmon, J. A., Effect of The Support On The Fischer-Tropsch Synthesis With Co/Nb2O5 Catalysts. *Journal of The Chemical Society-Faraday Transactions* **1993,** *89* (21), 3975-3980.
63. Brown, R.; Kemball, C., Influence of Strong Metal-Support Interaction On Exchange With Deuterium And Other Reactions of Hydrocarbons .2. Studies With Pt/Nb2O5 And Rh/Nh(2)O(5). *Journal of The Chemical Society-Faraday Transactions* **1996,** *92* (2), 281-288.
64. Ito, S.; Fujimori, T.; Nagashima, K.; Yuzaki, K.; Kunimori, K., Strong Rhodium-Niobia Interaction In Rh/Nb2O5, Nb2O5-Rh/SiO2 And Rhnbo4/SiO2 Catalysts - Application To Selective CO Oxidation And Co Hydrogenation. *Catalysis Today* **2000,** *57* (3-4), 247-254.
65. Damyanova, S.; Dimitrov, L.; Petrov, L.; Grange, P., Effect of Niobium On The Surface Properties of Nb2O5-SiO2-Supported Mo Catalysts. *Appl Surf Sci* **2003,** *214* (1-4), 68-74.
66. Jasik, A.; Wojcieszak, R.; Monteverdi, S.; Ziolek, M.; Bettahar, M. M., Study of Nickel Catalysts Supported On Al2o3, SiO2 Or Nb2O5 Oxides. *Journal of Molecular Catalysis A-Chemical* **2005,** *242* (1-2), 81-90.
67. Ahn, I. Y.; Kim, W. J.; Moon, S. H., Performance of La(2)O3- Or Nb2O5-Added Pd/SiO2 Catalysts In Acetylene Hydrogenation. *Applied Catalysis A-General* **2006,** *308*, 75-81.
68. Tamai, T.; Haneda, M.; Fujitani, T.; Hamada, H., Promotive Effect of Nb2O5 On The Catalytic Activity of Ir/SiO2 For No Reduction With Co Under Oxygen-Rich Conditions. *Catalysis Communications* **2007,** *8* (6), 885-888.
69. Rojas, H.; Borda, G.; Rosas, D.; Martinez, J. J.; Reyes, P., Hydrogenation of Furfural On Ir/Nb2O5 Catalyst Study Kinetic. *Dyna-Colombia* **2008,** *75* (155), 115-122.
70. Taglauer, E.; Knozinger, H., Characterization of Supported Catalyst Systems With Surface Spectroscopies. *Physica Status Solidi B-Basic Research* **1995,** *192* (2), 465-475.
71. Kalinkin, A. V.; Pashis, A. V., Studies of The Effect of Strong Metal-Support Interaction (Smsi) Over Model Catalyst Rh/TiO2. *Reaction Kinetics And Catalysis Letters* **1992,** *46* (1), 33-38.
72. Beard, B. C.; Ross, P. N., Pt-Ti Alloy Formation From High-Temperature Reduction of A Titania-Impregnated Pt Catalyst - Implications For Strong Metal Support Interaction. *J Phys Chem-Us* **1986,** *90* (26), 6811-6817.
73. Vandelft, F.; Nieuwenhuys, B. E., Correlation of Nucleation And Growth Modes With Wetting, Alloy Segregation, Catalyst Preparation And Strong-Metal Support Interaction. *Solid State Ionics* **1985,** *16*

(1-4), 233-240.

74. Praliaud, H.; Martin, G. A., Evidence of A Strong Metal-Support Interaction And of Ni-Si Alloy Formation In Silica-Supported Nickel-Catalysts. *Journal of Catalysis* **1981,** *72* (2), 394-396.
75. Fu, Q.; Yang, F.; Bao, X., Interface-Confined Oxide Nanostructures For Catalytic Oxidation Reactions. *Accounts of Chemical Research* **2013,** *46* (8), 1692-1701.
76. Solymosi, F.; Tombacz, I.; Kocsis, M., Hydrogenation of Co On Supported Rh Catalysts. *Journal of Catalysis* **1982,** *75* (1), 78-93.
77. Ishihara, T.; Harada, K.; Eguchi, K.; Arai, H., Electronic Interaction Between Supports And Ruthenium Catalysts For The Hydrogenation of Carbon-Monoxide. *Journal of Catalysis* **1992,** *136* (1), 161-169.
78. Haller, G. L., New Catalytic Concepts From New Materials: Understanding Catalysis From A Fundamental Perspective, Past, Present, And Future. *Journal of Catalysis* **2003,** *216* (1-2), 12-22.
79. Zhang, W.; Zheng, W. T., Transmission Electron Microscopy Finds Plenty of Room On The Surface. *Phys Chem Chem Phys* **2015,** *17* (22), 14461-14469.
80. Liu, J., Advanced Electron Microscopy of Metal-Support Interactions In Supported Metal Catalysts. *Chemcatchem* **2011,** *3* (6), 934-948.
81. Heggen, M.; Penner, S.; Friedrich, M.; Dunin-Borkowski, R. E.; Armbruster, M., Formation of Zno Patches On Znpd/Zno During Methanol Steam Reforming: A Strong Metal-Support Interaction Effect? *Journal of Physical Chemistry C* **2016,** *120* (19), 10460-10465.
82. Lunkenbein, T.; Schumann, J.; Behrens, M.; Schlogl, R.; Willinger, M. G., Formation of A Zno Overlayer In Industrial Cu/Zno/Al2o3 Catalysts Induced By Strong Metal-Support Interactions. *Angewandte Chemie-International Edition* **2015,** *54* (15), 4544-4548.
83. Schott, V.; Oberhofer, H.; Birkner, A.; Xu, M.; Wang, Y.; Muhler, M.; Reuter, K.; Woell, C., Chemical Activity of Thin Oxide Layers: Strong Interactions With The Support Yield A New Thin-Film Phase of ZnO. *Angewandte Chemie-International Edition* **2013,** *52* (45), 11925-11929.
84. Li, W.-Z.; Kovarik, L.; Mei, D.; Liu, J.; Wang, Y.; Peden, C. H. F., Stable Platinum Nanoparticles On Specific MgAl2O4 Spinel Facets At High Temperatures In Oxidizing Atmospheres. *Nature Communications* **2013,** *4*.
85. Liu, X. Y.; Liu, M. H.; Luo, Y. C.; Mou, C. Y.; Lin, S. D.; Cheng, H. K.; Chen, J. M.; Lee, J. F.; Lin, T. S., Strong Metal-Support Interactions Between Gold Nanoparticles And ZnO Nanorods In Co Oxidation. *Journal of The American Chemical Society* **2012,** *134* (24), 10251-10258.
86. Liu, Y.; Yao, W. Y.; Cao, X. L.; Weng, X. L.; Wang, Y.; Wang, H. Q.; Wu, Z. B., Supercritical Water Syntheses of CexTiO2 Nano-Catalysts With A Strong Metal-Support Interaction For Selective Catalytic Reduction of No With Nh3. *Applied Catalysis B-Environmental* **2014,** *160*, 684-691.
87. Mei, D.; Glezakou, V.-A.; Lebarbier, V.; Kovarik, L.; Wan, H.; Albrecht, K. O.; Gerber, M.; Rousseau, R.; Dagle, R. A., Highly Active And Stable MgAl2O4-Supported Rh And Ir Catalysts For Methane Steam Reforming: A Combined Experimental And Theoretical Study. *Journal of Catalysis* **2014,** *316*, 11-23.
88. Tang, H. L.; Wei, J. K.; Liu, F.; Qiao, B. T.; Pan, X. L.; Li, L.; Liu, J. Y.; Wang, J. H.; Zhang, T., Strong Metal-Support Interactions Between Gold Nanoparticles And Nonoxides. *Journal of The American Chemical Society* **2016,** *138* (1), 56-59.
89. Zhang, B.; Shao, L.; Zhang, W.; Sun, X.; Pan, X.; Su, D. S., Interaction Between Palladium Nanoparticles And Surface-Modified Carbon Nanotubes: Role of Surface Functionalities. *Chemcatchem* **2014,** *6* (9), 2607-2612.
90. Zhang, B.; Su, D. S., Transmission Electron Microscopy And The Science of Carbon Nanomaterials.

Small **2014,** *10* (2), 222-229.

91. Zhang, B.; Su, D. S., Probing The Metal-Support Interaction In Carbon-Supported Catalysts By Using Electron Microscopy. *Chemcatchem* **2015,** *7* (22), 3639-3645.
92. Zhang, W.; Kuhn, L. T., Strong Metal-Support Interaction: Growth of Individual Carbon Nanofibers From Amorphous Carbon Interacting With An Electron Beam. *Chemcatchem* **2013,** *5* (9), 2591-2594.
93. Kumar, A.; Ramani, V., Strong Metal Support Interactions Enhance The Activity And Durability of Platinum Supported On Tantalum-Modified Titanium Dioxide Electrocatalysts. *Acs Catalysis* **2014,** *4* (5), 1516-1525.
94. Neagu, D.; Oh, T.-S.; Miller, D. N.; Menard, H.; Bukhari, S. M.; Gamble, S. R.; Gorte, R. J.; Vohs, J. M.; Irvine, J. T. S., Nano-Socketed Nickel Particles With Enhanced Coking Resistance Grown In Situ By Redox Exsolution. *Nature Communications* **2015,** *6*.
95. Schumann, J.; Eichelbaum, M.; Lunkenbein, T.; Thomas, N.; Galvan, M. C. A.; Schlogl, R.; Behrens, M., Promoting Strong Metal Support Interaction: Doping ZnO For Enhanced Activity of Cu/ZnO:M (M = Al, Ga, Mg) Catalysts. *Acs Catalysis* **2015,** *5* (6), 3260-3270.
96. Zhang, C.; Liu, F.; Zhai, Y.; Ariga, H.; Yi, N.; Liu, Y.; Asakura, K.; Flytzani-Stephanopoulos, M.; He, H., Alkali-Metal-Promoted Pt/TiO2 Opens A More Efficient Pathway To Formaldehyde Oxidation At Ambient Temperatures. *Angewandte Chemie-International Edition* **2012,** *51* (38), 9628-9632.
97. Suzuki, T.; Souda, R., The Encapsulation of Pd By The Supporting TiO2(110) Surface Induced By Strong Metal-Support Interactions. *Surf Sci* **2000,** *448* (1), 33-39.
98. Huang, H. B.; Leung, D. Y. C.; Ye, D. Q., Effect of Reduction Treatment On Structural Properties of TiO2 Supported Pt Nanoparticles And Their Catalytic Activity For Formaldehyde Oxidation. *Journal of Materials Chemistry* **2011,** *21* (26), 9647-9652.
99. Mcentee, M.; Stevanovic, A.; Tang, W. J.; Neurock, M.; Yates, J. T., Electric Field Changes On Au Nanoparticles On Semiconductor Supports - The Molecular Voltmeter And Other Methods To Observe Adsorbate-Induced Charge-Transfer Effects In Au/TiO2 Nanocatalysts. *Journal of The American Chemical Society* **2015,** *137* (5), 1972-1982.
100. Behrens, M.; Studt, F.; Kasatkin, I.; Kuehl, S.; Haevecker, M.; Abild-Pedersen, F.; Zander, S.; Girgsdies, F.; Kurr, P.; Kniep, B.-L.; Tovar, M.; Fischer, R. W.; Norskov, J. K.; Schloegl, R., The Active Site of Methanol Synthesis Over Cu/ZnO/Al2O3 Industrial Catalysts. *Science* **2012,** *336* (6083), 893-897.
101. Galloway, H. C.; Sautet, P.; Salmeron, M., Structure And Contrast In Scanning Tunneling Microscopy of Oxides: Feo Monolayer On Pt(111). *Phys Rev B* **1996,** *54* (16), 11145-11148.
102. Ritter, M.; Ranke, W.; Weiss, W., Growth And Structure of Ultrathin Feo Films On Pt(111) Studied By Stm And Leed. *Phys Rev B* **1998,** *57* (12), 7240-7251.
103. Tauster, S. J., Strong Metal-Support Interactions. *Accounts of Chemical Research* **1987,** *20* (11), 389-394.
104. Zhu, X.; Hoang, T.; Lobban, L. L.; Mallinson, R. G., Significant Improvement In Activity And Stability of Pt/TiO2 Catalyst For Water Gas Shift Reaction Via Controlling The Amount of Na Addition. *Catalysis Letters* **2009,** *129* (1-2), 135-141.
105. Tanaka, H.; Kuriyama, M.; Ishida, Y.; Ito, S.-I.; Kubota, T.; Miyao, T.; Naito, S.; Tomishige, K.; Kunimori, K., Preferential Co Oxidation In Hydrogen-Rich Stream Over Pt Catalysts Modified With Alkali Metals - Part Ii. Catalyst Characterization And Role of Alkali Metals. *Applied Catalysis A-General* **2008,** *343* (1-2), 125-133.
106. Prinetto, F.; Manzoli, M.; Morandi, S.; Frola, F.; Ghiotti, G.; Castoldi, L.; Lietti, L.; Forzatti, P.,

Pt-K/Al2O3 Nsr Catalysts: Characterization of Morphological, Structural And Surface Properties. *Journal of Physical Chemistry C* **2010,** *114* (2), 1127-1138.

107. Pigos, J. M.; Brooks, C. J.; Jacobs, G.; Davis, B. H., Low Temperature Water-Gas Shift: Characterization of Pt-Based Zro2 Catalyst Promoted With Na Discovered By Combinatorial Methods. *Applied Catalysis A-General* **2007,** *319*, 47-57.
108. Pellegrini, R.; Leofanti, G.; Agostini, G.; Bertinetti, L.; Bertarione, S.; Groppo, E.; Zecchina, A.; Lamberti, C., Influence of K-Doping On A Pd/SiO2-Al2O3 Catalyst. *Journal of Catalysis* **2009,** *267* (1), 40-49.
109. Panagiotopoulou, P.; Kondarides, D. I., Effects of Alkali Additives On The Physicochemical Characteristics And Chemisorptive Properties of Pt/Tio(2) Catalysts. *Journal of Catalysis* **2008,** *260* (1), 141-149.
110. Evin, H. N.; Jacobs, G.; Ruiz-Martinez, J.; Graham, U. M.; Dozier, A.; Thomas, G.; Davis, B. H., Low Temperature Water-Gas Shift/Methanol Steam Reforming: Alkali Doping To Facilitate The Scission of Formate And Methoxy C-H Bonds Over Pt/Ceria Catalyst. *Catalysis Letters* **2008,** *122* (1-2), 9-19.
111. Rui, Z. B.; Wu, S. R.; Peng, C.; Ji, H. B., Comparison of TiO2 Degussa P25 With Anatase And Rutile Crystalline Phases For Methane Combustion. *Chem Eng J* **2014,** *243*, 254-264.
112. Sun, Y. N.; Qin, Z. H.; Lewandowski, M.; Carrasco, E.; Sterrer, M.; Shaikhutdinov, S.; Freund, H. J., Monolayer Iron Oxide Film On Platinum Promotes Low Temperature Co Oxidation. *J Catal* **2009,** *266* (2), 359-368.
113. Giordano, L.; Lewandowski, M.; Groot, I. M. N.; Sun, Y. N.; Goniakowski, J.; Noguera, C.; Shaikhutdinov, S.; Pacchioni, G.; Freund, H. J., Oxygen-Induced Transformations of An FeO(111) Film On Pt(111): A Combined Dft And Stm Study. *J Phys Chem C* **2010,** *114* (49), 21504-21509.
114. Lei, Y.; Lewandowski, M.; Sun, Y. N.; Fujimori, Y.; Martynova, Y.; Groot, I. M. N.; Meyer, R. J.; Giordano, L.; Pacchioni, G.; Goniakowski, J.; Noguera, C.; Shaikhutdinov, S.; Freund, H. J., CO Plus NO Versus CO+O-2 Reaction On Monolayer FeO(111) Films On Pt(111). *Chemcatchem* **2011,** *3* (4), 671-674.
115. Weng, X. F.; Zhang, K.; Pan, Q. S.; Martynova, Y.; Shaikhutdinov, S.; Freund, H. J., Support Effects On CO Oxidation On Metal-Supported Ultrathin FeO(111) Films. *Chemcatchem* **2017,** *9* (4), 705-712.
116. Kugai, J.; Fox, E. B.; Song, C., Role of CeO2 Support For Pd-Cu Bimetallic Catalysts For Oxygen-Enhanced Water Gas Shift. *Applied Catalysis A-General* **2013,** *456*, 204-214.
117. Qiao, B. T.; Liang, J. X.; Wang, A. Q.; Xu, C. Q.; Li, J.; Zhang, T.; Liu, J. Y., Ultrastable Single-Atom Gold Catalysts With Strong Covalent Metal-Support Interaction (CMSI). *Nano Research* **2015,** *8* (9), 2913-2924.
118. Qiao, B.; Wang, A.; Yang, X.; Allard, L. F.; Jiang, Z.; Cui, Y.; Liu, J.; Li, J.; Zhang, T., Single-Atom Catalysis of Co Oxidation Using Pt-1/FeOx. *Nature Chemistry* **2011,** *3* (8), 634-641.
119. Mei, D. H.; Glezakou, V. A.; Lebarbier, V.; Kovarik, L.; Wan, H. Y.; Albrecht, K. O.; Gerber, M.; Rousseau, R.; Dagle, R. A., Highly Active And Stable MgAl2O4-Supported Rh And Ir Catalysts For Methane Steam Reforming: A Combined Experimental And Theoretical Study. *Journal of Catalysis* **2014,** *316*, 11-23.
120. Ertl, G., *Reactions At Solid Surfaces*. New York: Wiley & Sons: **2009**.
121. Somorjai Ga, L. Y., *Introduction To Surface Chemistry And Catalysis*. New York: Wiley & Sons.: **2010**.
122. Goodman, D. W., Model Studies In Catalysis Using Surface Science Probes. *Chemical Reviews* **1995,** *95* (3), 523-536.
123. Tao, F.; Crozier, P. A., Atomic-Scale Observations of Catalyst Structures Under Reaction Conditions And During Catalysis. *Chemical Reviews* **2016,** *116* (6), 3487-3539.
124. Rossler, M.; Geng, P.; Wintterlin, J., A High-Pressure Scanning Tunneling Microscope For Studying

Heterogeneous Catalysis. *Rev Sci Instrum* **2005,** *76* (2).

125. Ertl, G., Reactions At Surfaces: From Atoms To Complexity (Nobel Lecture). *Angewandte Chemie-International Edition* **2008,** *47* (19), 3524-3535.
126. Goodman, D. W.; Peden, C. H. F., Co Oxidation Over Rh And Ru - A Comparative-Study. *J Phys Chem-Us* **1986,** *90* (20), 4839-4843.
127. Berlowitz, P. J.; Peden, C. H. F.; Goodman, D. W., Kinetics of Co Oxidation On Single-Crystal Pd, Pt, And Ir. *J Phys Chem-Us* **1988,** *92* (18), 5213-5221.
128. Vannice, M. A., Catalytic Synthesis of Hydrocarbons From Carbon-Monoxide And Hydrogen. *Catalysis Reviews-Science And Engineering* **1976,** *14* (2), 153-191.
129. Goodman, D. W., Correlations Between Surface Science Models And ''Real-World'' Catalysts. *J Phys Chem-Us* **1996,** *100* (31), 13090-13102.
130. Goodman, D. W., Chemical Modification of Chemisorptive And Catalytic Properties of Nickel. *Appl Surf Sci* **1984,** *19* (1-4), 1-13.
131. Chuang, S. S. C.; Pien, S. I., Infrared Study of The Co Insertion Reaction On Reduced, Oxidized, And Sulfided Rh/SiO2 Catalysts. *Journal of Catalysis* **1992,** *135* (2), 618-634.
132. Goodman, D. W., Ethane Hydrogenolysis Over Single-Crystals of Nickel - Direct Detection of Structure Sensitivity. *Surf Sci* **1982,** *123* (1), L679-L685.
133. Mccrea, K. R.; Somorjai, G. A., Sfg-Surface Vibrational Spectroscopy Studies of Structure Sensitivity And Insensitivity In Catalytic Reactions: Cyclohexene Dehydrogenation And Ethylene Hydrogenation On Pt(111) And Pt(100) Crystal Surfaces. *Journal of Molecular Catalysis A-Chemical* **2000,** *163* (1-2), 43-53.
134. Cremer, P. S.; Su, X. C.; Shen, Y. R.; Somorjai, G. A., Ethylene Hydrogenation On Pt(111) Monitored In Situ At High Pressures Using Sum Frequency Generation. *Journal of The American Chemical Society* **1996,** *118* (12), 2942-2949.
135. Fernandez-Garcia, M.; Martinez-Arias, A.; Hanson, J. C.; Rodriguez, J. A., Nanostructured Oxides In Chemistry: Characterization And Properties. *Chemical Reviews* **2004,** *104* (9), 4063-4104.
136. Nilius, N., Properties of Oxide Thin Films And Their Adsorption Behavior Studied By Scanning Tunneling Microscopy And Conductance Spectroscopy. *Surface Science Reports* **2009,** *64* (12), 595-659.
137. Rodriguez, J. A.; Grinter, D. C.; Liu, Z. Y.; Palomino, R. M.; Senanayake, S. D., Ceria-Based Model Catalysts: Fundamental Studies On The Importance of The Metal-Ceria Interface In CO Oxidation, The Water-Gas Shift, CO2 Hydrogenation, And Methane And Alcohol Reforming. *Chemical Society Reviews* **2017,** *46* (7), 1824-1841.
138. Calaza, F.; Stiehler, C.; Fujimori, Y.; Sterrer, M.; Beeg, S.; Ruiz-Oses, M.; Nilius, N.; Heyde, M.; Parviainen, T.; Honkala, K.; Hakkinen, H.; Freund, H. J., Carbon Dioxide Activation And Reaction Induced By Electron Transfer At An Oxide-Metal Interface. *Angewandte Chemie-International Edition* **2015,** *54* (42), 12484-12487.
139. Cui, Y.; Pan, Y.; Pascua, L.; Qiu, H. S.; Stiehler, C.; Kuhlenbeck, H.; Nilius, N.; Freund, H. J., Evolution of The Electronic Structure of CaO Thin Films Following Mo Interdiffusion At High Temperature. *Phys Rev B* **2015,** *91* (3).
140. Cui, Y.; Stiehler, C.; Nilius, N.; Freund, H. J., Probing The Electronic Properties And Charge State of Gold Nanoparticles On Ultrathin Mgo Versus Thick Doped Cao Films. *Phys Rev B* **2015,** *92* (7).
141. Solis, B. H.; Cui, Y.; Weng, X. F.; Seifert, J.; Schauermann, S.; Sauer, J.; Shaikhutdinov, S.; Freund, H. J.,

Initial Stages of CO2 Adsorption On CaO: A Combined Experimental And Computational Study. *Phys Chem Chem Phys* **2017,** *19* (6), 4231-4242.

142. Martynova, Y.; Shaikhutdinov, S.; Freund, H.-J., CO Oxidation On Metal-Supported Ultrathin Oxide Films: What Makes Them Active? *Chemcatchem* **2013,** *5* (8), 2162-2166.
143. Novotny, Z.; Mulakaluri, N.; Edes, Z.; Schmid, M.; Pentcheva, R.; Diebold, U.; Parkinson, G. S., Probing The Surface Phase Diagram of Fe_3O_4(001) Towards The Fe-Rich Limit: Evidence For Progressive Reduction of The Surface. *Phys Rev B* **2013,** *87* (19).
144. Xu, C.; Lai, X.; Zajac, G. W.; Goodman, D. W., Scanning Tunneling Microscopy Studies of The TiO2(110) Surface: Structure And The Nucleation Growth of Pd. *Phys Rev B* **1997,** *56* (20), 13464-13482.
145. Baumer, M.; Cappus, D.; Kuhlenbeck, H.; Freund, H. J.; Wilhelmi, G.; Brodde, A.; Neddermeyer, H., The Structure of Thin NiO(100) Films Grown On Ni(100) As Determined By Low-Energy-Electron Diffraction And Scanning Tunneling Microscopy. *Surf Sci* **1991,** *253* (1-3), 116-128.
146. Libuda, J.; Winkelmann, F.; Baumer, M.; Freund, H. J.; Bertrams, T.; Neddermeyer, H.; Muller, K., Structure And Defects of An Ordered Alumina Film On NiAl(110). *Surf Sci* **1994,** *318* (1-2), 61-73.
147. Schroeder, T.; Zegenhagen, J.; Magg, N.; Immaraporn, B.; Freund, H. J., Formation of A Faceted Moo2 Epilayer On Mo(112) Studied By Xps, Ups And Stm. *Surf Sci* **2004,** *552* (1-3), 85-97.
148. Blume, R.; Niehus, H.; Conrad, H.; Bottcher, A.; Aballe, L.; Gregoratti, L.; Barinov, A.; Kiskinova, M., Identification of Subsurface Oxygen Species Created During Oxidation of Ru(0001). *Journal of Physical Chemistry B* **2005,** *109* (29), 14052-14058.
149. Kim, Y. D.; Schwegmann, S.; Seitsonen, A. P.; Over, H., Epitaxial Growth of RuO2(100) On Ru(10(1)Over-Bar0): Surface Structure And Other Properties. *Journal of Physical Chemistry B* **2001,** *105* (11), 2205-2211.
150. Krasnikov, S. A.; Murphy, S.; Berdunov, N.; Mccoy, A. P.; Radican, K.; Shvets, I. V., Self-Limited Growth of Triangular PtO2 Nanoclusters On The Pt(111) Surface. *Nanotechnology* **2010,** *21* (33), 335301.
151. Rai, R.; Li, T.; Liang, Z.; Kim, M.; Asthagiri, A.; Weaver, J. F., Growth And Termination of A Rutile IrO2(100) Layer On Ir(111). *Surf Sci* **2016,** *652*, 213-221.
152. Gokhale, A. A.; Dumesic, J. A.; Mavrikakis, M., On The Mechanism of Low-Temperature Water Gas Shift Reaction On Copper. *Journal of The American Chemical Society* **2008,** *130* (4), 1402-1414.
153. Sun, Y. N.; Giordano, L.; Goniakowski, J.; Lewandowski, M.; Qin, Z. H.; Noguera, C.; Shaikhutdinov, S.; Pacchioni, G.; Freund, H. J., The Interplay Between Structure And CO Oxidation Catalysis On Metal-Supported Ultrathin Oxide Films. *Angewandte Chemie-International Edition* **2010,** *49* (26), 4418-4421.
154. Lewandowski, M.; Groot, I. M. N.; Shaikhutdinov, S.; Freund, H. J., Scanning Tunneling Microscopy Evidence For The Mars-Van Krevelen Type Mechanism of Low Temperature CO Oxidation On An FeO(1 1 1) Film On Pt(1 1 1). *Catal Today* **2012,** *181* (1), 52-55.
155. Udo Schwertmann, R. M. C., *The Iron Oxides: Structure, Properties, Reactions, Occurrences And Uses*. 2nd Ed.; Wiley-Vch: 2000.
156. Ning, Y. X.; Wei, M. M.; Yu, L.; Yang, F.; Chang, R.; Liu, Z.; Fu, Q.; Bao, X. H., Nature of Interface Confinement Effect In Oxide/Metal Catalysts. *Journal of Physical Chemistry C* **2015,** *119* (49), 27556-27561.
157. Khan, N. A.; Matranga, C., Nucleation And Growth of Fe And FeO Nanoparticles And Films On Au(111). *Surf Sci* **2008,** *602* (4), 932-942.
158. Ihle, D.; Lorenz, B., Small-Polaron Conduction And Short-Range Order In Fe_3O_4. *Journal of Physics*

C-Solid State Physics **1986,** *19* (26), 5239-5251.

159. Ritter, M.; Weiss, W., Fe_3O_4(111) Surface Structure Determined By Leed Crystallography. *Surf Sci* **1999,** *432* (1-2), 81-94.
160. Shaikhutdinov, S. K.; Ritter, M.; Wang, X. G.; Over, H.; Weiss, W., Defect Structures On Epitaxial Fe_3O_4(111) Films. *Phys Rev B* **1999,** *60* (15), 11062-11069.
161. Li, X. K.; Paier, J., Adsorption of Water On The Fe_3O_4(111) Surface: Structures, Stabilities, And Vibrational Properties Studied By Density Functional Theory. *Journal of Physical Chemistry C* **2016,** *120* (2), 1056-1065.
162. Santos-Carballal, D.; Roldan, A.; Grau-Crespo, R.; De Leeuw, N. H., A Dft Study of The Structures, Stabilities And Redox Behaviour of The Major Surfaces of Magnetite Fe_3O_4. *Phys Chem Chem Phys* **2014,** *16* (39), 21082-21097.
163. Xiaoke Li, J. P., Joachim Sauer, Francesca Mirabella, Eman Zaki, Francisco Ivars Barcelo, Shamil Shaikhutdinov, And Hans-Joachim Freund, Surface Termination of Fe_3O_4(111) Films Studied By Co Adsorption Revisited. *The Journal of Physical Chemistry B* **2017**.
164. Ceballos, S. F.; Mariotto, G.; Jordan, K.; Murphy, S.; Seoighe, C.; Shvets, I. V., An Atomic Scale Stm Study of The Fe_3O_4(001) Surface. *Surf Sci* **2004,** *548* (1-3), 106-116.
165. Stanka, B.; Hebenstreit, W.; Diebold, U.; Chambers, S. A., Surface Reconstruction of Fe_3O_4(001). *Surf Sci* **2000,** *448* (1), 49-63.
166. Tarrach, G.; Burgler, D.; Schaub, T.; Wiesendanger, R.; Guntherodt, H. J., Atomic Surface-Structure of Fe_3O_4(001) In Different Preparation Stages Studied By Scanning Tunneling Microscopy. *Surf Sci* **1993,** *285* (1-2), 1-14.
167. Chambers, S. A.; Thevuthasan, S.; Joyce, S. A., Surface Structure of Mbe-Grown Fe_3O_4(001) By X-Ray Photoelectron Diffraction And Scanning Tunneling Microscopy. *Surf Sci* **2000,** *450* (1-2), L273-L279.
168. Pentcheva, R.; Wendler, F.; Meyerheim, H. L.; Moritz, W.; Jedrecy, N.; Scheffler, M., Jahn-Teller Stabilization of A "Polar" Metal Oxide Surface: Fe_3O_4(001). *Phys Rev Lett* **2005,** *94* (12).
169. Pentcheva, R.; Moritz, W.; Rundgren, J.; Frank, S.; Schrupp, D.; Scheffler, M., A Combined Dft/Leed-Approach For Complex Oxide Surface Structure Determination: Fe_3O_4(001). *Surf Sci* **2008,** *602* (7), 1299-1305.
170. Bliem, R.; Mcdermott, E.; Ferstl, P.; Setvin, M.; Gamba, O.; Pavelec, J.; Schneider, M. A.; Schmid, M.; Diebold, U.; Blaha, P.; Hammer, L.; Parkinson, G. S., Subsurface Cation Vacancy Stabilization of The Magnetite (001) Surface. *Science* **2014,** *346* (6214), 1215-1218.
171. Novotny, Z.; Argentero, G.; Wang, Z.; Schmid, M.; Diebold, U.; Parkinson, G. S., Ordered Array of Single Adatoms With Remarkable Thermal Stability: Au/Fe_3O_4(001). *Phys Rev Lett* **2012,** *108* (21).
172. Rustad, J. R.; Wasserman, E.; Felmy, A. R., A Molecular Dynamics Investigation of Surface Reconstruction On Magnetite (001). *Surf Sci* **1999,** *432* (1-2), L583-L588.
173. Parkinson, G. S.; Novotny, Z.; Jacobson, P.; Schmid, M.; Diebold, U., A Metastable Fe(A) Termination At The Fe_3O_4(001) Surface. *Surf Sci* **2011,** *605* (15-16), L42-L45.
174. Spiridis, N.; Barbasz, J.; Lodziana, Z.; Korecki, J., Fe_3O_4(001) Films On Fe(001): Termination And Reconstruction of Iron-Rich Surfaces. *Phys Rev B* **2006,** *74* (15).
175. Fonin, M.; Pentcheva, R.; Dedkov, Y. S.; Sperlich, M.; Vyalikh, D. V.; Scheffler, M.; Rudiger, U.; Guntherodt, G., Surface Electronic Structure of The Fe_3O_4(100): Evidence of A Half-Metal To Metal Transition. *Phys Rev B* **2005,** *72* (10).
176. Spiridis, N.; Handke, B.; Slezak, T.; Barbasz, J.; Zajac, M.; Haber, J.; Korecki, J., Surface Structure of

Epitaxial Magnetite Fe_3O_4(001) Films: In Situ Stm And Cems Studies. *Journal of Physical Chemistry B* **2004,** *108* (38), 14356-14361.

177. Voogt, F. C.; Fujii, T.; Smulders, P. J. M.; Niesen, L.; James, M. A.; Hibma, T., No2-Assisted Molecular-Beam Epitaxy of Fe_3O_4, Fe3-Delta O4, And Gamma-Fe2o3 Thin Films On MgO(100). *Phys Rev B* **1999,** *60* (15), 11193-11206.
178. Mijiritskii, A. V.; Boerma, D. O., The (001) Surface And Morphology of Thin Fe_3O_4 Layers Grown By O-2-Assisted Molecular Beam Epitaxy. *Surf Sci* **2001,** *486* (1-2), 73-81.
179. Anderson, J. F.; Kuhn, M.; Diebold, U.; Shaw, K.; Stoyanov, P.; Lind, D., Surface Structure And Morphology of Mg-Segregated Epitaxial Fe_3O_4(001) Thin Films On MgO(001). *Phys Rev B* **1997,** *56* (15), 9902-9909.
180. Parkinson, G. S.; Manz, T. A.; Novotny, Z.; Sprunger, P. T.; Kurtz, R. L.; Schmid, M.; Sholl, D. S.; Diebold, U., Antiphase Domain Boundaries At The Fe_3O_4(001) Surface. *Phys Rev B* **2012,** *85* (19).
181. Binnig, G.; Rohrer, H.; Gerber, C.; Weibel, E., Tunneling Through A Controllable Vacuum Gap. *Appl Phys Lett* **1982,** *40* (2), 178-180.
182. Chen, C. J., *Introduction To Scanning Tunneling Microscopy*. Oxford University Press: **1993**.
183. Https://Www.Iap.Tuwien.Ac.At/Www/Surface/Stm_Gallery/Stm_Schematic.
184. Davisson, C.; Germer, L. H., Diffraction of Electrons By A Crystal of Nickel. *Phys Rev* **1927,** *30* (6), 705-740.
185. Clarke, L. J., *Surface Crystallography*. John Wiley & Sons Ltd: **1985**.
186. Http://Eng.Thesaurus.Rusnano.Com/Upload/Iblock/Cb5/Difrakcia-Medlen-Electr1.Jpg.
187. Duparc, O. H., Pierre Auger - Lise Meitner: Comparative Contributions To The Auger Effect. *Int J Mater Res* **2009,** *100* (9), 1162-1166.
188. Http://Hyperphysics.Phy-Astr.Gsu.Edu/Hbase/Atomic/Auger.Html.
189. Http://Www.Cif.Iastate.Edu/Sites/Default/Files/Uploads/Ms/Quadrupole%20pic.Jpg.
190. Redhead, P. A., Thermal Desorption of Gases. *Vacuum* **1962,** *12* (4).
191. Shaikhutdinov, S. K.; Meyer, R.; Naschitzki, M.; Baumer, M.; Freund, H. J., Size And Support Effects For Co Adsorption On Gold Model Catalysts. *Catalysis Letters* **2003,** *86* (4), 211-219.
192. Gatel, C.; Snoeck, E., Epitaxial Growth of Au And Pt On Fe_3O_4(111) Surface. *Surf Sci* **2007,** *601* (4), 1031-1039.
193. Meyer, R.; Shaikhutdinov, S. K.; Freund, H. J., CO Oxidation On A Pd/Fe_3O_4(111) Model Catalyst. *Zeitschrift Fur Physikalische Chemie-International Journal of Research In Physical Chemistry & Chemical Physics* **2004,** *218* (8), 905-914.
194. Gatel, C.; Snoeck, E., Comparative Study of Pt, Au And Ag Growth On Fe_3O_4(001) Surface. *Surf Sci* **2006,** *600* (13), 2650-2662.
195. Ma, T.; Fu, Q.; Su, H. Y.; Liu, H. Y.; Cui, Y.; Wang, Z.; Mu, R. T.; Li, W. X.; Bao, X. H., Reversible Structural Modulation of Fe-Pt Bimetallic Surfaces And Its Effect On Reactivity. *Chemphyschem* **2009,** *10* (7), 1013-1016.
196. Sakurai, M., Magnetic-Anisotropy of Epitaxial Fe/Pt(001) Multilayers. *Phys Rev B* **1994,** *50* (6), 3761-3766.
197. Hufnagel, T. C.; Kautzky, M. C.; Daniels, B. J.; Clemens, B. M., Structural Evolution During Deposition of Epitaxial Fe/Pt(001) Multilayers. *J Appl Phys* **1999,** *85* (5), 2609-2616.
198. Mulakaluri, N.; Pentcheva, R.; Scheffler, M., Coverage-Dependent Adsorption Mode of Water On Fe_3O_4(001): Insights From First Principles Calculations. *Journal of Physical Chemistry C* **2010,** *114* (25),

11148-11156.

199. Shvets, I. V.; Mariotto, G.; Jordan, K.; Berdunov, N.; Kantor, R.; Murphy, S., Long-Range Charge Order On The Fe_3O_4(001) Surface. *Phys Rev B* **2004,** *70* (15).
200. Shaikhutdinov, S.; Ritter, M.; Weiss, W., Hexagonal Heterolayers On A Square Lattice: A Combined Stm And Leed Study of FeO(111) On Pt(100). *Phys Rev B* **2000,** *62* (11), 7535-7541.
201. Parkinson, G. S.; Novotny, Z.; Argentero, G.; Schmid, M.; Pavelec, J.; Kosak, R.; Blaha, P.; Diebold, U., Carbon Monoxide-Induced Adatom Sintering In A Pd-Fe_3O_4 Model Catalyst. *Nature Materials* **2013,** *12* (8), 724-728.
202. Bliem, R.; Kosak, R.; Perneczky, L.; Novotny, Z.; Gamba, O.; Fobes, D.; Mao, Z.; Schmid, M.; Blaha, P.; Diebold, U.; Parkinson, G. S., Cluster Nucleation And Growth From A Highly Supersaturated Adatom Phase: Silver On Magnetite. *Acs Nano* **2014,** *8* (7), 7531-7537.
203. Hansen, K. H.; Worren, T.; Stempel, S.; Laegsgaard, E.; Baumer, M.; Freund, H. J.; Besenbacher, F.; Stensgaard, I., Palladium Nanocrystals On Al2O3: Structure And Adhesion Energy. *Phys Rev Lett* **1999,** *83* (20), 4120-4123.
204. Sun, Y. N.; Qin, Z. H.; Lewandowski, M.; Shaikhutdinov, S.; Freund, H. J., Co Adsorption And Dissociation On Iron Oxide Supported Pt Particles. *Surf Sci* **2009,** *603* (20), 3099-3103.
205. Mccabe, R. W.; Schmidt, L. D., Binding States of Co On Single-Crystal Planes of Pt. *Surf Sci* **1977,** *66* (1), 101-124.
206. Sala, A.; Marchetto, H.; Qin, Z. H.; Shaikhutdinov, S.; Schmidt, T.; Freund, H. J., Defects And Inhomogeneities In Fe_3O_4(111) Thin Film Growth On Pt(111). *Phys Rev B* **2012,** *86* (15).
207. Lemire, C.; Meyer, R.; Henrich, V. E.; Shaikhutdinov, S.; Freund, H. J., The Surface Structure of Fe_3O_4(111) Films As Studied By Co Adsorption. *Surf Sci* **2004,** *572* (1), 103-114.
208. Yu, X.; Tian, X.; Wang, S., Adsorption of Ni, Pd, Pt, Cu, Ag And Au On The Fe_3O_4(111) Surface. *Surf Sci* **2014,** *628*, 141-147.
209. Roland, B., Single Metal Adatoms At The Reconstructed Fe_3O_4 (001) Surface. *Phd Thesis*, *Tu Wien* **2016**.
210. Yu, X. H.; Tian, X. X.; Wang, S. G., Adsorption of Ni, Pd, Pt, Cu, Ag And Au On The Fe_3O_4(111) Surface. *Surf Sci* **2014,** *628*, 141-147.
211. Ringleb, F.; Fujimori, Y.; Wang, H. F.; Ariga, H.; Carrasco, E.; Sterrer, M.; Freund, H. J.; Giordano, L.; Pacchioni, G.; Goniakowski, J., Interaction of Water With FeO(111)/Pt(111): Environmental Effects And Influence of Oxygen. *Journal of Physical Chemistry C* **2011,** *115* (39), 19328-19335.
212. Fu, Q.; Li, W.-X.; Yao, Y.; Liu, H.; Su, H.-Y.; Ma, D.; Gu, X.-K.; Chen, L.; Wang, Z.; Zhang, H.; Wang, B.; Bao, X., Interface-Confined Ferrous Centers For Catalytic Oxidation. *Science* **2010,** *328* (5982), 1141-1144.
213. Fu, Q.; Yao, Y.; Guo, X.; Wei, M.; Ning, Y.; Liu, H.; Yang, F.; Liu, Z.; Bao, X., Reversible Structural Transformation of FeOx Nanostructures On Pt Under Cycling Redox Conditions And Its Effect On Oxidation Catalysis. *Phys Chem Chem Phys* **2013,** *15* (35), 14708-14714.
214. Sun, D.; Gu, X.-K.; Ouyang, R.; Su, H.-Y.; Fu, Q.; Bao, X.; Li, W.-X., Theoretical Study of The Role of A Metal-Cation Ensemble At The Oxide-Metal Boundary On CO Oxidation. *Journal of Physical Chemistry C* **2012,** *116* (13), 7491-7498.
215. Kudernatsch, W.; Peng, G. W.; Zeuthen, H.; Bei, Y. H.; Merte, L. R.; Lammich, L.; Besenbacher, F.; Mavrikakis, M.; Wendt, S., Direct Visualization of Catalytically Active Sites At The FeO-Pt(111) Interface. *Acs Nano* **2015,** *9* (8), 7804-7814.
216. Mu, R. T.; Fu, Q.; Guo, X. G.; Xu, X. J.; Tan, D. L.; Bao, X. H., A Comparative Study In Structure And

Reactivity of "FeOx-On-Pt" And "NiOx-On-Pt" Catalysts. *Sci China Chem* **2015,** *58* (1), 162-168.

217. Pan, Q.; Weng, X.; Chen, M.; Giordano, L.; Pacchioni, G.; Noguera, C.; Goniakowski, J.; Shaikhutdinov, S.; Freund, H.-J., Enhanced CO Oxidation On The Oxide/Metal Interface: From Ultra-High Vacuum To Near-Atmospheric Pressures. *Chemcatchem* **2015,** *7* (17), 2620-2627.
218. Martynova, Y.; Liu, B. H.; Mcbriarty, M. E.; Groot, I. M. N.; Bedzyk, M. J.; Shaikhutdinov, S.; Freund, H. J., CO Oxidation Over ZnO Films On Pt(111) At Near-Atmospheric Pressures. *Journal of Catalysis* **2013,** *301*, 227-232.
219. Pan, Q.; Liu, B. H.; Mcbriarty, M. E.; Martynova, Y.; Groot, I. M. N.; Wang, S.; Bedzyk, M. J.; Shaikhutdinov, S.; Freund, H. J., Reactivity of Ultra-Thin ZnO Films Supported By Ag(111) And Cu(111): A Comparison To ZnO/Pt(111). *Catalysis Letters* **2014,** *144* (4), 648-655.
220. Barth, J. V.; Brune, H.; Ertl, G.; Behm, R. J., Scanning Tunneling Microscopy Observations On The Reconstructed Au(111) Surface - Atomic-Structure, Long-Range Superstructure, Rotational Domains, And Surface-Defects. *Phys Rev B* **1990,** *42* (15), 9307-9318.
221. Voigtlander, B.; Meyer, G.; Amer, N. M., Epitaxial-Growth of Thin Magnetic Cobalt Films On Au(111) Studied By Scanning Tunneling Microscopy. *Phys Rev B* **1991,** *44* (18), 10354-10357.
222. Hallmark, V. M.; Chiang, S.; Rabolt, J. F.; Swalen, J. D.; Wilson, R. J., Observation of Atomic Corrugation On Au(111) By Scanning Tunneling Microscopy. *Phys Rev Lett* **1987,** *59* (25), 2879-2882.
223. Chambliss, D. D.; Wilson, R. J.; Chiang, S., Ordered Nucleation of Ni And Au Islands On Au(111) Studied By Scanning Tunneling Microscopy. *Journal of Vacuum Science & Technology B* **1991,** *9* (2), 933-937.
224. Maksymovych, P.; Sorescu, D. C.; Dougherty, D.; Yates, J. T., Surface Bonding And Dynamical Behavior of The Ch3sh Molecule On Au(111). *Journal of Physical Chemistry B* **2005,** *109* (47), 22463-22468.
225. Piccolo, L.; Loffreda, D.; Aires, F.; Deranlot, C.; Jugnet, Y.; Sautet, P.; Bertolini, J. C., The Adsorption of Co On Au(111) At Elevated Pressures Studied By Stm, Rairs And Dft Calculations. *Surf Sci* **2004,** *566*, 995-1000.
226. Min, B. K.; Alemozafar, A. R.; Biener, M. M.; Biener, J.; Friend, C. M., Reaction of Au(111) With Sulfur And Oxygen: Scanning Tunneling Microscopic Study. *Top Catal* **2005,** *36* (1-4), 77-90.
227. Woll, C.; Chiang, S.; Wilson, R. J.; Lippel, P. H., Determination of Atom Positions At Stacking-Fault Dislocations On Au(111) By Scanning Tunneling Microscopy. *Phys Rev B* **1989,** *39* (11), 7988-7991.
228. Bligaard, T.; Norskov, J. K.; Dahl, S.; Matthiesen, J.; Christensen, C. H.; Sehested, J., The Bronsted-Evans-Polanyi Relation And The Volcano Curve In Heterogeneous Catalysis. *Journal of Catalysis* **2004,** *224* (1), 206-217.
229. Goniakowski, J.; Noguera, C., Polarization And Rumpling In Oxide Monolayers Deposited On Metallic Substrates. *Phys Rev B* **2009,** *79* (15).
230. Davis, L. E., Macdonald, N. C., Palmberg, P. W., G. E. Riach, Weber ,R. E. , *Handbook of Auger Electron Spectroscopy,*. Perkin Elmer Corp.,Eden Prairie: Minnesota, , 1977.
231. Weiss, W.; Somorjai, G. A., Preparation And Structure of 1-8 Monolayer Thick Epitaxial Iron-Oxide Films Grown On Pt(111). *J Vac Sci Technol A* **1993,** *11* (4), 2138-2144.
232. Galloway, H. C.; Benitez, J. J.; Salmeron, M., Growth of FeOx On Pt(111) Studied By Scanning-Tunneling-Microscopy. *J Vac Sci Technol A* **1994,** *12* (4), 2302-2307.
233. Weiss, W.; Ritter, M., Metal Oxide Heteroepitaxy: Stranski-Krastanov Growth For Iron Oxides On Pt(111). *Phys Rev B* **1999,** *59* (7), 5201-5213.
234. Yao, Y. X.; Fu, Q. A.; Wang, Z.; Tan, D. L.; Bao, X. H., Growth And Characterization of Two-Dimensional

FeO Nanoislands Supported On Pt(111). *Journal of Physical Chemistry C* **2010,** *114* (40), 17069-17079.

235. Vurens, G. H.; Maurice, V.; Salmeron, M.; Somorjai, G. A., Growth, Structure And Chemical-Properties of FeO Overlayers On Pt(100) And Pt(111). *Surf Sci* **1992,** *268* (1-3), 170-178.
236. Wei, M. M.; Fu, Q.; Dong, A. Y.; Wang, Z. J.; Bao, X. H., Coverage And Substrate Effects On The Structural Change of FeOx Nanostructures Supported On Pt. *Top Catal* **2014,** *57* (10-13), 890-898.
237. Liu, Y.; Yang, F.; Zhang, Y.; Xiao, J. P.; Yu, L.; Liu, Q. F.; Ning, Y. X.; Zhou, Z. W.; Chen, H.; Huang, W. G.; Liu, P.; Bao, X. H., Enhanced Oxidation Resistance of Active Nanostructures Via Dynamic Size Effect. *Nature Communications* **2017,** *8*.
238. Giordano, L.; Pacchioni, G.; Noguera, C.; Goniakowski, J., Identification of Active Sites In A Realistic Model of Strong Metal-Support Interaction Catalysts: The Case of Platinum (111)-Supported Iron Oxide Film. *Chemcatchem* **2014,** *6* (1), 185-190.
239. Mclean, J. G.; Krishnamachari, B.; Peale, D. R.; Chason, E.; Sethna, J. P.; Cooper, B. H., Decay of Isolated Surface Features Driven By The Gibbs-Thomson Effect In An Analytic Model And A Simulation. *Phys Rev B* **1997,** *55* (3), 1811-1823.
240. Wang, Z. J.; Dong, J. C.; Cui, Y.; Eres, G.; Timpe, O.; Fu, Q.; Ding, F.; Schloegl, R.; Willinger, M. G., Stacking Sequence And Interlayer Coupling In Few-Layer Graphene Revealed By In Situ Imaging. *Nature Communications* **2016,** *7*.

Publications and conference appearances

Publications

1. ***Ke Zhang***, Shamil Shaikhutdinov, Hans-Joachim Freund, Does the Surface Structure of Oxide Affect Strong Metal-Support Interaction with Pt? Pt on Fe_3O_4(001) vs Fe_3O_4(111), ChemCatChem, 2015, 7, 3725-3730
2. ***Ke Zhang***, Linfei Li, Shamil Shaikhutdinov, Hans-Joachim Freund, CO oxidation on metal-supported monolayer oxide films: What phase (interface) is active?, Angewandte Chemie International Edition, accepted
3. Xuefei Weng, ***Ke Zhang***, Qiushi Pan, Yulia Martynova, Shamil Shaikhutdinov, Hans-Joachim Freund, Support effects on CO oxidation on metal-supported ultrathin FeO(111) films, ChemCatChem, 2017, 9, 705-712
4. Earl M. Davis, ***Ke Zhang***, Yi Cui, Helmut Kuhlenbeck, Shamil Shaikhutdinov, Hans-Joachim Freund, Growth of Fe_3O_4 (001) thin films on Pt(100): Tuning surface termination with an Fe buffer layer, Surface Science, 2015, 636, 42–46
5. ***Ke Zhang***, Shamil Shaikhutdinov, Hans-Joachim Freund, Size-dependent O desorption on FeO_2/Pt(111) island, in preparation

Conference appearances

1. ***Ke Zhang***, Shamil Shaikhutdinov, Hans-Joachim Freund, strong metal support interaction of noble metal supported on Fe_3O_4(001) surface, Talk, European Conference on Surface Science(ECOSS) 31, Barcelona

Acknowledgement

Standing at the point to be finishing my PhD study, I gratefully acknowledge my supervisor, Prof. Dr. Hans-Joachim Freund, for giving me the opportunity to study and work with best of the best scientists and on state-of-the-art equipment. I greatly appreciate his supervision and trust.

I would like to thank Prof. Dr. Mario Dähne for kindly being the cosupervisor and reviewing my thesis.

I would like to thank Prof. Dr. Reinhard Schomäcker for kindly agreeing to be the chairman of the defense examination committee.

I am particularly grateful to Dr. Shamil Shaikhutdinov, who is my daily scientific advisor. I appreciate his patience and trust he showed throughout my PhD study. I am also very grateful for his valuable comments on my PhD thesis.

I also owe my sincere gratitude to my colleagues, Dr. Linfei Li, for cooperation on FeO/Pt system; Earl Davis, on Fe_3O_4(001) thin film preparation and STM; Dr. Zhujun Wang, Dr. Petr Dementyev, Dr. Qiushi Pan, Dr. Francisco Ivars-Barcelo, Prof. Yi Cui, Dr. Mikołaj Lewandowski, Dr. Florencia Calaza, Dr. Zongfang Wu, Paulina Adrianna Dębek, Sylwia Jarmolińska for helpful discussions.

I am thankful to Dr. Georg Simon and Kristin Werner for help in abstract translation from English to German.

My thanks would also go to Daniel Jüterbock, Matthias Naschitzki, Walter Wachsmann and specially, Klaus-Peter Vogelgesang, for their technical assistance, and to Manuela Misch and Daniela Nikolaus for their patient help in administrative works.

Finally, my deepest gratitude goes to my beloved parents and wife Yisha for their endless love, persistent encouragement and great confidence in me. They have been a constant source of courage and inspiration in my life.

Curriculum Vitae

The curriculum vitae is not included in the online version

List of abbreviations

AC-HRTEM Aberration-corrected High-resolution Transmission Electron Microscopy
AES Auger Electron Spectroscopy
AFM Atomic Force Microscopy
DFT Density Function Theory
DOS Density of States
DRIFT Diffuse reflectance infrared Fourier transform
EELS Electron energy loss spectroscopy
FFT Fast Fourier Transform
HRTEM High-resolution Transmission Electron Microscopy
LDOS Local Density of States
LEED Low Energy Electron Diffraction
LT Low temperature
ML Monolayer
MS Mass Spectrometry / Mass Spectrometer
PVD Physical Vapor Deposition
QMS Quadrupole Mass Spectrometer
RGA Residual Gas Analysis
RT Room Temperature
SEM Scanning Electron Microscopy
SMSI Strong Metal-Support Interaction
SPM Scanning Probe Microscopy
STM Scanning Tunneling Microscopy
STS Scanning Tunneling Spectroscopy
TDS Thermal Desorption Spectroscopy
TEM Transmission Electron Microscopy
TPD Temperature Programmed Desorption
UHV Ultra-High Vacuum
XPS X-ray Photoelectron Spectroscopy